Transitions and helicity in two-dimensional three-component turbulence

N'Nankou Agoua

N° d'ordre NNT: 2023ECDL0055

THESE DE DOCTORAT DE
L'ECOLE CENTRALE DE LYON

MEMBRE DE L'UNIVERSITÉ DE LYON

ÉCOLE DOCTORALE No.162 MEGA
Mécanique, Énergétique, Génie civil, Acoustique

Spécialité: Mécanique des Fluides

Soutenue publiquement le 18/12/2023 par :

Wesley Agoua

Transitions and Helicity in two-dimensional three-component turbulence

Devant le jury composé de:

BOS Wouter	Directeur de Recherche CNRS	Directeur de Thèse
DORMY Emmanuel	Directeur de Recherche CNRS	Rapporteur
FAVIER Benjamin	Chargé de Recherche CNRS	Examinateur
GREA Benoît-Joseph	Directeur de Recherche CEA	Examinateur
LESUR Maxime	Maître de Conférences - Université de Lorraine	Rapporteur
MURAGLIA Magali	Maître de Conférences - Université Aix-Marseille	Examinatrice
THALABARD Simon	Maître de Conférences - Université Côte d'Azur	Examinateur

Contents

List of Figures

Remerciements

Je tiens à remercier en premier lieu les membres du jury pour avoir pris le temps d'évaluer mon travail de thèse, le président du jury Benoit-Joseph Gréa, les examinateurs Magali Muraglia, Benjamin Favier et notre invité Simon Thalabard, et plus particulièrement les rapporteurs Maxime Dormy et Maxime Lesur pour avoir évaluer le manuscrit de thèse et avoir relevé les bons passages tout comme les points pouvant être améliorés. Je remercie tous les membres du jury pour leur intérêt pour mon travail et les discussions que nous avons pu avoir lors de la soutenance.

En premier lieu je remercie évidemment mon boss Wouter, qui m'a proposé ce sujet de thèse après mon stage. Merci infiniment pour ton soutien durant toutes ces années, notamment pendant ces moments quand tu as plus cru au projet que moi même. Ce fut un véritable plaisir de travailler avec toi et d'apprendre beaucoup sur la turbulence et la simulation numérique. Tu m'as aidé à progresser en matière de méthode de recherche et je te remercie pour ta confiance qui m'a permis de travailler avec une bonne autonomie et qui nous a menés sur des champs de recherche imprévus mais passionnants. Une petite équipe s'est constitué avec Tong, Ryo, puis Bruce et Smiron. Cela a permis une belle collaboration entre turbulence et mécanique statistique présente dans cette thèse. Quant à toi Smiron bon courage pour ta fin de thèse, j'attend une soutenance en français évidemment!

Je tiens à remercier Phlippe Blanc-Benon et Christophe Bailly, les directeur successifs du laboratoire qui m'ont accueilli et permis de mener ma thèse à terme au LMFA. Je remercie plus particulièrement Christophe qui a été le premier durant son cours à me présenter ce concept étrange d turbulence qui allait occuper mes quatre dernières années.

Je souhaite remercier Stéphane Aubert, Pierre Duquesne et Christophe Corre pour m'avoir accueilli au sein du département MFAE et particulièrement dans la joyeuse équipe d'UE FLE, dans laquelle j'ai pu découvrir le merveilleux métier d'enseignant en tant que moniteur puis ATER (merci Pierre!). Ce fut une expérience très enrichissante, notamment sur le plan pédagogique, et je remercie chaleureusement tous mes collègues pour leurs nombreux conseils prodigués. Je remercie notamment Richard pour sa passion pour les canaux, Vincent et Alexis pour la formation sur les différents TPs, Marc et Didier pour les précieux conseils pour les corrections et leurs belles anecdotes, Gilles pour son partage d'expérience et m'avoir encouragé dans ma carrière de chanteur, Michel pour sa bonne humeur à toutes épreuves et ses nombreux remplacements, Ariane pour son optimisme et ses encouragements pour ma thèse. Je tire aussi mon chapeau à Horacio, Michel et Seb qui bichonnent avec amour les bancs expérimentaux.

Un salut tout particulier au plus Anglais des Italiens Andrea, qui avec confiance (ou naïveté je ne sais pas trop) m'a confié la tâche d'encadrer les TD du cours de transfert thermique, rôle que j'ai le grand plaisir de transmettre à Mathieu cette année (pour son plus grand plaisir à lui aussi je présume) . Merci à toi cher Aveyronnais pour m'avoir aidé

à gardé le moral en fin de thèse, et m'avoir donné envie de passer le reste de ma vie dans le Rouergue!

Durant ma thèse je fus accueilli dans l'équipe Turbulence et Instabilités, dirigée d'une main de maître par Florence Raynal. J'ai pu y bénéficier des précieux conseils et anecdotes de mes aînés et voisins de couloir Benoit et Fabien qui m'ont beaucoup appris sur le fonctionnement de la recherche scientifique. Bon courage à toi Benoit pour ta croisade pour le libre accès à la science ! Je salue aussi les autres camarades du couloir I11 Ouest Xavier et Marc qui entretiennent l'atmosphère de travail sympathique du meilleur couloir du labo ! Un coucou aussi aux locataire du RDC, Benjamin, Aurore et Juan que j'aurai le plaisir de retrouver au pied des Alpes . Merci beaucoup pour ton café camarade !

Je remercie très chaleureusement la fine équipe SAF, Marie-Noëlle, Marie-Gabrielle , Sylviane, Fatima, Camille, et plus particulièrement celles qui ont dû le plus se coltiner ma phobie administrative Noura et Emelyne. Merci à vous toutes pour votre patience à l'égard de mon inaptitude à remplir correctement un ordre de mission ! Sans vous le labo ne tiendrait vraiment pas longtemps!

Autres piliers du labo les membres du pôle calcul, chargés entre autre de gérer notre bon vieux Newton. Je remercie tout particulièrement Laurent, qui m'a sorti de beaucoup de pétrins durant mon séjour et qui fut toujours encourageant et positif. Bonne continuation à toi à l'INRIA! Merci beaucoup à Anne, qui s'est montrée disponible et très, TRES patiente pour m'aider à utiliser les codes numériques sur le calculateur. Le padawan Mattéo, très efficace et toujours disponible en cas de pépin, et bien sûr Lulu revenu de son exil toulousain pour prêter main-forte à la fine équipe.

Durant cette thèse j'ai pu côtoyer d'autres jeunes camarades dans un bureau où étaient déjà passées nombre de légendes de la turbulence. J'ai été chaleureusement accueilli par Cenk qui m'a initié au code DNS maison, et par Alexandr qui m'a montré bien en avance les difficultés de la fin de thèse. Et bien sûr ce cher Henri qui fut mon compagnon de travail pendant plus de deux ans. Nous avons été rejoints rapidement par Ahmed afin de former un chouette trio. Les gars se fut un plaisir de bosser avec vous, malgré vos quelques mois d'infidélités! Nous avons supporté ensemble le trafic sur Newton, l'absence de fenêtre, la chaleur tropicale estivale dans la bonne humeur.

Je remercie évidemment ma famille pour leur soutien pendant toutes ces années. Je ne suis pas sûr que vous ayez compris . L'un de mes objectifs était d'être docteur avant mon petit frère, objectif atteint et bon courage à toi frangin ! Je pense aussi aux amis qui m'ont encouragé tout le long du chemin. Ceux de Paris, comme JB et Barthélémy qui ont carrément pris une journée pour venir voir ma soutenance, Floflo Marco, PC, Robin, Nikita et tous les autres. Mais aussi les Lyonnais que j'ai rencontré pendant cette thèse comme Aurélie et Rexhina.

Et enfin je tiens à remercier les vendeurs de donuts, notamment un petit commerçant athénien qui m'a permis de faire le spectacle à l'EFMC, ainsi que les magasins lyonnais Donuts Land et Dream Donuts qui n'ont pas dû comprendre le lien entre leurs donuts et un réacteur nucléaire.

Résumé

Cette thèse étudie la turbulence incompressible bidimensionnelle (2D) avec trois composantes de vitesse. De tels systèmes seront appelés écoulements 2D3C. Deux classes principales sont considérées, les écoulements 2D3C cartésiens et les écoulements 2D3C axisymétriques.

Pour la première classe d'écoulements, nous montrons que l'hélicité est associée à une corrélation entre la vorticité verticale et un champ scalaire, représentant ici la vitesse verticale. La mécanique statistique permet de prédire la persistance possible de structures hélicoïdales à grande échelle. Cette prédiction est vérifiée par des simulations numériques et son implication dans les applications de mélange est discutée. En effet, la corrélation vorticité-scalaire déterminera l'efficacité du mélange dans les écoulements 2D.

Nous étudions ensuite, dans la turbulence axisymétrique, une transition critique entre un écoulement purement poloïdal, un écoulement 2D et un écoulement 2D3C. Nous transposons les idées à une géométrie toroïdale et soutenons que cette transition peut jouer un rôle majeur dans les tokamaks, où une transition critique conduit à un meilleur confinement du plasma.

Dans la dernière partie, nous illustrons comment l'hélicité peut être générée spontanément. Nous effectuons des simulations de turbulence stratifiée instable en présence d'un champ magnétique intense. Nous soutenons que le mécanisme de génération d'hélicité observé pourrait être également observé dans des applications géophysiques si une forte anisotropie est combinée avec des mécanismes linéaires d'injection d'énergie.

Abstract

This thesis investigates two-dimensional (2D) incompressible turbulence with three velocity components. Such systems will be called 2D3C flows. Two main classes are considered, Cartesian 2D3C flows and axisymmetric 2D3C flows.

For the first class of flows we show that helicity is associated with a correlation between the vertical vorticity and a scalar field, here representing the vertical velocity. Statistical mechanics allows to predict the possible persistence of large-scale helical structures. This prediction is verified in numerical simulations and its implication for mixing applications is discussed. Indeed, the vorticity-scalar correlation will importantly affect the mixing-efficiency in 2D flows.

We then investigate, in axisymmetric turbulence, a critical transition between a purely poloidal 2D flow and a 2D3C flow. We transpose the ideas to a toroidal geometry and argue that this transition can play a major role in tokamaks, where a critical transition leads to enhanced plasma confinement.

In the final part, we illustrate how helicity can be generated, spontaneously. We carry out simulations of unstably stratified turbulence in the presence of a strong magnetic field. We argue that the observed helicity generating mechanism might be observed in geophysical applications if strong anisotropy is combined with linear energy injection mechanisms.

1 Motivations and objectives

The beginning of the study of turbulence is often attributed to Leonardo da Vinci who drew sketches of turbulent flows five centuries ago[1]. The modern study of turbulence is obviously younger and starts, somewhat subjectively, with the work of Reynolds [2], Richardson [3] and Taylor [4]. In particular Taylor introduced the concept of homogeneous and isotropic turbulence, a kind of turbulence which, statistically, is invariant with respect to rotations and translations. Three-dimensional homogeneous turbulence has received since then received an enormous amount of attention, and entire textbooks have been written on the subject (e.g. [1, 5, 6]).

Another field of research, greatly inspired by geophysical flows, is the study of two-dimensional turbulence. Such flow, described by the movement of fluid motion in a plane, can also be simplified, statistically, to yield two-dimensional homogeneous and isotropic turbulence, where the same symmetries are satisfied as in the three dimensional case, but now only with respect to translations and rotations in the considered plane. In particular since the work of Kraichnan [7], and the discovery and statistical characterization of the inverse cascade, two-dimensional turbulence has received an enormous attention[2].

Flows in nature are however never purely two-dimensional nor isotropic. A whole class of flows described approximately by two-dimensional theory does contain a third velocity component. In the present manuscript we investigate such a subclass, which is conceptually situated in between two-dimensional and three-dimensional turbulent flows. Specifically, we investigate two-dimensional three-component (2D3C) flows. These flows are characterized by the fact that they can be described by three velocity components, which vary only in two space dimensions.

A major difference characterizing these flows, compared to either 2D or 3D flows is the invariants. Whereas energy-conservation is a (almost) universal property of turbulent flows in the absence of dissipation, 2D turbulence conserves also enstrophy and 3D turbulence conserves helicity. The conservation of these quantities, which will be introduced in the following chapter, will change the dynamics of the 2D3C flows considered in the present work. Furthermore, we will be interested to see how the dynamics of a flow change when we are close to the transition between 2D or 3D flows and the here considered 2D3C flows.

Even though our approach is fairly theoretical, we do have two specific applications in mind and these applications are on the one hand the transition towards enhanced confinement observed in tokamak fusion plasmas and the generation of helicity in geophysical and astrophysical flows on the other. At first sight these two phenomena have nothing in common. However, once we explore the dynamics of 2D3C turbulence,

[1] See for instance the cover-illustration of the textbook by Uriel Frisch [1].

[2] Kraichnan's publication has been cited about 4000 times at the moment of this writing (source: Google Scholar 9/10/2023).

we can understand both effects as transitions towards 2D3C turbulence. For the first application, tokamaks, the transition is between 2D2C flows and 2D3C flows, whereas the generation of helicity is associated with a transition from 3D3C to 2D3C flow.

As a third application of the theoretical results in this thesis, we anticipate that helicity in 2D3C flows is a quantity which is intimately related with the advection of a passive scalar in two-dimensional flow. As such, we will show that we can understand why mixing is very sensitive to initial conditions.

The present manuscript is then constructed as follows. In the next chapter, Chap. 2, we introduce the necessary concepts. Chap. 3 discusses the numerical tools used to investigate the different flows. Chap. 4 addresses the dynamics of Cartesian 2D3C flows, with an application to mixing. Axisymmetric turbulence in unbounded geometry is investigate in Chap. 5. The findings of this chapter are then transposed to more complex, wall bounded geometry geometry, in Chap. 6, where it is argued that the transition between 2D2C flows and 2D3C flows can be relevant to fusion research. The final chapter before the conclusions, Chap. 7 illustrates how unstable stratification, combined with a strong magnetic field allows to attain a 2D3C limit, where helicity can be generated spontaneously.

2 Introduction: some generalities about turbulence

In this chapter we introduce some necessary concepts for the remainder of this thesis. In particular we discuss the governing equations, the concept of inviscid invariants, the description of turbulence in Fourier space, cascades of energy in 2D and 3D turbulence and transitions between turbulent flows with different dimensionalities.

2.1 What is turbulence?

"Turbulence is everywhere" is a common sentence often heard during lectures of fluid mechanics. Indeed turbulent flows can be encountered both in nature and engineering applications, from quantum scales to interplanetary distances. Often turbulence is a harmful property of the flow, for instance when the goal is to efficiently transport fluid through pipes, where from an energetic viewpoint turbulence is undesirable, or during airplane flights where planes and their passengers get shaken by turbulent bursts. However there are cases where turbulence is beneficial. For instance mixing is more efficient when a flow is turbulent. Even though turbulence is an ubiquitous phenomenon, it takes such different forms in different physical systems that its precise definition is not straightforward. Turbulence is therefore mostly defined by its characteristic properties and we will refrain from an attempt to give a precise definition.

Turbulent flows of liquid, gas and plasma are characterized by a chaotic disorder. Reynolds called turbulent flows "sinuous" [2], since in contrast to "direct" laminar flows, turbulent trajectories seem less predictable and not "direct" but "sinuous" between two points of the flow. These non-straight trajectories are caused by fluctuations, the size of which can rarely be neglected in a turbulent flow. The fluctuations are often associated with chaotic vortical motion and the associated vortices in a turbulent flow are rarely stable for a long time. The fragmentation of vortices and other types of structures in a flow leads to the coexistence of a wide range of length scales, and the inherent difficulties to study multi-scale systems. Because of these particularities, it is, in general, not convenient to use a deterministic approach to study turbulence. We will discuss later in this chapter the appropriate statistical tools to study turbulent flows.

It was early noticed [2] that turbulence could be triggered, in pipes, by high velocities, or kinetic energy. Another parameter is the viscosity of the flow, since flows with a small viscosity, like most gases, become more easily turbulent than honey, in which kinetic energy is rapidly dissipated by the viscous friction. In some sense turbulence seems the manifestation of the difficulty of the flow to deal with its kinetic energy.

Regimes in mechanics are usually defined using non-dimensional control parameters.

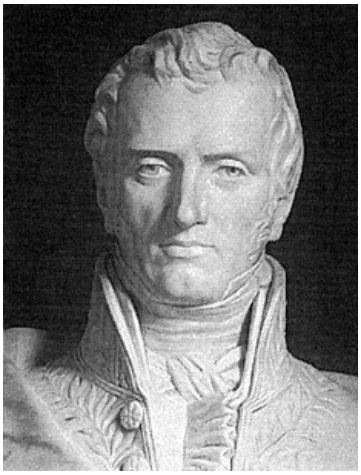

Figure 2.1: Entente Cordiale in fluid mechanics: Claude-Louis Navier and George Gabriel Stokes.

In the experiment by Osborne Reynolds, it was observed that the transition from laminar to turbulent flow was determined by the Reynolds number Re [2], defined as:

$$Re = \frac{uL}{\nu} \tag{2.1}$$

with L a characteristic length of the flow (the pipe diameter for Reynolds), u a characteristic velocity amplitude, and ν the kinematic viscosity. A more insightful definition of the Reynolds number is that it measures the relative influence of advection to viscous stresses on a fluid particle,

$$Re = \frac{\text{advection}}{\text{viscous stress}}, \tag{2.2}$$

but to better interpret this interpretation we need to write the evolution-equation of a fluid parcel, governed by the Navier-Stokes equations. That will be done now.

2.2 Governing equations

In this section we will focus, respectively, on the evolution equations of mass, momentum, vorticity and advected scalar quantities.

2.2.1 The Navier-Stokes equations

The Navier-Stokes (NS) equations govern the dynamics of fluids. They are derived from usual continuity equations, concerning density (i.e. mass) and momentum conservation.

We first consider the mass continuity equation,

$$\frac{\partial \rho}{\partial t} + \nabla \cdot (\rho \boldsymbol{u}) = 0, \tag{2.3}$$

with $\rho(x, y, z, t)$ the density and $\boldsymbol{u}(x, y, z, t)$ the velocity field. For this study we consider an incompressible flow. This means that the density of a fluid parcel remains constant so

that the material derivative of the density is zero,

$$\frac{\mathrm{D}\rho}{\mathrm{D}t} = \frac{\partial \rho}{\partial t} + \boldsymbol{u} \cdot \nabla \rho = 0. \tag{2.4}$$

This relation can be interpreted as a volume continuity equation: the volume of a fluid parcel remains constant along a streamline. Combining these expressions, we obtain the so-called divergence-free condition for incompressible flow,

$$\nabla \cdot \boldsymbol{u} = 0. \tag{2.5}$$

The Navier-Stokes equations are obtained by applying Newton's second law to the same kind of fluid parcel. It illustrates the conservation of the momentum $\rho \boldsymbol{u}$,

$$\frac{\mathrm{D}\rho \boldsymbol{u}}{\mathrm{D}t} = \frac{\partial \rho \boldsymbol{u}}{\partial t} + \boldsymbol{u} \cdot \nabla \rho \boldsymbol{u} = \boldsymbol{F}_{int} + \boldsymbol{F}_{ext} \tag{2.6}$$

with $\boldsymbol{F}_{ext}$ externally imposed forces and $\boldsymbol{F}_{int}$ represents the internal forces, respectively, associated with stresses on the fluid particle. The stress tensor $\boldsymbol{\sigma}$ can be used to model the internal forces with $\boldsymbol{F}_{int} = \nabla \cdot \boldsymbol{\sigma}$. In fluid mechanics the stress tensor is split into a pressure part $P\boldsymbol{I}$ and a deviatoric viscous part $\boldsymbol{\tau}$. P is called pressure. For an isotropic flow $P = \sigma_{ii}$.

We consider a Newtonian fluid, which means there is a linear relation between $\boldsymbol{\tau}$ and the the strain rate tensor $\boldsymbol{S} = \nabla \boldsymbol{u}$ so that

$$\boldsymbol{\sigma} = -P\boldsymbol{I} + \boldsymbol{\tau} \qquad \text{with} \quad \boldsymbol{\tau} = \mu \left(\nabla \boldsymbol{u} + \nabla \boldsymbol{u}^T \right) + \lambda (\nabla \cdot \boldsymbol{u}) \boldsymbol{I}. \tag{2.7}$$

With the incompressibility condition (2.5) the second term is null. The dynamic viscosity μ will be considered constant in this study, leading to

$$\frac{\partial \rho \boldsymbol{u}}{\partial t} + \boldsymbol{u} \cdot \nabla \rho \boldsymbol{u} = \rho \left[\frac{\partial \boldsymbol{u}}{\partial t} + \boldsymbol{u} \cdot \nabla \boldsymbol{u} \right] \qquad \text{and} \qquad \nabla \cdot \boldsymbol{\tau} = \mu \Delta \boldsymbol{u}. \tag{2.8}$$

This yields the Navier-Stokes equation for a homogeneous, isotropic, Newtonian and incompressible flow with constant viscosity,

$$\frac{\partial \boldsymbol{u}}{\partial t} + \boldsymbol{u} \cdot \nabla \boldsymbol{u} = -\frac{1}{\rho} \nabla P + \nu \Delta \boldsymbol{u} + \boldsymbol{F}, \tag{2.9}$$

with $\nu = \mu / \rho$ the kinematic viscosity and $\boldsymbol{F} = \boldsymbol{F}_{ext}$ the external body-forces. These forces can result for example from buoyancy, magnetic fields etc. The resulting equation is nonlinear. The non-linear term $\boldsymbol{u} \cdot \nabla \boldsymbol{u}$ (also called advection term) is the key of the comprehension of chaos and turbulence (and it can be argued that it is this nonlinearity which makes fluid mechanics really interesting...).

Since in most of the following we will focus on constant density flows, we will, unless otherwise stated, absorb the density into the pressure,

$$P/\rho \to P. \tag{2.10}$$

Only in the last chapter of this thesis, Chap. 7, we will consider a case where fluctuations of the density play a role. By taking the divergence of (2.9) and taking into account the divergence-free condition, a Poisson equation can be obtained for the pressure,

$$\Delta P = \nabla \cdot (\boldsymbol{F} - \boldsymbol{u} \cdot \nabla \boldsymbol{u}). \tag{2.11}$$

If this expression is solved, the pressure can be eliminated from the system, so that, for given external forces, the three equations for the components of $\boldsymbol{u}$ are determined by three partial differential equations. This is not always analytically possible and in many systems treating the pressure term is challenging. In particular this relation shows how body forces and pressure are entangled in the dynamics of the Navier-Stokes equations and their disentanglement in complex flows is a subject of recent research [8].

Equations (2.9) can be formulated in different coordinate systems. The Cartesian formulation is the most generally used and we have there $\boldsymbol{u} = (u, v, w)$, $\nabla = (\partial_x, \partial_y, \partial_z)$, $\Delta = \partial_x^2 + \partial_y^2 + \partial_z^2$. For use in chapters 5 and 6, Eq. ((2.9)) will here be written in the cylindrical coordinate system (r, θ, z). We decompose $\boldsymbol{u} = u_r \boldsymbol{e_r} + u_\theta \boldsymbol{e_\theta} + u_z \boldsymbol{e_z}$ and write (2.9) for the three components,

$$\frac{\partial u_r}{\partial t} + \boldsymbol{u} \cdot \nabla u_r - \frac{u_\theta^2}{r} = -\frac{\partial P}{\partial r} + \nu \left(\Delta u_r - \frac{u_r}{r^2} - \frac{2}{r^2}\frac{u_\theta}{\partial \theta} \right) + F_r \tag{2.12}$$

$$\frac{\partial u_\theta}{\partial t} + \boldsymbol{u} \cdot \nabla u_\theta + \frac{u_\theta u_r}{r} = -\frac{1}{r}\frac{\partial P}{\partial \theta} + \nu \left(\Delta u_\theta - \frac{u_\theta}{r^2} + \frac{2}{r^2}\frac{u_r}{\partial \theta} \right) + F_\theta \tag{2.13}$$

$$\frac{\partial u_z}{\partial t} + \boldsymbol{u} \cdot \nabla u_z = -\frac{\partial P}{\partial z} + \nu \Delta u_z + F_z \tag{2.14}$$

with

$$\boldsymbol{u} \cdot \nabla = u_r \frac{\partial}{\partial r} + \frac{u_\theta}{r}\frac{\partial}{\partial \theta} + u_z \frac{\partial}{\partial z},$$

and

$$\Delta = \frac{1}{r}\frac{\partial}{\partial r}\left(r \frac{\partial}{\partial r} \right) + \frac{1}{r^2}\frac{\partial^2}{\partial \theta^2} + \frac{\partial^2}{\partial z^2} = \frac{\partial^2}{\partial r^2} + \frac{1}{r}\frac{\partial}{\partial r} + \frac{1}{r^2}\frac{\partial^2}{\partial \theta^2} + \frac{\partial^2}{\partial z^2},$$

and incompressibility

$$\frac{1}{r}\frac{\partial r u_r}{\partial r} + \frac{1}{r}\frac{\partial u_\theta}{\partial \theta} + \frac{\partial u_z}{\partial z} = 0. \tag{2.15}$$

Obviously, the dynamics of the flow do not depend on the choice of the coordinate system. We stress however that in the cylindrical formulation, the different components are not interacting in the same manner as in the Cartesian system. For instance, focusing on the left hand side of Eqs. (2.12)-(2.14), it is observed that the toroidal component u_θ and the radial component u_r of the velocity are coupled by terms $-u_\theta^2/r$ and $u_\theta u_r/r$, allowing for a direct energy transfer between the components, even in the absence of gradients. This transfer will play a major role later on in this thesis, where axisymmetric turbulence will be considered.

2.2.2 The evolution of vorticity.

Vorticity $\boldsymbol{\omega}$ is defined as the curl of the velocity. It represents the local rotation rate of the flow,

$$\boldsymbol{\omega} = \nabla \times \boldsymbol{u}. \tag{2.16}$$

The equation for the evolution of vorticity can be derived by taking the curl of (2.9).[1]

$$\frac{\partial \boldsymbol{\omega}}{\partial t} - \nabla \times (\boldsymbol{u} \times \boldsymbol{\omega}) = \nu \nabla^2 \boldsymbol{\omega} + \nabla \times \boldsymbol{F}$$

so that we obtain the equation for the vorticity [2]

$$\frac{\partial \boldsymbol{\omega}}{\partial t} + \boldsymbol{u} \cdot \nabla \boldsymbol{\omega} = \boldsymbol{\omega} \cdot \nabla \boldsymbol{u} + \nu \nabla^2 \boldsymbol{\omega} + \nabla \times \boldsymbol{F} \tag{2.17}$$

The vortex stretching term $\boldsymbol{\omega} \cdot \nabla \boldsymbol{u}$ is often mentioned as the cause of turbulence, or the energy cascade. It represents the elongation of vortices (more particularly vortex tubes) caused by strain. This stretching induces an energy transfer between different lengthscales in a flow, and intensifies the local enstrophy. It can be noticed that the elongation of vortices is only possible in a 3D domain.

We can curl once more to obtain,

$$\nabla \times \boldsymbol{\omega} = \nabla \times \nabla \times \boldsymbol{u} = -\Delta \boldsymbol{u}, \tag{2.18}$$

Even though it is not directly intuitive what the curl of the curl represents, this quantity plays an important role in the viscous dissipation of enstrophy.

2.2.3 Advection-diffusion in fluid flow

An important concept in this thesis will be the advection of a scalar field. In fluid dynamics typical advected scalars are the temperature field, the density field of an immiscible liquid or the concentration of a chemical species. The evolution of a scalar field ϕ in a flow can be described by the advection-diffusion equation:

$$\frac{\partial \phi}{\partial t} + \boldsymbol{u} \cdot \nabla \phi = \nabla \cdot (D \nabla \phi) + Q, \tag{2.19}$$

with the D diffusion coefficient and Q a source term. Even though the scalar equation is linear, the scalar field is in general characterized by an interesting multi-scale behavior, reflecting the mode coupling by the advection term. The statistical characterization of a scalar field in a turbulent flow is therefore not a trivial task.

In Chap. 4 we will use the fact that the same equation governs the dynamics of the third component of a 2D3C velocity field.

---

[1]

$$\boldsymbol{u} \cdot \nabla \boldsymbol{u} = \frac{1}{2} \nabla (|\boldsymbol{u}|^2) - \boldsymbol{u} \times (\nabla \times \boldsymbol{u}) = \frac{1}{2} \nabla (|\boldsymbol{u}|2) - \boldsymbol{u} \times \boldsymbol{\omega}$$
$$\nabla \times \nabla f = 0 \quad \forall f$$
$$\Rightarrow \nabla \times (\boldsymbol{u} \cdot \nabla \boldsymbol{u}) = -\nabla \times (\boldsymbol{u} \times \boldsymbol{\omega})$$

[2]

$$\nabla \times (\boldsymbol{u} \times \boldsymbol{\omega}) = (\nabla \cdot \boldsymbol{\omega}) \boldsymbol{u} - (\nabla \cdot \boldsymbol{u}) \boldsymbol{\omega} + \boldsymbol{u} \cdot \nabla \boldsymbol{\omega} - \boldsymbol{\omega} \cdot \nabla \boldsymbol{u}$$
$$\nabla \cdot \boldsymbol{\omega} = \nabla \cdot \nabla \times \boldsymbol{u} = 0 \text{ and } \nabla \cdot \boldsymbol{u} = 0$$
$$\Rightarrow \ \nabla \times (\boldsymbol{u} \times \boldsymbol{\omega}) = \boldsymbol{u} \cdot \nabla \boldsymbol{\omega} - \boldsymbol{\omega} \cdot \nabla \boldsymbol{u}$$

2.2.4 Dimensionless representation of the equations

The dynamics of physical phenomena are often characterized using non-dimensional control parameters. If the governing equations are known, a proper non-dimensionalization allows often to isolate the important physical quantities in a system. For instance, the Navier-Stokes equations (for constant density), can be transformed into a non-dimensional equation using a velocity scale U and a length scale L (note that alternative quantities, containing the dimensions length and time could also be used). Rescaling all velocities $u^* = u/U$ all derivatives $\nabla^* = L\nabla$, time $t^* = tU/L$ and $P^* = P/U^2$, the Navier-Stokes equations write in dimensionless form

$$\frac{\partial \boldsymbol{u}^*}{\partial t^*} + \boldsymbol{u}^* \cdot \nabla^* \boldsymbol{u}^* = -\nabla P^* + \frac{1}{Re}(\nabla^*)^2 \boldsymbol{u}^* + \boldsymbol{F}^*. \tag{2.20}$$

The advection term $(\boldsymbol{u}^* \cdot \nabla^* \boldsymbol{u}^*)$ is the cause of the turbulence. Indeed, in its absence, all other terms, of linear nature, do not allow different length scales to couple and no chaos, nor multiscale physics will be observed. The relative magnitude of the advection term allows therefore to measure the intensity of the origin of turbulence. On the contrary viscosity helps to suppress the turbulence, through the diffusion and damping of fluctuations.

The relative intensity of advection and viscous friction can thereby indicate if the flow is laminar or turbulent. Indeed, comparing the relative intensity of the advection term with the diffusive term one finds the Reynolds number Re [2], which was introduced in Eq. (2.1),

$$Re = \frac{\text{advection of momentum}}{\text{viscous diffusion of momentum}} = \frac{\mathcal{O}(\boldsymbol{u} \cdot \nabla \boldsymbol{u})}{\mathcal{O}(\nu \Delta \boldsymbol{u})}, \tag{2.21}$$

where $\mathcal{O}$ indicates 'order of magnitude'. Replacing these terms by the dimensionless representation in (2.20), it is observed that one retrieves that the dimensionless terms scale as Eq. (2.1),

$$Re = \frac{uL}{\nu} \tag{2.22}$$

Analogously the Péclet number Pe can be defined as the ratio of the scalar field advection and diffusion:

$$Pe = \frac{uL}{D} \tag{2.23}$$

and is similarly associated with the advection-diffusion equation (2.19). The ratio of the scalar diffusivity and the kinematic viscosity is determined by the Schmidt number Sc.

$$Sc = \frac{\nu}{D} \tag{2.24}$$

If the scalar field is the temperature the non-dimensional parameter is the Prandtl number Pr.

2.3 Integral quantities

Integral quantities are defined here as the total value of a field, integrated over the flow domain. In the following we will discuss energy, enstrophy, scalar variance, palinstrophy and helicity. The most important integral quantities in our study, are those which are conserved by the dynamics if external forces and viscosity are set to zero. These quantities are called invariants in the following.

2.3.1 Kinetic energy.

During this study we will repeatedly focus on energy transfer. The equation for the pointwise kinetic energy density $e(\boldsymbol{x}, t) = \frac{1}{2}|\boldsymbol{u}|^2$ can be deduced from the momentum equation by taking the inner-product of (2.9) and $\boldsymbol{u}$, resulting in the expression

$$\frac{\partial e}{\partial t} + \boldsymbol{u} \cdot (\boldsymbol{u} \cdot \nabla \boldsymbol{u}) = \boldsymbol{u} \cdot \nabla P + \nu \boldsymbol{u} \cdot \Delta \boldsymbol{u} + \boldsymbol{u} \cdot \boldsymbol{F} \tag{2.25}$$

with

- $\boldsymbol{u} \cdot (\boldsymbol{u} \cdot \nabla \boldsymbol{u}) = \nabla \cdot (e\boldsymbol{u})$ [3] is the divergence the kinetic energy density flux $e\boldsymbol{u}$.
- $\nu \boldsymbol{u} \cdot \Delta \boldsymbol{u} = \nu \Delta e - \nu |\nabla \boldsymbol{u}|^2$ [4] is the ensemble of viscous energy dissipation and viscous diffusion of kinetic energy.
- $\boldsymbol{u} \cdot \boldsymbol{F}$ is the energy injection rate induced by the body forces.

Regrouping the divergence of the different fluxes, the kinetic energy evolution can be rewritten as,

$$\frac{\partial e}{\partial t} = -\nabla \cdot [(P + e)\, \boldsymbol{u} - \nu \boldsymbol{u} \times \boldsymbol{\omega}] - \nu |\boldsymbol{\omega}|^2 + \boldsymbol{u} \cdot \boldsymbol{F}. \tag{2.26}$$

This formulation immediately shows that if there are no fluxes into, or out of the flow domain, the total kinetic energy is entirely governed by the integral of the last two terms. Mathematically this is shown by eliminating the divergence terms using the Green-Ostrogradski theorem

$$\int_{\mathbb{R}^3} \nabla \cdot \boldsymbol{f} \, \mathrm{d}\boldsymbol{r} = \oint_{\mathbb{R}^2} \boldsymbol{f} \cdot \, \mathrm{d}\boldsymbol{r}, \tag{2.27}$$

in the case of periodic or Dirichlet boundaries.

Indeed, introducing the total kinetic energy,

$$E = \int_{\mathbb{R}^3} e \mathrm{d}\boldsymbol{r}, \tag{2.28}$$

we obtain for its temporal evolution for such boundary conditions,

$$\frac{\mathrm{d}E}{\mathrm{d}t} = I - \varepsilon \tag{2.29}$$

with

$$I = \int_{\mathbb{R}^3} \boldsymbol{u} \cdot \boldsymbol{F} \, \mathrm{d}\boldsymbol{r} \tag{2.30}$$

---

[3]

$$(\boldsymbol{u} \times \boldsymbol{\omega}) \perp \boldsymbol{u} \;\Rightarrow \boldsymbol{u} \cdot (\boldsymbol{u} \times \boldsymbol{\omega}) = 0$$
$$\Rightarrow \boldsymbol{u} \cdot (\boldsymbol{u} \cdot \nabla \boldsymbol{u}) = \boldsymbol{u} \cdot \nabla \left(\frac{1}{2} |\boldsymbol{u}|^2 \right)$$

[4]

$$\Delta \boldsymbol{u} = \nabla (\nabla \cdot \boldsymbol{u}) - \nabla \times (\nabla \times \boldsymbol{u}) = -\nabla \times \boldsymbol{\omega}$$
$$\Rightarrow \boldsymbol{u} \cdot (\boldsymbol{u} \cdot \nabla \boldsymbol{u}) = -\boldsymbol{u} \cdot (\nabla \times \boldsymbol{\omega}) = \nabla \cdot (\boldsymbol{u} \times \boldsymbol{\omega}) - \boldsymbol{\omega} \cdot (\nabla \times \boldsymbol{u})$$

and $\varepsilon = 2\nu W$ with the global enstrophy W defined by

$$W = \int_{\mathbb{R}^3} \omega^2 \, \mathrm{d}\boldsymbol{r}. \tag{2.31}$$

The energy balance (2.29) reflects the variation of total kinetic energy caused by viscous dissipation and external energy injection. As ε is always positive, the total kinetic energy decreases without energy injection. For a stationary state all energy I injected is dissipated at a rate ε. In the absence of external forcing and viscous stress, energy is thus conserved by the system. This means that kinetic energy is an invariant of the system.

2.3.2 Enstrophy

An interesting observation is that the dissipation of energy is, in total, proportional to the total enstrophy. The local enstrophy $w = \omega^2/2$ evolves as

$$\frac{\partial w}{\partial t} + \nabla \cdot (w\boldsymbol{u}) = \boldsymbol{\omega} \cdot (\boldsymbol{\omega} \cdot \nabla \boldsymbol{u}) + \nu \boldsymbol{\omega} \cdot \nabla^2 \boldsymbol{\omega} + \boldsymbol{\omega} \cdot \boldsymbol{F}_{\boldsymbol{\omega}} \tag{2.32}$$

with $\boldsymbol{F}_{\boldsymbol{\omega}} = \nabla \times \boldsymbol{F}$ the curl of the forcing term. Integrating over the flow domain, the total enstrophy is evolving as

$$\frac{\mathrm{d}W}{\mathrm{d}t} = P_{VS} - \varepsilon_w + I_w \tag{2.33}$$

where

$$I_w = \int_{\mathbb{R}^3} \boldsymbol{\omega} \cdot \boldsymbol{F}_{\boldsymbol{\omega}} \, \mathrm{d}\boldsymbol{r} \tag{2.34}$$

$$P_{VS} = \int_{\mathbb{R}^3} \boldsymbol{\omega} \cdot (\boldsymbol{\omega} \cdot \nabla \boldsymbol{u}) \, \mathrm{d}\boldsymbol{r} \tag{2.35}$$

$$\varepsilon_w = 2\nu B, \tag{2.36}$$

the palinstrophy B in the system being defined by

$$B = \int_{\mathbb{R}^3} |\nabla \times \boldsymbol{\omega}|^2 \, \mathrm{d}\boldsymbol{r} \tag{2.37}$$

This evolution is somewhat similar to the kinetic energy balance, with an injection term associated with the external forcing and a viscous dissipation term. However, the extra term, representing the influence of the vortex stretching adds an additional, internal, source of enstrophy to the system P_{VS}. Because of this term, enstrophy is not an invariant of the 3D Navier-Stokes equations, since it is not constant in the absence of forcing and dissipation. However, and we will come back to this, vortex stretching is identically zero in two-dimensional turbulence, making enstrophy an invariant of the two-dimensional Navier-Stokes equations.

2.3.3 The scalar variance, or scalar "energy".

A global quadratic quantity ϕ^2 can be constructed for a scalar. Like for the energy, the total scalar's variance S is given by

$$S = \int_{\mathbb{R}^3} \phi^2 \, \mathrm{d}V$$

As for the total kinetic energy, variations of S are caused by a dissipation term ε_S and an external injection P_S.

$$\frac{\mathrm{d}S}{\mathrm{d}t} = \varepsilon_S + P_S \tag{2.38}$$

with the dissipation

$$\varepsilon_S = D \int_{\mathbb{R}^3} |\nabla \phi|^2 \, \mathrm{d}\boldsymbol{r} \tag{2.39}$$

so that S is an invariant of the system, since it is conserved in the case of zero diffusivity D and zero injection.

2.3.4 Helicity

E, W and S are quadratic quantities obtained by squaring and integrating a vector or a scalar field. But quadratic quantities can also be formed by the product of different quantities. For instance we can consider the inner product of the velocity field $\boldsymbol{u}$ and the vorticity field $\boldsymbol{\omega}$. For all positions $\boldsymbol{x}$ one can define a scalar field named kinetic helicity h

$$h(\boldsymbol{x}) = \boldsymbol{u}(\boldsymbol{x}) \cdot \boldsymbol{\omega}(\boldsymbol{x}) \tag{2.40}$$

More precisely helicity is a pseudo-scalar, since its sign changes under symmetry (vorticity $\boldsymbol{\omega}$ is itself a pseudo-vector). Pioneering studies of helicity were proposed by Moreau [9] and Moffatt [10] who proposed the name "helicity" by analogy with the helicity of a particle in quantum physics. More generally helicity defines the cross-product of a vector field with its curl (notably in electromagnetism). Helicity was introduced as a tool to describe the topology of the flow, as it is a measure the degree of knottedness of the vortex lines of the flow, or as a measure of the chirality of the flow. It plays a role in dynamo action [11] and we will discuss this further in Chap. 7.

The dynamic evolution of helicity is obtained by multiplying (2.9) with $\boldsymbol{\omega}$ and (2.17) with $\boldsymbol{u}$ and adding them

$$\frac{\partial h}{\partial t} + \boldsymbol{u} \cdot \nabla h = -\nabla(P\boldsymbol{\omega}) + \boldsymbol{u} \cdot (\boldsymbol{\omega} \cdot \nabla \boldsymbol{u}) + \nu[\boldsymbol{\omega} \cdot \Delta \boldsymbol{u} + \boldsymbol{u} \cdot \Delta \boldsymbol{\omega}] + F_h \tag{2.41}$$

with $F_h = \boldsymbol{u} \cdot \boldsymbol{F}_\omega + \boldsymbol{\omega} \cdot \boldsymbol{F}$. The total helicity H is defined as

$$H = \int_{\mathbb{R}^3} h \, \mathrm{d}\boldsymbol{r}.$$

Since the vorticity and velocity are divergence free $\boldsymbol{u} \cdot (\boldsymbol{\omega} \cdot \nabla \boldsymbol{u}) = \nabla(e\boldsymbol{\omega})$ so that

$$\frac{\mathrm{d}H}{\mathrm{d}t} = I_h + \epsilon_h \tag{2.42}$$

with

$$I_h = \int_{\mathbb{R}^3} F_h \, \mathrm{d}\boldsymbol{r} \tag{2.43}$$

and

$$\epsilon_h = \int_{\mathbb{R}^3} \nu[\boldsymbol{\omega} \cdot \Delta \boldsymbol{u} + \boldsymbol{u} \cdot \Delta \boldsymbol{\omega}] \, \mathrm{d}\boldsymbol{r}. \tag{2.44}$$

We see thus that helicity is again an invariant if $\boldsymbol{F} = 0$ and $\nu = 0$.

The relative/normalised helicity h_{rel} is in the following considered, to estimate the strength of the correlation between the velocity field and the vorticity field,

$$H_{rel}(\boldsymbol{x}) = \frac{H}{\sqrt{2EW}} \tag{2.45}$$

In case of a Beltrami flow

$$\boldsymbol{\omega} = \lambda \boldsymbol{u} \tag{2.46}$$

we have $H_{rel} = 1$. An interesting feature is that the nonlinearity is zero in a Beltrami flow.

The interpretation of helicity as a measure of correlation between fields can be straightforward to generalize helicity over other quantities which link two fields. For instance it can be interesting to study how a scalar field can be entangled with vortices of a flow, and the influence of this correlation on the evolution of the scalar's variance. For this reason the scalar helicity can be introduced as a pseudoscalar by mimicking the kinetic helicity.

$$h_S = \sum_i \phi \omega_i \tag{2.47}$$

This quantity is called the skew-diffusion [12]. It will be shown that the skew-diffusion is intimately linked to the (kinetic) helicity, in particular in Chapter 7.

2.4 Homogeneous isotropic turbulence

The most commonly studied flow in theoretical studies of turbulence is, as we said, homogeneous (invariance of the properties by translation) and isotropic (invariance under rotation) turbulent flow, or HIT. More specifically, a turbulent flow can be only *statistically* homogeneous or/and isotropic. Therefore, in the remainder of this thesis homogeneity, isotropy and stationarity are tacitly understood in the statistical sense. The ergodic assumption considers an equivalence between spatial, time and ensemble average in HIT.

2.4.1 Correlation functions and spectra

The study of turbulence can be performed by studying the turbulent structures in a flow. As in other domains in physics, correlation functions can be used to estimate how different points of a field are correlated. One can then establish a hierarchy between structures by illustrating the distribution of energy over the different eddy sizes of the flow. For that, a useful statistical function is the two-point correlation function R_{ij}, defined as

$$R_{ij}(\boldsymbol{r}, \boldsymbol{x}, t) = \overline{u_i(\boldsymbol{x}, t) u_j(\boldsymbol{x} + \boldsymbol{r}, t)} = R_{ij}(r, t), \tag{2.48}$$

where the bar $\bar{\cdot}$ denotes an ensemble average. The two-point correlation function is independent of the position $\boldsymbol{x}$ for a homogeneous flow, and assuming isotropy there is no dependence on the direction of the vector $\boldsymbol{r}$. So $R_{ii}(r, t)$ gives directly an evaluation of the energy for points separated by a distance r associated with the energy of eddies of size r.

We can notice that

$$R_{ii}(\boldsymbol{r} = 0, t) = \overline{u_i(\boldsymbol{x}, t) u_i(\boldsymbol{x}, t)} = 2E(t). \tag{2.49}$$

Studies of the dynamics of structures at different lenght scales in physical space can be performed using R_{ij}. Different length scales such as the longitudinal and transversal integral length scales can, for instance, be introduced using R_{ij}, which describe, in general the large, energetic structures in a flow.

In order to study interactions and energy transfers between different scales of a flow, it can be useful to use Fourier transformations $\mathcal{F}$. For instance the Fourier transform $\hat{u}$ of the velocity can be defined as

$$\mathcal{F}[u(\boldsymbol{x},t)] = \hat{u}(\boldsymbol{k},t) = \frac{1}{(2\pi)^d}\int_{\mathbb{R}^3} u(\boldsymbol{x},t)e^{-i\boldsymbol{k}.\boldsymbol{x}}\mathrm{d}^3\boldsymbol{k}, \tag{2.50}$$

with d the dimension of space. The vector $\boldsymbol{k}$ is the Fourier mode (simply mode in the following). The wavenumber $k = |\boldsymbol{k}|$ is an inverse of a lenght l. It allows to work directly with the scales l of the turbulent eddies instead of the distance r and position $\boldsymbol{x}$, which is very useful if we want to know the distribution of the energy over the different eddy sizes.

A convenient mathematical property of Fourier transformations is the ability to transpose differential operators to algebraic operators, which is particularly useful for their numerical treatment as shown in Chapter 3.

$$\mathcal{F}[\partial_i f] = ik_i\hat{f} \qquad \mathcal{F}[\nabla\cdot\boldsymbol{u}] = i\boldsymbol{k}\cdot\boldsymbol{u} \qquad \mathcal{F}[\nabla\times\boldsymbol{u}] = i\boldsymbol{k}\times\hat{\boldsymbol{u}} \qquad \mathcal{F}[\Delta\boldsymbol{u}] = -k^2\hat{\boldsymbol{u}}. \tag{2.51}$$

The spectral tensor Φ_{ij} is defined as the Fourier transform of the two-point correlation function R_{ij},

$$\Phi_{ij}(\boldsymbol{k},t) = \frac{1}{(2\pi)^d}\int_{\mathbb{R}^3} R_{ij}(\boldsymbol{r},t)e^{-i\boldsymbol{k}\cdot\boldsymbol{r}}\mathrm{d}\boldsymbol{r}.$$

More particularly

$$R_{ii}(\boldsymbol{r}=0,t) = 2E = \int_{\mathbb{R}^3}\Phi_{ii}(\boldsymbol{k},t)\ \mathrm{d}\boldsymbol{k}$$

This shows that $\Phi_{ii}(\boldsymbol{k},t) = |\hat{\boldsymbol{u}}|^2(\boldsymbol{k},t)$ is the energy in each Fourier mode $\boldsymbol{k}$. We can relate this to the energy spectrum $E(k)$, representing the energy at wavenumber k.

$$E(k) = \int_{\mathbb{R}^3}\Phi_{ii}(\boldsymbol{k})\delta(|\boldsymbol{k}|-k)\mathrm{d}\boldsymbol{k} = \int_{\mathbb{R}^3}|\hat{\boldsymbol{u}}|^2\delta(|\boldsymbol{k}|-k)\ \mathrm{d}\boldsymbol{k}$$

$E(k)$ will be one of the main quantities that will be used during this study as its represents the distribution of the energy in each wave number k associated with lengthscales l, by the relation $l \sim 2\pi/k$. In 3D isotropy allows to simplify the integral over wavenumber space by

$$d\boldsymbol{k} \to 4\pi k^2 dk \tag{2.52}$$

and in 2D by

$$d\boldsymbol{k} \to 2\pi k dk. \tag{2.53}$$

Therefore, if energy in Fourier-space is equally distributed over all modes, the kinetic energy spectrum will yield,

$$E(k) \sim k^{d-1} \tag{2.54}$$

Such equilibrium states are not common in real-life turbulence, but they play an important role in statistical mechanics approaches applied to turbulence, as we will discuss in Chapter 4.

The total kinetic energy density can be naturally obtained by summing the energy distributed in each wavenumber k:

$$e = \int_0^\infty E(k)\ \mathrm{d}k$$

The vorticity spectrum $W(k)$ can be obtained from the relation (2.16) and rules (2.51)

$$\boldsymbol{u}(\boldsymbol{k}) = \frac{i}{k^2}\boldsymbol{k} \times \boldsymbol{\omega}(\boldsymbol{k}) \tag{2.55}$$

$$W = \int_0^\infty W(k)\ \mathrm{d}k = \int_0^\infty \mathrm{d}k \int_{\mathbb{R}^3} |\hat{\boldsymbol{\omega}}|^2 \delta(|\boldsymbol{k}| - k)\ \mathrm{d}\boldsymbol{k} = 2\int_0^\infty k^2 E(k)\ \mathrm{d}k. \tag{2.56}$$

2.4.2 Dynamics of the velocity spectrum

The temporal evolution equation of the velocity spectrum $E(k)$, also called Lin's equation, can be obtained from the Fourier transform of the Navier-Stokes equation (2.9), by multiplying by the conjugate $\hat{\boldsymbol{u}}^*(\boldsymbol{k}, t)$ in order to have the equation for $\phi_{ii}(\boldsymbol{k}, t)$ and then integrate over modes $\boldsymbol{k}$ with $|\boldsymbol{k}| = k$, resulting in

$$\frac{\mathrm{d}E(k,t)}{\mathrm{d}t} = T(k,t) - 2\nu k^2 E(k,t) + I(k,t) \tag{2.57}$$

with

$$I(k,t) = \int_{\mathbb{R}^3} \mathcal{R}[\hat{\boldsymbol{u}}^*(\boldsymbol{k},t) \cdot \hat{\boldsymbol{F}}(\boldsymbol{k},t)]\delta(|\boldsymbol{k}| - k)\ \mathrm{d}\boldsymbol{k}$$

and

$$T(k,t) = \int_{\mathbb{R}^3} \mathcal{R}[\hat{\boldsymbol{u}}^*(\boldsymbol{k},t) \cdot \mathcal{F}(\boldsymbol{NL}(\boldsymbol{u}))]\delta(|\boldsymbol{k}| - k)\ \mathrm{d}\boldsymbol{k}$$

with $\mathcal{R}$ real part of complex numbers and where we introduced,

$$\boldsymbol{NL}(\boldsymbol{u}) = \boldsymbol{u} \cdot \nabla \boldsymbol{u} + \nabla P. \tag{2.58}$$

In this expression $T(k,t)$ is the spectral energy transfer function. It represents the spectral transfer of energy from scale k to scale $k + \Delta k$. In general we have $T(k,t) > 0$ for small scales which receive energy and $T(k,t) < 0$ for the largest scales which give their energy, on average. Since the transfer term is not-dissipative or energy-producing (and that is why it is called transfer), in a freely evolving flow all energy must eventually reach the smallest scales where it can be dissipated.

The conservative nature of the flux is mathematically represented by the relation

$$\int_0^\infty T(k,t)\ \mathrm{d}k = 0.$$

An other measure of the energy transfer is the spectral energy flux function $\Pi(k)$ defined by:

$$\Pi(k) = -\int_0^k T(k',t)\ \mathrm{d}k' = \int_k^\infty T(k',t)\ \mathrm{d}k'. \tag{2.59}$$

The spectral energy flux is the cumulative energy transfer of all modes of norm smaller than the wave number k to higher wave numbers, or in the physical space from largest

(larger than $1/k$) to smaller structures. Then Lin's equation (2.57) can be reformulated with the spectral energy flux:

$$\frac{\mathrm{d}E(k,t)}{\mathrm{d}t} = -\frac{\partial \Pi(k,t)}{\partial k} - 2\nu k^2 E(k,t) + I(k,t). \tag{2.60}$$

In Kolmogorov's theory, which will be discussed in the next section, it is assumed that $I(k,t)$ is injected at large scales (small wavenumber k). It means that in the inertial range $I(k,t) = 0$, and for a stationary states:

$$\frac{\partial \Pi(k,t)}{\partial k} = -2\nu k^2 E(k,t) \tag{2.61}$$

Indeed to derive this expression we need to assume that dissipation can be neglected in the inertial range so $(\partial \Pi(k,t))(\partial k) \longrightarrow 0$, which means that the spectral energy flux is constant in the inertial range. It is logically equal to the dissipation rate ϵ and the injection rate for a stationary state. The sign of Π indicates the direction of the energy transfer. For 3D HIT, Π is positive which means that that the transfer goes from small to large wave numbers.

2.4.3 K41 theory

Now that we have defined the convenient tools to investigate multi-scale statistics, we turn to the phenomenological picture of how energy is distributed over scales. The seminal concept of a cascade of energy was formulated poetically by Lewis Fry Richardson in 1922 [3]: *Big whorls have little whorls that feed on their velocity, and little whorls have smaller whorls and so on to viscosity - in the molecular sens.*

The idea behind this poem is that a turbulent flow consists of structures, called eddies. The turbulent energy of the flow is distributed over these eddies. Observations do then suggest that energy goes from the largest-scale structures of the flow to the smallest ones, in a process referred to as a cascade. This mechanism continues until eddies are reached which are small enough so that the viscous friction of the flow can remove them by dissipating their energy.

A statistical characterization of the energy cascade was proposed by Kolmogorov. Kolmogorov's predictions [13] are based on several hypothesis:

- Turbulence is fully developed, which means that there is a sufficient scale range. It means in practice that it requires a fairly large value of the Reynolds number.
- The fluid is locally homogeneous and isotropic, which means that if the flow can have anisotropy at large scales, at sufficient small scales statistical properties are homogeneous and isotropic.
- At sufficient small scales all statistical characteristics are determined only by ϵ and ν. Indeed ϵ remains constant and finite and is determined by large structures as suggested by Taylor [4]
$$\epsilon \sim u^3/L. \tag{2.62}$$
- At sufficient small scales the flow shows a self-similarity at all scales. This self-similarity depends only on ϵ and the length scale l (or the wave number k in spectral space).

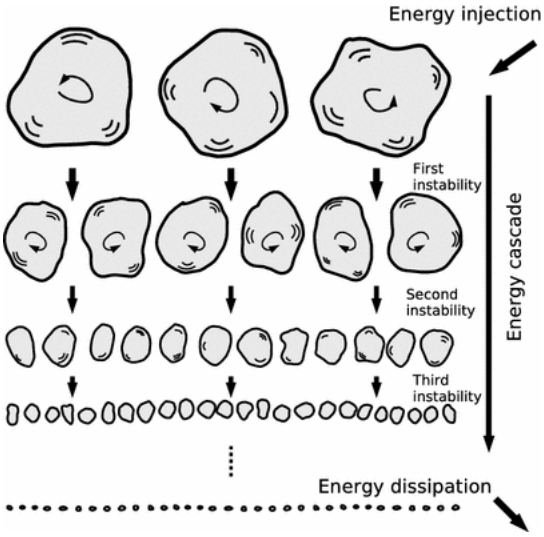

Figure 2.2: Illustration of the energy cascade[1]

The scale range in which Kolmogorov's assumptions can be applied is called the inertial range. For smaller scales viscosity becomes too effective. These assumptions are very useful because it means that parameters of the flow at small scales are combinations of ν and ϵ and can be found with dimensional analysis. These parameters are called Kolmogorov parameters. For instance

$$\eta = \left(\frac{\nu^3}{\epsilon}\right)^{1/4}$$

is Kolmogorov's length scale and characterizes the typical length scale where viscous diffusion dominates the dynamics. Energy cascade from large to small scales until eddies size reaches η. Wave numbers larger than $k_\eta = 1/\eta$ are said to be in the dissipative range.

For an isotropic flow ϵ one can derive [4] that

$$\epsilon = 15\nu\overline{\left(\frac{\partial u_i}{\partial x_j}\right)^2} \tag{2.63}$$

The self-similarity of the flow can be used to find a law for the scale by scale energy partition. Indeed this means that $u(l) \propto l^p\epsilon^q$. Equivalently in the spectral domain we have $E(k) = C\epsilon^q k^p$

With $\epsilon \approx u_l^3/l$, $E_l \approx u_l^2 \approx kE(k)$ the energy of l-size eddies with $l \approx 1/k$ we can obtain the Obukhov-Kolmogorov scaling law for 3D turbulence.

$$E(k) = C\epsilon^{2/3}k^{-5/3}. \tag{2.64}$$

Kolmogorov himself proposed a correction to this scaling [14], taking into account spatial fluctuations of the dissipation rate, but the resulting corrections to the energy spectrum turn out to be small and will not be of interest in our investigation.

2.5 Turbulence in less than three dimensions

Certain flows in nature are so anisotropic that their dynamics are close to two-dimensional. This two dimensionality is either caused by geometrical factors, body forces (such as

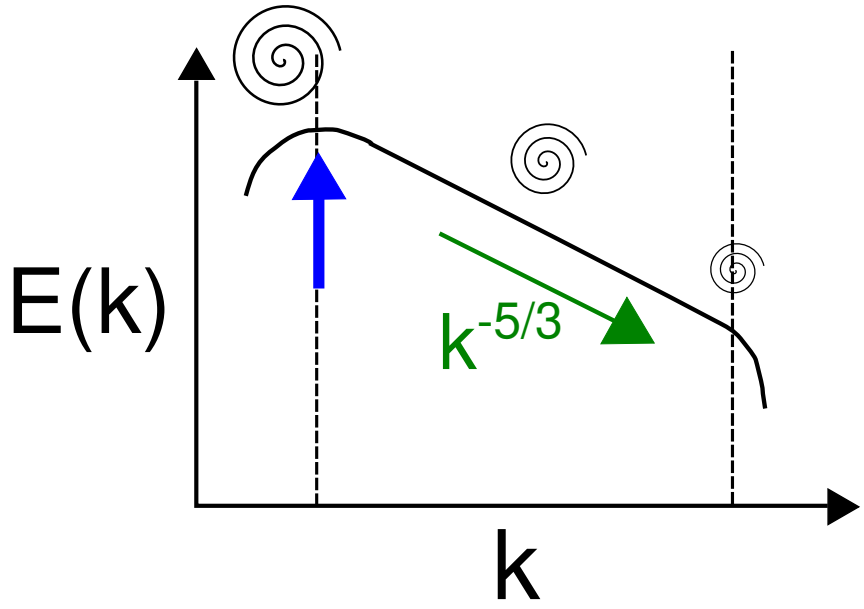

Figure 2.3: Theoretical energy spectrum $E(k)$ according to Kolmogorov's theory, resulting from a conserved energy flux through scale space.

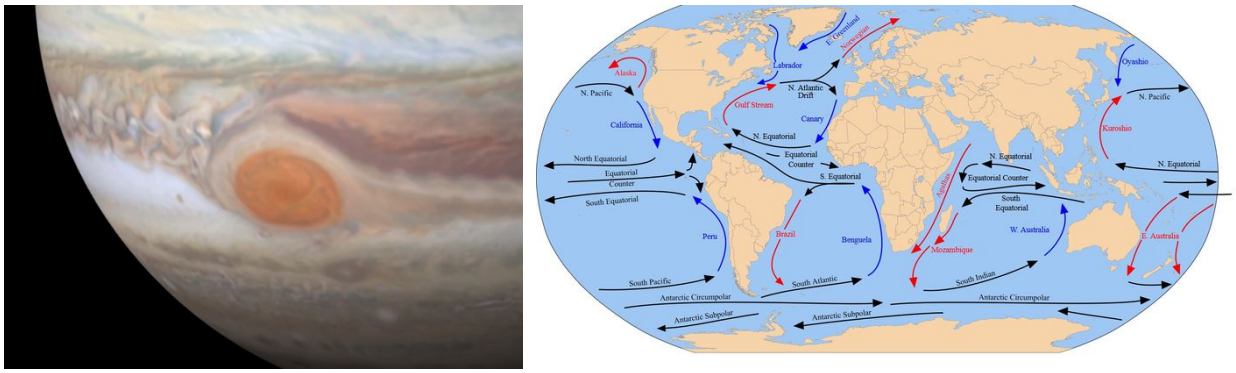

(a) (b)

Figure 2.4: Two examples of long-time coherent, close to 2D flow patterns. (a) Jupiter's red spot. (b) The oceanic currents on the Earth.

rotation, stratification or magnetic fields [15]), or both. Historically 2D turbulence was proposed with the purpose to explain large coherent and stable structures in the atmosphere. This self-organisation, like for oceanic currents, is caused by two phenomena: the Coriolis acceleration caused by the Earth's rotation [16, 17, 18, 19], and the density stratification of the atmosphere. Indeed oceanographic and atmospheric turbulent flows are self-organised thin layers (See e.g. Fig. 2.4), resulting in a confinement in the vertical direction of the flow.

Artificial two-dimensional flows can also be created, notably in conducting flows like liquid metals and plasma. In the presence of a magnetic field [20, 16] flows become almost invariant along the magnetic field direction [21], allowing the dynamics perpendicular to the field to be close to two-dimensional. This effect has been studied numerically [22, 23, 24] and experimentally [25]. These flows have therefore two dimensions of variation, but three velocity components, since the dynamics along the field are not constrained.

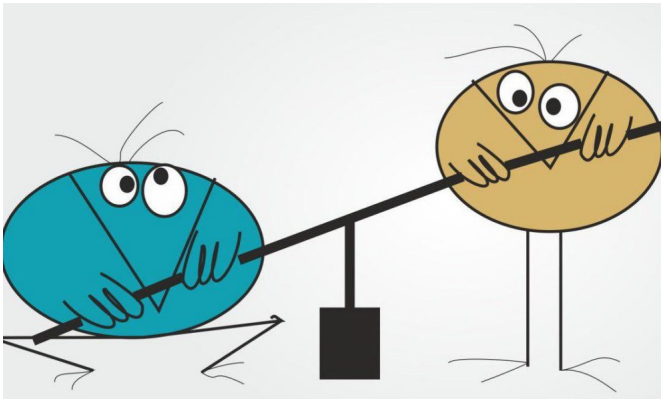

Figure 2.5: In the world of the Shadoks there is no direct energy cascade! Indeed, as stated in Wikipedia: *"Dans le monde des Shadoks, l'espace est représenté comme un plan et, comme tel, il est plat. Il n'a donc pas de profondeur (comme tout l'univers shadokéen), seulement le haut et le bas, la gauche et la droite"*. This particularity can partially explain the specificities observed on planet Shadok.

In the following we will first discuss 2D turbulence and after that we consider the just mentioned 2D3C flows. These latter will be considered in both Cartesian and cylindrical coordinate systems.

2.5.1 2D turbulence

A perfectly two-dimensional turbulent flow is a turbulent flow which is restricted to a plane. It can be described with two geometrical directions. In such flows the velocity field has only two components which only vary in the two coordinate directions. Such two-dimensional turbulent flow is somewhat theoretical in our three-dimensional world and seems particularly interesting for Shadoks (see Fig. 2.5).

Nevertheless, strong confinement in one direction, or the effect of certain body forces allows to observe close to two-dimensional turbulence. Examples are rapidly rotating turbulence, atmospheric and oceanic flows at large length scales and magnetically confined plasmas in the plane perpendicular to the magnetic field. Reviews on 2D turbulence are [26, 27, 28, 29].

An important feature, distinguishing it from 3D turbulence is that it is characterised by an inverse energy cascade. This means that a 2D flow shows a tendency to transfer energy, injected at a certain scale, to larger scales. This is the opposite kind of cascade compared to 3D turbulence. Nevertheless, 2D turbulence possesses also a direct cascade, but of enstrophy, not of energy.

The inverse cascade allows to self-organize a flow into large structures. This difference between 2D and 3D turbulence with respect to the energy transfer was already pointed out by Ogura [30] and Fjortoft [31]. The presence of the inverse energy cascade implies that in the world of the Shadoks a turbulent flow is characterized by large scale structures. That is totally different from the Richardson cascade which causes the fragmentation of eddies to form smaller vortices in 3D.

Particularities of two-dimensional turbulence were quantitatively studied by Kraichnan [7], Leith [32] and Batchelor [33]. The so-called KLB model predicts the shape of the

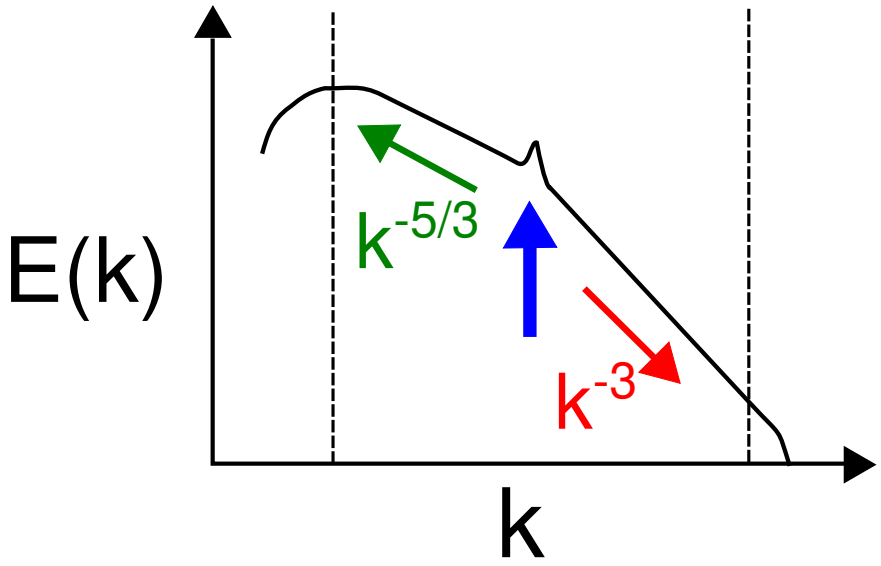

Figure 2.6: Energy spectrum for a two-dimensional flow

energy spectrum for an energy injected at the wavenumber k_i:

$$E_{k<ki}(k) = C_e \epsilon^{2/3} k^{-5/3} \qquad E_{k>k_i}(k) = C_w \beta^{2/3} k^{-3}, \tag{2.65}$$

where $\beta = 2\nu B$ is the enstrophy-dissipation rate.

The energy spectrum in 2D is related to two distinct conservative quadratic quantities. In 2D the vorticity has only one non-zero component, and the helicity is zero,

$$\boldsymbol{\omega} = \nabla \times \boldsymbol{u}_\perp = \omega_z \boldsymbol{e_z} \Longrightarrow h = \boldsymbol{u}_\perp \cdot \boldsymbol{e_z} \omega_z = 0, \tag{2.66}$$

with $\boldsymbol{u} = \boldsymbol{u}_\perp = u_x \boldsymbol{e_x} + u_y \boldsymbol{e_y}$.

We will now discuss the equations for two dimensional velocity and vorticity. The two-dimensional velocity field is governed by

$$\frac{\partial \boldsymbol{u}_\perp}{\partial t} + \boldsymbol{u}_\perp \cdot \nabla \boldsymbol{u}_\perp = -\nabla P + \nu \Delta \boldsymbol{u}_\perp. \tag{2.67}$$

with $\partial_x u_x + \partial_y u_y = 0$. For the vorticity this yields

$$\frac{\partial \omega_z}{\partial t} + \boldsymbol{u}_\perp \cdot \nabla \omega_z = \nu \Delta \omega_z. \tag{2.68}$$

One can notice that the evolution of the vorticity, represented by a scalar field, is governed by an advection-diffusion equation, as Eq. (2.19). Without the vortex stretching term[5] the vorticity is indeed simply advected by the two-dimensional velocity field. However, it is not a passive scalar field since its value is tied to the velocity by the relation $\omega_z = (\nabla \times \boldsymbol{u}_\perp) \cdot \boldsymbol{e}_z$.

Mathematically since incompressible two-dimensional turbulence has two components and incompressibility constrains its movement, the whole dynamics can be described conveniently by a single scalar field, the stream-function. We define the stream function ψ such that

$$u_x = -\frac{\partial \psi}{\partial y} \qquad u_y = \frac{\partial \psi}{\partial x} \tag{2.69}$$

[5] Vortex stretching $\boldsymbol{\omega} \cdot \nabla \boldsymbol{u} = \omega_z \partial_z \boldsymbol{u}_\perp = 0$

With this definition ψ verifies the incompressibility equation (2.5). An other interesting property is the relation with the vorticity: $\omega_z = -\Delta\psi$. These relations allow to reduce (2.67) to an equation for ψ. Indeed [6] we obtain

$$\frac{\partial \psi}{\partial t} + \Delta^{-1}[\psi, -\Delta\psi] = \nu \Delta \psi \tag{2.70}$$

or, using this notation, the vorticity equation reads

$$\frac{\partial \omega_z}{\partial t} + [\psi, \omega_z] = \nu \Delta \omega_z. \tag{2.71}$$

with

$$[f, g] = \frac{\partial f}{\partial x}\frac{\partial g}{\partial y} - \frac{\partial f}{\partial y}\frac{\partial g}{\partial x} \tag{2.72}$$

(also called Poisson bracket) and more particularly $\boldsymbol{u}_\perp \cdot \nabla f = [\psi, f]$.

The fact that the vorticity is governed by an advection equation shows that enstrophy is conserved in a 2D flow in the absence of dissipation. As for the energy, it leads to a constant positive enstrophy flux in the range $k_i > k$, associated with a direct enstrophy cascade which ends in a dissipation range governed by the palinstrophy. For $k < k_i$, the energy flux is again constant which gives again the $-5/3$ scaling, but the flux is negative which corresponds to an inverse cascade.

Asymptotically, the energy flux is negligible in the direct enstrophy cascade and so is the enstrophy flux in the inverse energy cascade. The KLB model was early numerically tested by Lilly for forced [34] and decaying turbulence [35], and later confirmed [36, 37, 38]. Experiments also confirmed the presence of the inverse energy cascade [39, 40].

The energy spectrum in the enstrophy cascade range has been modified by Kraichnan [41] with a logarithmic correction, in order to account for the divergence of the enstrophy when integrating the enstrophy spectrum. This correction to the spectrum (2.65) leads to

$$E_{k>k_i}(k) = C\beta^{2/3}k^{-3}\left[\ln\left(\frac{k}{k_{max}}\right)\right]^{-1/3}. \tag{2.73}$$

Thereby the enstrophy flux is constant, but the scaling is no pure power law anymore. Moreover several numerical studies still show a steeper slope than $-5/3$ of the energy spectrum in the inverse cascade and the precise value exponent remains a debated subject.

2.5.2 Cartesian two-dimensional three-component (2D3C) flow

We consider a flow which is two-dimensional turbulence but needs three scalar equations to be fully described. In practice this corresponds to the asymptotic limit of very strongly anisotropic flow as, for instance generated by strong rotation or the presence of a strong magnetic field.

To understand this definition it can be interesting to study the Navier-Stokes equations in a flat Cartesian coordinate system. We consider that the dynamics of all

[6]
$$\boldsymbol{u} \cdot \nabla f = u_x \frac{\partial f}{\partial x} + u_y \frac{\partial f}{\partial y} = -\frac{\partial \psi}{\partial y}\frac{\partial f}{\partial x} + \frac{\partial \psi}{\partial x}\frac{\partial f}{\partial y}$$

components are invariant along the third direction, $\partial_z = 0$ yielding:

$$\begin{cases} \dfrac{\partial \boldsymbol{u}_\perp}{\partial t} + \boldsymbol{u}_\perp \cdot \nabla \boldsymbol{u}_\perp = -\nabla P + \nu \Delta \boldsymbol{u}_\perp \\ \\ \dfrac{\partial u_z}{\partial t} + \boldsymbol{u}_\perp \cdot \nabla u_z = \nu \Delta u_z \end{cases} \tag{2.74}$$

As for the vorticity in 2D2C flows, the third velocity component can be seen as a scalar field advected by the flow. The total kinetic energy is still conserved, which is also the case for both horizontal and vertical components individually. The dynamics of u_z are then equivalent to those governing a passive scalar, advected by two-dimensional, at unity Prandtl number. It can be noticed that the vorticity is not a scalar field any more since the third component is not zero,

$$\boldsymbol{\omega} = -\frac{\partial u_z}{\partial y}\boldsymbol{e_x} + \frac{\partial u_z}{\partial x}\boldsymbol{e_y} + \left(\frac{\partial u_x}{\partial y} - \frac{\partial u_y}{\partial x}\right)\boldsymbol{e_z}$$

However with $\partial_z = 0$ the vertical component of the vortex stretching is still zero.

Furthermore, the x and y components of the vorticity do not modify the dynamics of u_x and u_y and the flow remains two-dimensional. An additional conserved quantity, compared to pure 2D flow, is the helicity, which can also be decomposed into a vertical part $h_\perp = u_z\omega_z$ and a horizontal part $h_\parallel = u_x\omega_x + u_y\omega_y$. It can be noticed[7] that $\frac{1}{2}\overline{h} = \overline{h_\perp} = \overline{h_\parallel}$ and both parts of the helicity are thus conserved.

2.5.3 Axisymmetric 2D3C flows

Axisymmetric flows were studied early [42, 43], but only for the weaker case of a statistically averaged axisymmetric flow. Recently several studies have been performed for strict (i.e. instantaneous) axisymmetric turbulence [44, 45, 46, 47, 48, 49]. In this geometrical configuration there is an invariance along an angular coordinate. In the (r, θ, z) coordinate system this means that $\partial_\theta = 0$. Examples of axisymmetric geometry are torii and cylinders (Fig 2.7).

From now we introduce the poloidal velocity $\boldsymbol{u_P} = u_r\boldsymbol{e_r} + u_z\boldsymbol{e_z}$ and the toroidal velocity $\boldsymbol{u_T} = u_\theta\boldsymbol{e_\theta}$. With the property $\dfrac{\partial}{\partial\theta} = 0$, equations (2.12)-(2.14) become

$$\begin{cases} \dfrac{\partial u_r}{\partial t} + (\boldsymbol{u_P}\cdot\nabla_P)u_r - \dfrac{u_\theta^2}{r} = -\dfrac{\partial P}{\partial r} + \nu\boldsymbol{\mathcal{L}}u_r + F_r \\ \\ \dfrac{\partial u_\theta}{\partial t} + (\boldsymbol{u_P}\cdot\nabla_P)u_\theta + \dfrac{u_\theta u_r}{r} = \nu\boldsymbol{\mathcal{L}}u_\theta + F_\theta \\ \\ \dfrac{\partial u_z}{\partial t} + (\boldsymbol{u_P}\cdot\nabla_P)u_z = -\dfrac{\partial P}{\partial z} + \nu\Delta_P u_z + F_z \end{cases} \tag{2.75}$$

[7] $$h_\perp = u_z\frac{\partial u_x}{\partial y} - u_z\frac{\partial u_y}{\partial x} \qquad h_\parallel = -u_x\frac{\partial u_z}{\partial y} + u_y\frac{\partial u_z}{\partial x} \Longrightarrow h_\parallel - h_\perp = -\frac{\partial(u_xu_y)}{\partial y} + \frac{\partial(u_zu_y)}{\partial x}$$

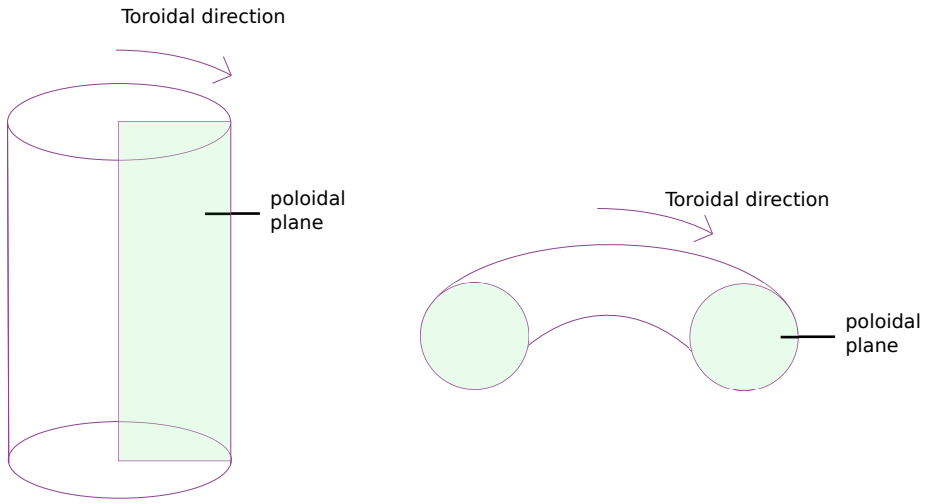

Figure 2.7: Examples of axisymmetric geometries: cylinder and torus. The invariance for our definition of axisymmetric flow is along the toroidal direction.

with

$$\boldsymbol{u_P} \cdot \nabla_P = u_r \frac{\partial}{\partial r} + u_z \frac{\partial}{\partial z}$$
$$\Delta_P = \frac{\partial^2}{\partial r^2} + \frac{1}{r}\frac{\partial}{\partial r} + \frac{\partial^2}{\partial z^2}$$
$$\mathcal{L} = \Delta_P - \frac{1}{r^2}$$

The third velocity component is still only advected by the poloidal flow as in the Cartesian case, but the Coriolis terms $-u_\theta^2/r$ and $u_\theta u_r/r$ induce a coupling of the toroidal velocity and the poloidal dynamics.

The toroidal component can be considered as an active scalar. The 2D3C flow is thereby definitely an intermediate state between 2D and 3D flows, since even if an invariance along the toroidal direction remains, the poloidal flow can be influence by toroidal effects. The total kinetic energy is conserved but its two components can exchange their energy through the influence of the Coriolis terms. However it can be shown by a change of variables [44] that without a toroidal flow the 2D3C flow is equivalent to a Cartesian 2D2C flow.

A stream function can again be defined,

$$u_r = -\frac{\partial \psi}{\partial z} \qquad u_z = \frac{1}{r}\frac{\partial r\psi}{\partial r}, \tag{2.76}$$

with $\mathcal{L}\psi = -\omega_\theta$ and vorticity

$$\boldsymbol{\omega} = -\frac{\partial u_\theta}{\partial z}\boldsymbol{e_r} + \left(\frac{\partial u_r}{\partial z} - \frac{\partial u_z}{\partial r}\right)\boldsymbol{e_\theta} + \frac{1}{r}\frac{\partial r u_\theta}{\partial r}\boldsymbol{e_z}.$$

The toroidal vorticity component ω_θ obeys the equation

$$\frac{\partial \omega_\theta}{\partial t} + (\boldsymbol{u} \cdot \nabla_P)\omega_\theta = \frac{\omega_\theta u_r}{r} + \frac{1}{r}\frac{\partial u_\theta^2}{\partial z} + \nu\mathcal{L}\omega_\theta. \tag{2.77}$$

A new bracket can be introduced:

$$[f,g] = \left(\frac{\partial f}{\partial r} + \frac{f}{r}\right)\frac{\partial g}{\partial z} - \frac{\partial f}{\partial z}\frac{\partial g}{\partial r}. \tag{2.78}$$

The dynamics of the 3D flow can be reduced to a system of two equations from (2.77) by using relations between ψ, ω_θ and $\boldsymbol{u_P}$.

$$\begin{cases} \dfrac{\partial \psi}{\partial t} = \nu\mathcal{L}\psi + \mathcal{L}^{-1}\left([\psi, -\mathcal{L}\psi] - \dfrac{\mathcal{L}\psi}{r}\left(\dfrac{\partial \psi}{\partial z}\right) - \dfrac{1}{r}\dfrac{\partial u_\theta^2}{\partial z}\right) \\ \dfrac{\partial u_\theta}{\partial t} + [\psi, u_\theta] = \nu\mathcal{L}u_\theta + \dfrac{u_\theta}{r}\dfrac{\partial \psi}{\partial z}. \end{cases} \tag{2.79}$$

The details of this kind of flow are studied in Chap. 5 and 6.

2.5.4 Transitions between turbulent states

Whereas the transition from laminar to turbulent flow is a specific research domain with its own approaches, the transition between different turbulent states is less well-defined as a specialty. Nevertheless, over the last 20 years a significant amount of investigations have addressed such transitions. The most well-studied one is probably the transition from 2D to 3D turbulence. Starting from the pioneering study by Lesieur and Frisch [50], several studies have investigated this transition, where the energy cascade flips from inverse to forward, when the flow becomes progressively more three-dimensional.

In particular direct-numerical simulations have investigated this transition in thin fluid layers in periodic domains [51, 52, 53] and experiments have also illustrated this [54]. A recent review article gives a rather exhaustive survey of the literature [55].

Transition from 2D flow to axisymmetric turbulence was only recently studied [49, 56]. It is this kind of transitions which will be at the heart of the present PhD project. Indeed, after introducing numerical tools in the following section, chapter 4 will investigate the properties and specificities of 2D and 2D3C flows. Transitions between these flows will be investigated in Chapters 5, 6 and 7.

3 Numerical tools

In this part we introduce the numerical tools used for the different studies performed during this thesis.

3.1 Direct numerical simulations of turbulence

3.1.1 Choice of a numerical simulation method

In fluid mechanics, a wide range of tools exist, all more or less adapted to the different existing flow-types. Indeed, depending on the fluid type, the compressibility, the geometry or the body forces, different methods can be adopted. In the study of turbulence, even before discussing the numerical method, one needs to define a level of modeling. If every detail of a flow is simulated at every time instant, one speaks of direct numerical simulation. In practice, however, all methods discretize space and time in some way, so that at sufficiently fine scales and times the method only approximates reality. In turbulent flows, as we introduced in Sec. 2.4 the Kolmogorov scale represents the smallest dynamically active scale. If the discretization is sufficiently fine in space and time to resolve these scales and the smallest relevant time-scales, one classifies a simulation as a direct numerical simulation.

However, in three-dimensional high Reynolds number turbulence it is often challenging to resolve the full dynamics, from a numerical point of view. If one only needs the average behavior of a flow, modeling is often introduced. In turbulence, the most general approach to model a flow is the Reynolds Averaged Navier-Stokes (RANS) modeling approach. The RANS method uses the Reynolds decomposition to split physical fields $f(\boldsymbol{x}, t)$ into averaged parts $\overline{f}(\boldsymbol{x})$ and fluctuating part $f'(\boldsymbol{x}, t)$. The RANS equations are derived from the averaged NS equation with $\overline{f'}(\boldsymbol{x}, t) = 0$. The essential difficulty of this method is the closure of the resulting equation through the modeling of a term named Reynolds stress which represents the contribution of the turbulent fluctuations on the mean-field. The complexity of this modeling dictates the speed and the accuracy of the simulation, ranging from models suitable for engineering approaches such as the $k - \epsilon$ model [57] to sophisticated closure approaches such as the EDQNM model [58].

In the last decades, numerical power has increased so rapidly that more and more flows can be simulated using direct numerical simulations, or using hybrid approaches such as large eddy simulation, where a part of the scales of the flow is computed using direct numerical simulation, while the remaining scales are modeled.

If new phenomena are investigated and the detailed behavior of a flow is not known, and sufficient numerical resources are available, it is often, rather than using models, safer to carry out direct numerical simulations. Such simulations can be considered numerical

experiments, if one has sufficient certainty about the governing equations. Eventually the choice of a method is often a compromise between the computational cost and the desired accuracy. For this study we need to understand the behaviour of the turbulence at all scales, particularly energy transfers between different scales. We have no detailed understanding yet, since the system is relatively novel and part of its dynamics unknown. This means that we cannot model it with sufficient certainty, even though first modeling approaches have recently been developed [56]. We therefore use DNS methods.

Once it is decided that we carry out numerical experiments using direct numerical simulations, one needs to think about the numerical implementation of the method. Various formulations are available, depending on the spatial and temporal discretization, modal projection, treatment of boundary conditions and time-stepping.

Two types of methods have been used for this work: the pseudo-spectral approach, a variant of spectral methods, and a spectral element method, a variant of the finite element method, borrowing properties from spectral methods.

3.1.2 Common features

Spectral methods and finite element methods are two ways to implement DNS methods. They share several characteristics.

Discretization Both methods attempt to determine approximate solution of a system of differential equations. For a physical field $u(\boldsymbol{x}, t)$, an approximate solution function $\tilde{u}(\boldsymbol{x}, t)$ can be constructed with a projection on a set of N functions $\phi_i(\boldsymbol{x})$ named trial functions such that:

$$\tilde{u}(\boldsymbol{x}, t) = \sum_{1}^{N} \tilde{u}_i(t)\phi_i(\boldsymbol{x}) \tag{3.1}$$

where $\tilde{u}_i$ is called the expansion coefficient. The trial basis functions do not necessarily satisfy the boundary conditions of the differential equations. We will see later that the choice of the trial functions is the main difference between spectral methods and finite element methods, and that it is the main characteristic of the SEM. The dimension N of the basis determines the resolution of the numerical simulation.

Weighted residuals method Finite element methods and spectral methods are both weighted residuals methods. Indeed since $\tilde{u}$ is only an approximation of u, it cannot be a solution of the differential equation (which admits an unique solution u). If we consider the Navier-Stokes equation on a spatial domain Ω,

$$\frac{\partial \boldsymbol{u}}{\partial t} + \boldsymbol{u} \cdot \nabla \boldsymbol{u} = -\nabla P + \nu \Delta \boldsymbol{u} + \boldsymbol{f}, \tag{3.2}$$

then we can define

$$L(\boldsymbol{u}) = \frac{\partial \boldsymbol{u}}{\partial t} + \boldsymbol{u} \cdot \nabla \boldsymbol{u} + \nabla P - \nu \Delta \boldsymbol{u} - \boldsymbol{f} \tag{3.3}$$

with L containing all the possible spatial and temporal operators applied on $\boldsymbol{u}$ and other fields.

Ideally, $L(\boldsymbol{u}) = 0$, but since $\tilde{u}$ is only an approximation, $L(\tilde{\boldsymbol{u}})$ is not exactly null. The quantity $L(\tilde{\boldsymbol{u}})$ is called the residual and the goal of the numerical method is, using the weighted residuals methods, to find $\tilde{u}$ which minimizes the residual.

The purpose of a weighted residual method is the transformation of the differential equation in a weak formulation by using a test (or weight) function w such that

$$\int_\Omega L(\boldsymbol{u}(\boldsymbol{x},t)w(\boldsymbol{x})\mathrm{d}\Omega = 0. \tag{3.4}$$

This expression is also called the variational form, which means that we have to minimize the quantity $\int_\Omega L(\tilde{\boldsymbol{u}}(\boldsymbol{x},t))w(\boldsymbol{x})\mathrm{d}\Omega$. In practice the residual is projected on basis functions w_i such that $\forall i, \int_\Omega L(\tilde{\boldsymbol{u}}(\boldsymbol{x},t))w_i(\boldsymbol{x})\mathrm{d}\Omega$ must be minimal.

3.2 Pseudo-spectral method

3.2.1 Spectral methods

Spectral methods are characterized by the decomposition of the solution function on a basis of high-order polynomials or Fourier series. It is a global decomposition, which means that the polynomials are non-trivial and regular on the whole domain.

There are different types of spectral methods such as Tau, Galerkin and collocation methods. The last one is sometimes called pseudo-spectral method in fluid mechanics, but for the present study the name pseudo-spectral method will be designated to indicate another technique which will be described later.

We will concentrate on Galerkin methods which allows the orthogonality of the projection. It also means that the trial functions must satisfy boundaries condition, which is the main difference with the Tau approach. At the end a system must be solved to obtain the expansion coefficients $\tilde{u}_i(t)$.

3.2.2 Decomposition on a Fourier basis using the Galerkin method

A convenient decomposition uses a Fourier basis of trial functions ϕ_k defined by $\phi_k(x) = e^{i\boldsymbol{k}\boldsymbol{x}}$. The drawback is that the domain must be chosen so that the basis satisfies the boundary conditions. For a 2D geometry a domain $[0:2\pi]\times[0:2\pi]$ with the base $(\boldsymbol{e_r},\boldsymbol{e_z})$ will be chosen in the present work. A stream function ψ and azimuthal velocity u_θ can be approximated by $\tilde{\psi}$ and $\tilde{u_\theta}$. These approximation functions can be expanded on the truncated Fourier basis as follows,

$$\tilde{\psi}(t,\boldsymbol{x}) = \sum_k \hat{\psi}_k(t)e^{i\boldsymbol{k}.\boldsymbol{x}} \qquad\qquad \tilde{u_\theta}(t,\boldsymbol{x}) = \sum_k \hat{u}_{\theta k}(t)e^{i\boldsymbol{k}.\boldsymbol{x}},$$

with $\boldsymbol{k} = k_r\boldsymbol{a_r} + k_z\boldsymbol{a_z}$ in Fourier space.

3.2.3 Solving differential equation using pseudo-spectral methods

Once the equations are projected on the Fourier basis, one can write equations for the Fourier coefficients. For the 2D3C equations this yields, for instance,

$$\frac{\partial\hat{u}_\theta}{\partial t} = \nu\hat{\boldsymbol{\mathcal{L}}}\hat{u}_\theta + \widehat{\frac{u_\theta}{R}\frac{\partial\psi}{\partial z}} - \widehat{[\psi,u_\theta]} \tag{3.5}$$

and

$$\frac{\partial\hat{\psi}}{\partial t} = \nu\hat{\mathcal{L}}\hat{\psi} + \hat{\mathcal{L}}^{-1}\left[\widehat{[\psi, -\mathcal{L}\psi]} - \widehat{\frac{1}{R}\frac{\partial u_\theta^2}{\partial z}} - \widehat{\frac{\mathcal{L}\psi}{R}\frac{\partial\psi}{\partial z}}\right]. \tag{3.6}$$

In these equations all terms containing products of fields become convolutions between the Fourier transforms,

$$\widehat{\frac{\mathcal{L}\psi}{R}\frac{\partial\psi}{\partial z}} = \widehat{\frac{\mathcal{L}\psi}{R}} * \widehat{\frac{\partial\psi}{\partial z}} \tag{3.7}$$

where the convolution product is indicated by $*$. The computation of such a convolution requires N^2 operations, which will make simulations prohibitively expensive when thousands or even millions of modes are used, as needed to represent fully developed turbulence.

At this moment intervenes the pseudo-spectral method. Instead of staying in the Fourier (spectral) space, non-linear terms are computed in physical space. For that purpose discrete Fourier transforms are used. More importantly the development of Fast Fourier Transform algorithms has made this procedure very competitive for large numbers of modes, where purely spectral methods become practically impossible to use.

Let us define vectors $\boldsymbol{x}_{mn} = r_m\boldsymbol{e_r} + z_n\boldsymbol{e_z}$ such that

$$r_m = \frac{2\pi m}{N} \qquad z_n = \frac{2\pi n}{N} \qquad (m,n) \in [-N/2, N/2-1] \tag{3.8}$$

Then the discrete Fourier coefficient $\tilde{\psi}_k$ is defined by

$$\tilde{\psi}_{\boldsymbol{k}}(t) = \frac{1}{N^2}\sum_{m,n}\psi(\boldsymbol{x}_{mn},t)e^{-i\boldsymbol{k}\cdot\boldsymbol{x_{mn}}} \qquad \text{with} \qquad \psi(\boldsymbol{x}_{mn},t) = \sum_{k_r,k_z}\tilde{\psi}_{\boldsymbol{k}}(t)e^{i\boldsymbol{k}\cdot\boldsymbol{x_{mn}}} \tag{3.9}$$

For instance, in Eq. 3.7, $\widehat{\mathcal{L}\psi/R} = \hat{\mathcal{L}}\hat{\psi}/R$ and $\widehat{\partial_z(\partial\psi)}$ can be conveniently computed in Fourier space. Inverse transforms are used to get $\mathcal{L}\psi/R$ and $\partial\psi/\partial z$. Conversely, the product is computed in physical space to avoid the need for a convolution product. Finally discrete Fourier coefficients $\widetilde{\mathcal{L}\psi R^{-1}\partial_z\psi}\Big|_k$ are computed by the discrete Fourier transform.

This, pseudo-spectral method is less expensive ($N\log(N)$ operations instead of N^2). However, it introduces an aliasing effect. Indeed

$$\widetilde{\frac{\mathcal{L}\psi}{R}\frac{\partial\psi}{\partial z}}\bigg|_k = \widehat{\frac{\mathcal{L}\psi}{R}\frac{\partial\psi}{\partial z}}\bigg|_k + A_N(u) \tag{3.10}$$

Where the aliasing contribution $A_N(u)$ is resulting from the product term. A method must be applied to avoid errors in the simulations. The most radical (but not necessarily most optimized) method is to cut-off the Fourier modes generated by the product. This so-called two-thirds approach is the one used in the present study.

It can be noticed that the use of the discrete Fourier expansion for the pseudospectral method leads to a discretization of the NS equation very similar to the expression obtained with the collocation method (vectors of discretization $\boldsymbol{x}_{mn}$ can be seen as collocation vectors. For this reason the collocation method is often called pseudo-spectral method when the solution is approximated by a Fourier-series.

3.2.4 GHOST code

GHOST (for Geophysical High-Order Suite for Turbulence [59]) is a pseudo-spectral method code (in the meaning of collocation method) mostly written in Fortran90 and C. It can solve equations in 2D and 3D for different physical issues like compressible flows, MHD flows, plasmas, passive scalar... It uses a a hybrid parallelization method combining MPI and OpenMP for the 3D version of the code, but for our 2D case it will be only a MPI parallelization. Fourier transformations use the FFTW library. Visualizations have been performed with Python scripts.

Time is discretized using a 2nd-order explicit Runge-Kutta scheme. As discussed in the previous section, aliasing must be removed. GHOST uses the 2/3 de-aliasing: all modes above a maximum value $k_{max} = N/3$ ($N/3 = 2/3 \times N/2$) are set to zero in the Runge-kutta algorithm, which means that

$$\forall k > k_{max} \qquad \hat{\psi}_k(t) = 0 \qquad \hat{u}_{\theta k}(t) = 0 \tag{3.11}$$

For this reason, for a Nth-order Fourier expansion, Fourier spectra will be limited by k_{max}.

Routines for 2D geometry with passive scalar were already implemented in GHOST. It solves stream function and scalar equations. Global quantities are directly computed in Fourier space. For the study of the axisymmetric case, the GHOST routines have been modified by adding coupling terms from the Coriolis effect in the Runge Kutta routine.

Furthermore, for both the 2D3C and axisymmetric cases (Chaps. 4 and 5), the diffusion-convection equation is turned into an equation for the third velocity component. It has been verified that results in "flat" space can be obtained by pushing the curvature radius $R \longrightarrow \infty$.

3.2.5 The inhouse LMFA code

Chronologically, the results in the last Chapter of this thesis, Chap. 7, were obtained first. That study could have been carried out with GHOST. However, we used the three-dimensional pseudo-spectral code of the Turbulence and Instability team [60] to carry out that study. We will not give the details, since the priniciple characteristics are common with GHOST. The main differences are that not the equation for the stream-function is used, but the equations for the three velocity components are directily discretized.

3.3 Spectral element methods

3.3.1 Finite element method

The finite element method differs from the pseudo-spectral method by the fact that it is a local method. It means that for a solution function of an equation, the goal of this method is not to obtain the global approximation of the function like for the pseudo spectral method, but rather to get an approximated solution function at several points of the domain. The method needs the creation of a mesh on the domain with different subdomains named finite elements. At each node of this mesh, the solution function can be obtained and then interpolated on the element.

The particularity of the finite element approach is that trial functions f_i are non-trivial only on a subdomain Ω_i of the global domain. In contrary, for the pseudo-spectral method the decomposition uses non-trivial function on the whole domain. It explains the better adaptability of finite elements to account for complex geometry. Usually for the finite element methods, trial functions are piecewise low-order polynomials. Each subdomain is called "element". If N is the number of elements in the domain then the approximated solution $\tilde{u}$ is defined on each element i by $\tilde{u}_i$:

$$\tilde{u} = \sum_{1}^{N} \tilde{u}_i f_i \tag{3.12}$$

The simulation resolution is $N^d E$ with N degree of basis polynomials, d the geometry dimension (in our case $d = 2$) and E is the number of elements.

3.3.2 Nek5000 code: a spectral element code

The purpose of spectral element methods [61] is to combine the advantages of both spectral methods and finite elements. In this method, weight functions used for the interpolation of the solution are higher-order polynomials with global continuity (for instance Chebyshev polynomials in the original formulation [61]). This allows a better approximation of the function over the element compared to interpolations based on low order piece-wise polynomial basis function, since resolution increases quadratic in 2D geometry. This higher complexity of basis functions imposes more simple shapes for the elements of the mesh, rectangular or hexahedral.

Finite element methods are easier to implement, more particularly for complex geometry and need less calculation time for the integration, whereas spectral element methods are more accurate more particularly for fast variations which can be generated by turbulence in fluids. Spectral elements appear to be a good compromise between the accuracy of pseudo-spectral methods and the geometrical flexibility of finite element methods.

Nek5000 [62] is an open-source spectral element code developped in 1990 from Nekton 2.0 code and written in Fortran77 and C. It uses MPI for parallelization. Visualizations of the flow have been made with ViSit [63]. NEK allows to compute a wide range of fluid flows: compressible flows, heat transfer, MHD, combustion, particle dispersion, moving walls...

By default in 2D geometry Nek5000 solves the Navier-Stokes equations for both velocity components, and a scalar advection diffusion equation. The file .usr allows the addition of external forces. It was used to add Coriolis terms as external forces. As with GHOST it results in transforming the heat equation into an equation for the third velocity component. Additional advection-diffusion equations can be added for the study of mixing.

As a high order spectral element code it uses high order polynomials as basis functions. Trial basis functions are Lagrange interpolating polynomials L_i. Interpolating nodes are Gauss-Lobato-Legendre nodes, more particularly in our multidimensional case tensor-product polynomials.

The PnPn-2 method is used, meaning that that if a nth-order trial polynomial basis is chosen for the decomposition of velocity, the pressure is projected on a polynomial basis of order $n-2$. Moreover the trial basis functions for the decomposition of the pressure are

Lagrange polynomials interpolating Gauss-Legendre nodes. Time discretization uses the kth order Backward Difference Formula (BDFk). For the pressure equation the method is an extrapolation of order k (EXTk).

The dealiasing approach is a kind of two-third truncation rule, slightly different from that used by GHOST. Instead of an Nth-order expansion, the terms to which an inverse discrete Fourier transform must be applied to calculate the convolution product are expanded in a $3N/2$ discrete Fourier series. However expansion coefficients above $N/2$ are set to zero.

3.4 Summary of methods used

In the remainder of this thesis, three different numerical codes are used.

- In the next 2 chapters, Chaps. 4 and 5 two-dimensional pseudo-spectral simulations are carried out on a double-periodic domain, using GHOST.
- Then, in Chap. 6, since non-trivial (toroidal) geometry is considered with no-slip boundary conditions, the spectral element code NEK5000 is used.
- In the last part, where again, periodic boundary conditions are used, this time in three-dimensional flow, we use the house-code of the LMFA.

4 Cartesian Two-dimensional three-component turbulence

In this chapter[1] we focus on two-dimensional flow with two or three velocity components. We consider the Cartesian case, where the third component is perpendicular to the plane of the 2D flow. There is no curvature involved. We first focus on Galerkin truncated systems of 2D and 2D3C flows. In the 2D2C flows we encounter a surprising discrepancy between theory and observations, which we attempt to explain.

Subsequently it is illustrated that in 2D3C flows the helicity plays an important role in the determination of the statistical equilibrium, suggesting that it might also importantly affect the dynamics. This is illustrated in the last part of this chapter where the role of helicity in 2D3C flows and 2D mixing of a passive scalar is explored.

4.1 Equilibrium statistical mechanics

An impressive feature of two-dimensional turbulence is its tendency to self-organize, forming large scale structures. Some examples were given in the previous chapter. An understanding of this tendency was given by Onsager in 1949 [64], who suggested to apply statistical mechanics to a point-vortex system. Such a structure-based statistical mechanics was further explored by Joyce and Montgomery [65, 66] and more recently by the works of Miller [67], Robert and Sommeria [68]. A concise review can be found in the article of Eyink and Sreenivasan [69], and more comprehensive reviews are [70] and [71].

The point-vortex and coarse grained vorticity statistical mechanics are approaches based on the observation that enstrophy, and small vorticity patches in general, are advected conservatively in the two-dimensional Euler equations. An alternative statistical approach in turbulence consists in considering, instead of vorticity patches in physical space, the dynamics of modes, after a convenient decomposition. The most common decomposition in turbulence research is the Fourier-decomposition, as discussed in Sec. 2.4. Once a flow-field is decomposed on a large, but finite number of modes, the statistically most probable state can be determined by statistical mechanics, once physical constraints, such as energy conservation, are taken into account.

For three dimensional Euler-turbulence, statistical mechanics on a truncated set of Fourier-modes yields, if the only constraint of the system is energy conservation, an equipartition of energy between all the modes. This means that, statistically, every Fourier mode contains the same amount of energy. This results was first obtained by Lee in 1951 [72]. The definition of the kinetic energy spectrum (see Sec. 2.4) yields then

[1] For this chapter we acknowledge a collaboration with Tong Wu and Xi-Yuan (Bruce) Yin.

that

$$E_{3D}(k) = \frac{8\pi k^2}{\alpha}, \tag{4.1}$$

with α a constant. The subscript $3D$ will be used only when the dynamics are three-dimensional and the subscripts will be omitted for 2D and 2D3C cases, which are the main subject of this chapter. Kraichnan modified this statistical mechanics after the discovery of another constraint on 3D Euler-turbulence: helicity conservation, leading to,

$$E_{3D}(k) = \frac{8\pi\alpha k^2}{\alpha^2 - \beta^2 k^2}. \tag{4.2}$$

From this expression, which modifies only the largest wavenumber behavior of the equilibrium, Kraichnan inferred that helicity should not tremendously influence the dynamics of three-dimensional flow. This assumption turned out to be valid in most non-pathological cases (see however some extreme cases [73] with very strong imposed helicity, or turbulence where vortex-stretching has been removed artificially [74]).

After this short digression on three-dimensional turbulence, let us come back to two-dimensional three-component turbulence, the main subject of this chapter. Since the third velocity component is passively advected by the 2D2C flow, it is of interest to discuss the pure two-dimensional flow first. In his seminal paper on two-dimensional turbulence, Kraichnan [7] not only carried out the statistical mechanics of two-dimensional turbulence, but he also inferred from the results that two-dimensional flows should show a tendency to transfer the two conserved quantities (energy and enstrophy) in opposite directions. From the statistical mechanics prediction of the kinetic energy spectrum,

$$E(k) = \frac{2\pi k}{\alpha + \beta k^2}, \tag{4.3}$$

he inferred that, to approach this equilibrium, enstrophy should be dominantly transferred to large k, while energy should then "cascade" in the inverse direction. This double-cascade picture of two-dimensional turbulence has since this investigation been the cornerstone of the description of two-dimensional turbulence. This illustrates the importance of statistical mechanics applied to turbulent flows.

The prediction (4.3) was verified in early simulations of the two-dimensional Euler equations. Indeed, the development of pseudo-spectral methods in the 1970s allowed to solve non-dissipative simulations of truncated Euler dynamics. It was shown by [75, 76] that the theory of Kraichnan roughly predicts the correct energy spectrum (4.3) of the equilibrium state. It was however observed that "*substantial deviations from equilibrium are present at low wavenumbers. These are probably explained by the long dynamical time scale of large scale turbulent eddies, so that continuing the calculation to much longer times may give relaxation*"[75]. However more recent numerical investigations showed that these deviations persist even at very long times, and no hint of relaxation is observed [77, 78]. In particular, when the ratio of energy to enstrophy is large, some discrepancy is observed in the larger Fourier modes. We will come back to this in Sec. 4.2.4.

The third velocity component u_z, which is advected as a passive scalar allows also a description by statistical mechanics. The outcome is that the variance (or vertical energy) is, as in 3D turbulence without helicity, equally distributed over all available Fourier modes. There is however an additional invariant in the system, which is the vertical helicity, determined by the integral correlation of vertical vorticity and velocity.

This second invariant modifies the equilibrium distribution but has, in the context of two-dimensional turbulence, received only very little attention. Only in references [79, 80, 81] interest was paid to the influence of the vorticity-scalar correlation on two-dimensional scalar mixing. We will assess the statistical mechanics of this quantity in 4.3.

Then to conclude this chapter, we will investigate how this invariant influences the mixing of a passive scalar in two-dimensional Navier-Stokes turbulence in 4.4, when viscosity and diffusion are present in the system.

4.2 Equilibrium statistical mechanics for two-dimensional turbulence

In this section we consider the case of two-dimensional Euler turbulence, restricted to a finite number of Fourier modes. The dynamics of this system are given by

$$\frac{\partial \boldsymbol{u}}{\partial t} + \boldsymbol{u} \cdot \nabla \boldsymbol{u} = -\nabla P \tag{4.4}$$

with $\nabla \cdot \boldsymbol{u} = 0$. The velocity is $\boldsymbol{u}(x, y, t)$ and the gradient acts in the plane $\nabla = (\partial_x, \partial_y)$. After projecting on a Fourier base, only modes restricted to the interval $k \in [k_{\min}, k_{\max}]$ are retained. Eq. (4.4) does not contain any forcing or friction and conserves thereby energy,

$$E = \int \frac{1}{2} |\boldsymbol{u}|^2(\boldsymbol{x}) \, \mathrm{d}\boldsymbol{x}. \tag{4.5}$$

Furthermore, as discussed in Chap. 2, enstrophy

$$W = \int \omega^2(\boldsymbol{x}) \mathrm{d}\boldsymbol{x} \tag{4.6}$$

is another invariant of the system. In these expressions $\boldsymbol{\omega} = \nabla \times \boldsymbol{u} = \omega \boldsymbol{e}_z$. The integral balance is thus

$$\frac{dE}{dt} = \frac{dW}{dt} = 0. \tag{4.7}$$

4.2.1 Predictions

In the appendix of this thesis we illustrate how equilibrium energy spectra can be obtained. For the energy spectrum of two-dimensional turbulence the prediction is (as mentioned in the introduction of this chapter),

$$E(k) = \frac{2\pi k}{\alpha + \beta k^2} \tag{4.8}$$

Once the initial values of the kinetic energy and the enstrophy are fixed, for a given wave number interval, α and β are fixed. This allows us to determine predictions for other integral quantities, such as the palinstrophy and the mean-square stream-function. Indeed, these quantities are not invariant, but since their values are determined by the energy spectrum, they should tend to a constant value if the energy spectrum tends to its equilibrium shape.

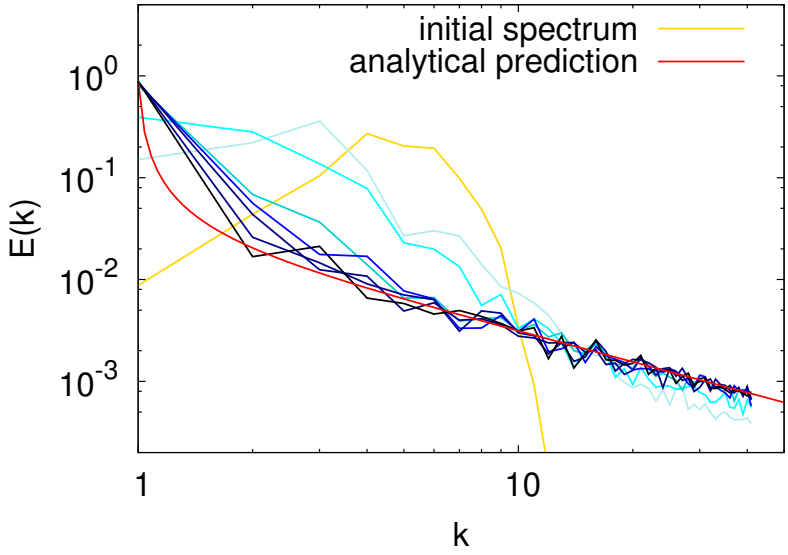

Figure 4.1: Time evolution of the energy spectrum for $W/E = 28.4$ at t=0, 6, 10, 40, 100, 200, 300 and 500. The analytical prediction is also shown.

For instance, palinstrophy B is defined as

$$B = \int |\nabla \times \boldsymbol{\omega}|^2 \, \mathrm{d}\boldsymbol{x} = \int |\nabla \times \nabla \times \boldsymbol{u}|^2 \, \mathrm{d}\boldsymbol{x} \tag{4.9}$$

and since the flow is incompressible, $\nabla \cdot \boldsymbol{u} = 0$ and :

$$B = \int |-\Delta \boldsymbol{u}|^2 \, \mathrm{d}\boldsymbol{x} \tag{4.10}$$

and by using 4.3 we have

$$\begin{aligned} B &= \int_{k_{min}}^{k_{max}} k^4 E(k) \, \mathrm{d}k \\ &= \int_{k_{min}}^{k_{max}} \frac{2\pi k^5}{\alpha + \beta k^2} \, \mathrm{d}k \\ &= 2\pi \left[\frac{\alpha^2}{2\beta^3} \ln \left(\frac{\alpha + \beta k_{max}^2}{\alpha + \beta} \right) - \frac{\alpha(k_{max}^2 - 1)}{2\beta^2} + \frac{k_{max}^4 - 1}{4\beta} \right] \end{aligned} \tag{4.11}$$

For the mean-square stream-function $\int \psi^2 \mathrm{d}\boldsymbol{x}$, a similar expression can be derived, since its value is determined by the integral of $k^{-2}E(k)$.

4.2.2 Numerical results at low resolution

Numerical simulations are performed with the parallel pseudospectral code GHOST [59] (see Chap. 3). Equations for stream function are solved in a 2π-periodic square box with a resolution $N = 128^2$ for this first part of the investigation. The 2/3 method has been used, therefore the cut-off of the spectra is $k_{max} = 42$. The initial condition is given by the Gaussian spectrum

$$E(k) = C_k e^{-(k-k_0)^2/2\sigma^2} \tag{4.12}$$

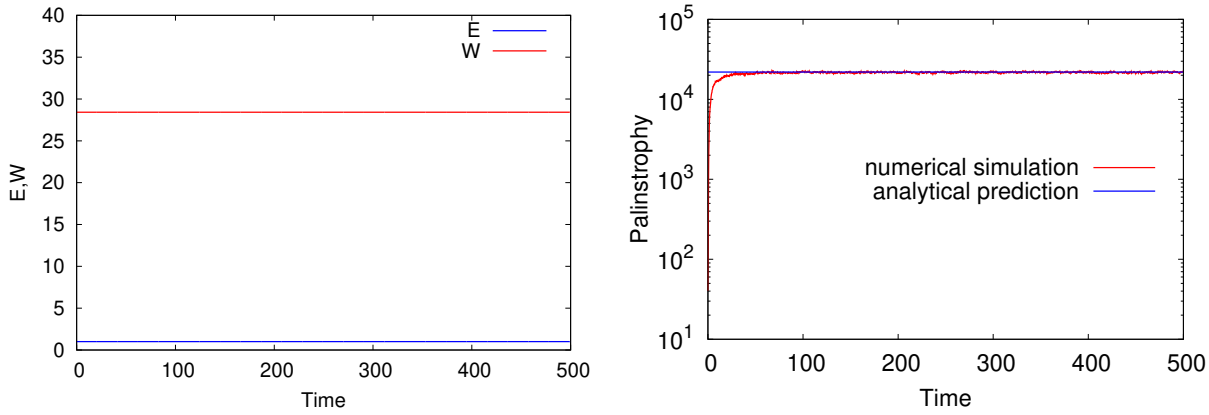

(a) (b)

Figure 4.2: Time evolution of (a) inviscid integral invariants, energy and enstrophy, (b) palinstrophy. The final value of the latter fits correctly with the predicted value.

with $k_0 = 4$, $\sigma = 2$ and C_k is a chosen so that $\int_1^{k_{max}} E(k)\ \mathrm{d}k \equiv E = 1$, where all Fourier-phases are chosen randomly so that the initial conditions is structureless.

In Fig. 4.1 we show the evolution of the kinetic energy spectrum for a given initial condition towards its equilibrium shape. It is observed that the long-time shape of the spectrum is close to the prediction. An interesting feature is that at the energy spectrum rapidly evolves for $k \approx 1$ even though in principle these scales have the slowest dynamics. This might be related to the ideas of Fox and Davidson [78], who suggested that in 2D Euler turbulence the transients should be governed by integral constraints which determine the wave number dependence for k going to zero.

To conclude, at these resolutions, we observe that the energy distributions tend to the equilibrium spectra predicted using statistical mechanics. This is a rather well known result. How this agreement deteriorates for large wavenumber domains is less well-known and will be discussed now.

4.2.3 Numerical results at large resolution

We use the same numerical setup but with a higher resolution 512^2. The initial energy spectrum is still given by the Gaussian function Eq. (4.12), but different mean wave numbers k_0 are chosen. This corresponds, on the level of the invariants to a modification of the ratio W/E of the flow.

To relate this latter ratio to a physical quantity, we introduce the characteristic wavelength

$$k_c = \sqrt{W/E}. \tag{4.13}$$

The energy is maintained at the same value, here $E = 1$, for all simulations. We modify therefore k_c by changing W.

Figure 4.3 shows that the shape of the final kinetic energy spectrum is, as expected, dependent on the ratio W/E. Indeed, modifying this ratio changes the ratio of related Lagrangian multipliers α/β. For small values of α/β, $E(k)$ has an asymptotic dependence $2\pi/\beta k$ at small scales. On the contrary if α/β is large, the asymptotic prediction for the energy spectrum is $E(k) \approx 2\pi k/\alpha$ at large scales.

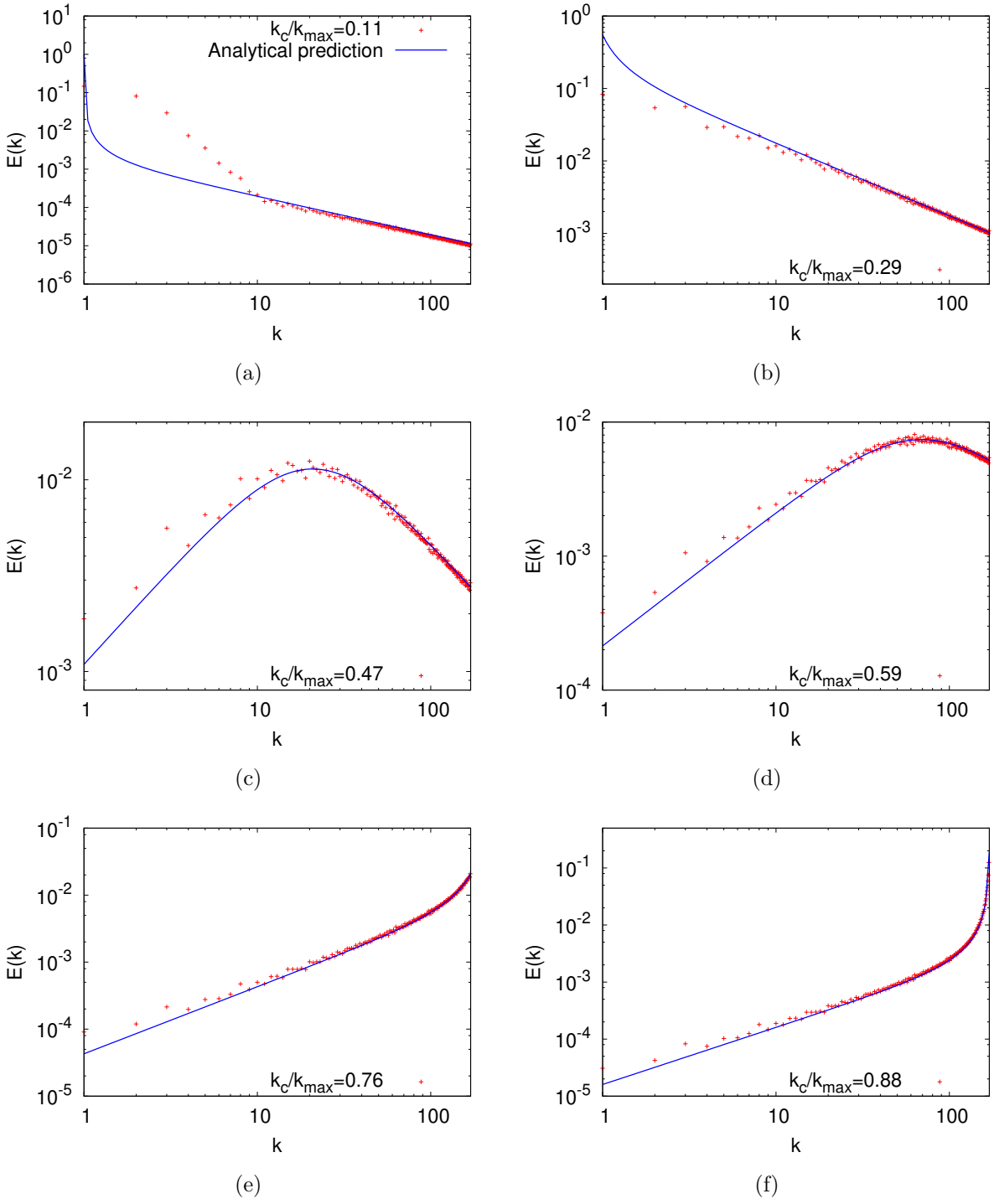

Figure 4.3: Equilibrium energy spectrum for different values of k_c/k_{max} for Gaussian initial distribution.

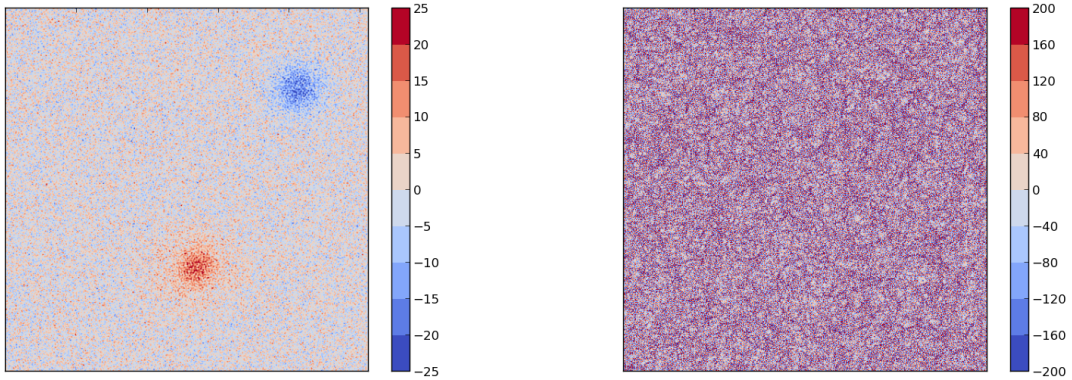

(a) (b)

Figure 4.4: Vorticity field for $k \in [1:170]$, and (a) $k_c/k_{max} = 0.11$, (b) $k_c/k_{max} = 0.88$.

An interesting result is the deviation to the theory for small wave numbers. This deviation is stronger for small k_c/k_{max} (i.e. small initial mean wavenumber k_0), particularly for $k_c/k_{max} = 0.11$. For other cases there is less energy in small wave numbers relatively to the total kinetic energy, so the deviation is not important for large initial k_c/k_{max}. This deviation was observed in the past [75, 78, 77], as mentioned in the introduction, but no satisfactory explanation is known. In Fig. 4.4, we show a visualization of the vorticity field, corresponding to the flow with the largest deviation from theory, $(k_c/k_{max}) = 0.11$. It is observed that, apart from noise, a large-scale condensate is observed.

4.2.4 Coexistence of noise and structures

The presence of a condensate hints on the presence of phase-correlations. This suggests that the different Fourier-modes are not statistically independent, which might violate the assumption of ergodicity with respect to the statistics of the Fourier modes. Indeed, this assumption is behind the derivation of the equilibrium energy spectra. We have at this point no rigorous explanation, but, nevertheless, we have a suggestive description of the phenomenology. Indeed, as we discussed in the introduction, the work of Onsager, followed by Joyce, Montgomery, Miller, Roberts and Sommeria, proposed a different type of statistical mechanics, not based on Fourier modes, but describing the dynamics of point-vortices, or, in the later works, by coarse-grained vorticity. An outcome of these statistical mechanics approaches was the derivation, in equilibrium, of a function relation between vorticity and stream-function,

$$\omega = F(\psi), \tag{4.14}$$

indeed, if for every point in the flow such a relation exists, the nonlinearity vanishes, so that one obtains a steady solution of the Euler equation. In Fig. 4.5, we show a scatter-plot of ψ versus ω for a given time-instant. Clearly, the noisy cloud of points does not fall on a single functional relation. Nevertheless, if the scatterplots are averaged in time for many realizations, a clear functional relation, not very different from a hyperbolic sine

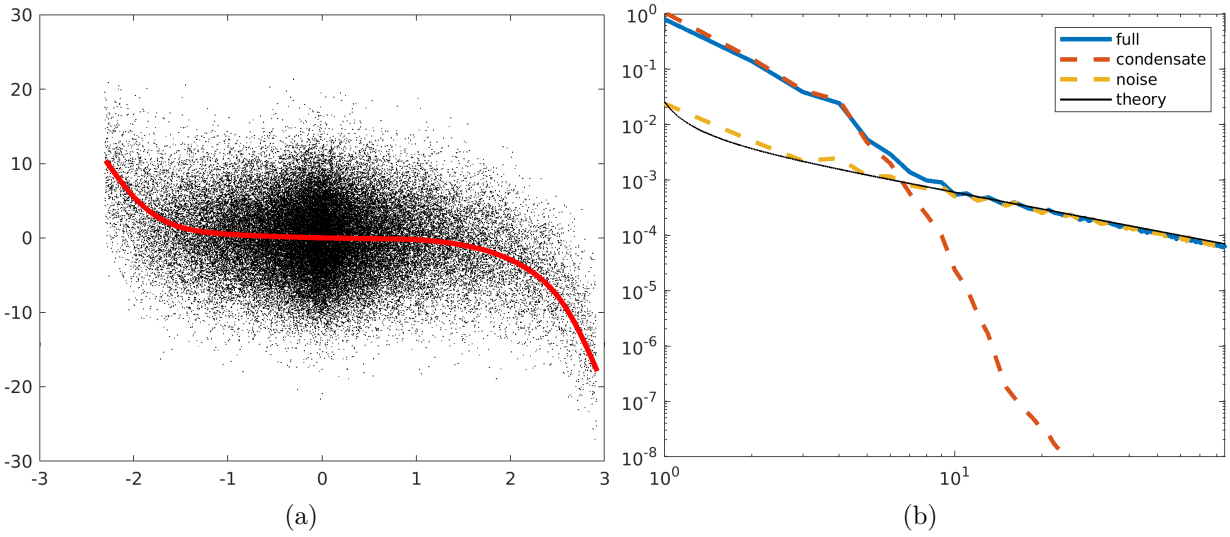

(a) (b)

Figure 4.5: (a) Scatter-plot of the vorticity against the stream-function for a given time-instant. Every dot corresponds to a point (x, y) of the flow-field, where both the vorticity and the stream-function are evaluated. The thick red line is a temporal average over many scatter-plots, averaging all possible vorticity values for small bins of the stream-function. (b) Decomposition of the energy spectrum $E(k)$ into a condensate part and a noise part. The noise part is closely described by the theoretical prediction.

is observed. We call this function $\overline{F}$, and we assume that this function characterizes the condensate.

We now compute, for a given time t for every point in space an estimate for the vorticity of the condensate

$$\overline{\omega}(x, y, t) = \overline{F}[\psi(x, y, t)] \tag{4.15}$$

Subtracting now this "coherent" vorticity from the total vorticity,

$$\omega'(x, y, t) = \omega(x, y, t) - \overline{\omega}(x, y, t), \tag{4.16}$$

we should get an estimate for the remaining noise. We illustrate in Fig. 4.6, that this decomposition, at least visually, allows to clearly separate the condensate from the underlying noise.

An interesting feature is now that, if we compute the energy and the enstrophy of the noise-part of the flow and compute the associated Kraichnan spectrum, the analytical prediction very closely predicts the simulated results (Fig. 4.5)(b).

The interesting feature of our approach is that we do not assume any particular shape of the condensate or any particular coloring of the noise. The only assumption is that there exists a function $\overline{\psi} = F(\overline{\omega})$, which characterizes the condensate, without any other constraints on the type of function.

We can conclude this section by saying that even though we have no rigorous results explaining the shape of the spectrum, we show that we can understand the dynamics as a coexistence of a condensate and noise, where the condensate is described by "point-vortex" statistical mechanics, whereas the noise satisfies an energy distribution, consistent with equilibrium statistical mechanics applied to Fourier modes.

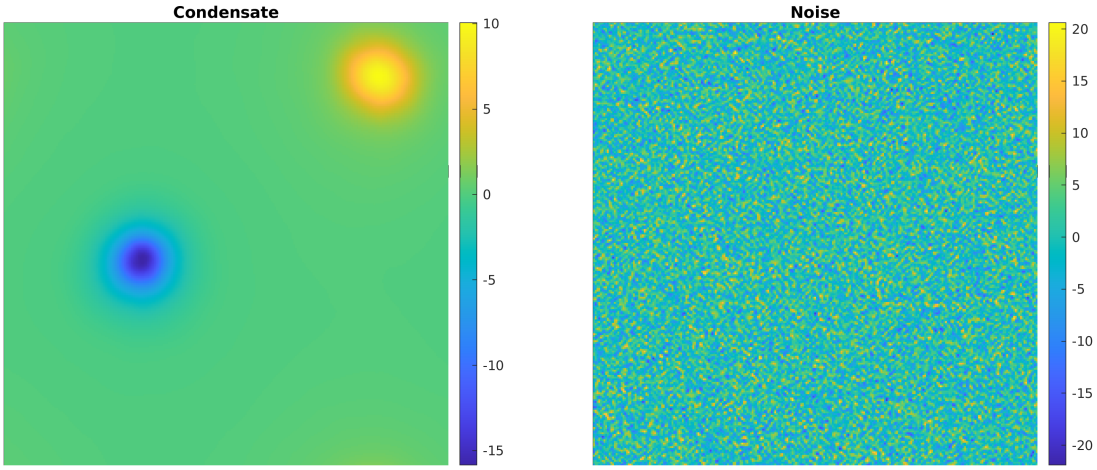

Figure 4.6: Decomposition of the flow-field into a condensate and the underlying noise

4.3 Equilibria for 2D3C flows: the influence of helicity

Now that we have explored the parameter-space for two-dimensional two-component flow, let us add the third component. We propose to investigate a statistically homogeneous and isotropic incompressible turbulent flow with a three component velocity field, invariant along the z–direction and without curvature. This means that the third component u_z is always perpendicular to the plane formed by the other two components (x, y). The velocity $\boldsymbol{u} = \boldsymbol{u}_z + \boldsymbol{u}_\perp$ is divided in two components, the part aligned with the z-direction $\boldsymbol{u}_z$, and the velocity in the (x, y) plane, perpendicular to the z–axis. The specificity compared to everyday 3D turbulence is that we have $\partial_z = 0$ for all components of the flow.

The equations we consider are then

$$\frac{\partial \boldsymbol{u}_\perp}{\partial t} + \boldsymbol{u}_\perp \cdot \nabla \boldsymbol{u}_\perp = -\nabla P \tag{4.17}$$

$$\frac{\partial u_z}{\partial t} + \boldsymbol{u}_\perp \cdot \nabla u_z = 0 \tag{4.18}$$

with $\nabla = (\partial_x, \partial_y)$ and $\nabla \cdot \boldsymbol{u}_\perp = 0$. It can thus be seen in Eq. (4.17), that the planar velocity is only advected by itself and independent from the vertical velocity: it is fully two dimensional and is identical to the system in the first part of this chapter. The vertical velocity equation is governed by an advection-equation and can be considered as a passive scalar.

The individual dynamics of Eq. (4.17) has been considered in the foregoing. In the present section we will therefore focus on the dynamics and statistics of $u_z(x, y, t)$. The first questions is then: what are the invariants associated with Eq. (4.18)? The first, perhaps most obvious, conserved quantity is the variance of u_z, indeed, as mentioned in Sec. 2.3.3, the variance of a passive scalar,

$$S = \int_{\mathbb{R}^3} u_z^2 \, \mathrm{d}V, \tag{4.19}$$

is an inviscid invariant. There is however another invariant which can play a role in the dynamics of u_z, which is associated with the planar velocity. This invariant is the helicity, which we already introduced in Sec. 2.3.4.

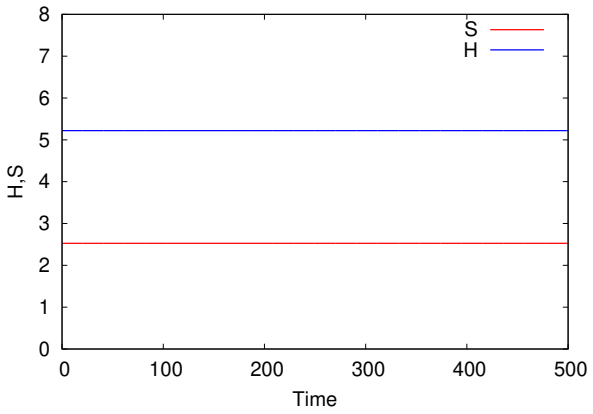

(a)

Figure 4.7: Time evolution of the invariants S and H.

In the present set-up, helicity can be divided in two parts, $H_\perp$ and $H_\parallel$,

$$H_\perp = \int_{\mathbb{R}^3} \boldsymbol{u}_\perp \cdot \boldsymbol{\omega}_\perp \, \mathrm{d}\boldsymbol{x} = \int \left(-\frac{\partial u_z}{\partial y} u_x + \frac{\partial u_z}{\partial x} u_y \right) \mathrm{d}\boldsymbol{x} \tag{4.20}$$

$$H_z = \int_{\mathbb{R}^3} u_z \omega_z \, \mathrm{d}\boldsymbol{x} = \int u_z \left(\frac{\partial u_x}{\partial y} - \frac{\partial u_y}{\partial x} \right) \mathrm{d}\boldsymbol{x}. \tag{4.21}$$

How helical a flow is can be quantified using the relative helicity H_{rel}

$$H_{rel} = \frac{H}{\sqrt{S W_\perp}} \tag{4.22}$$

with

$$W_\perp = \int_{\mathbb{R}^3} \omega_z^2(\boldsymbol{x}) \mathrm{d}\boldsymbol{x}, \tag{4.23}$$

representing the vertical enstrophy, related to the horizontal velocity field $u_\perp$ so that $\nabla \times \boldsymbol{u}_\perp = \boldsymbol{e}_z \omega_z$.

We recall that the other invariants of 2D3C flows are the horizontal energy E, and related enstrophy $W_\perp$. Since for a 2D3C flow $H_\parallel = H_\perp = \frac{1}{2}H$, the total number of independent invariants is therefore 4. Time evolution of the vertical energy and the helicity are shown in figure 4.7 for $H_{rel} = 0.61$. Vertical energy and helicity are conserved during the simulation, as expected.

In the appendix, it is shown how to derive equilibrium spectra for two-dimensional Euler and 2D3C flows. The energy spectrum associated with the planar dynamics remains unchanged,

$$E(k) = \frac{2\pi k}{\alpha + \beta' k^2} \tag{4.24}$$

and the enstrophy spectrum is obtained from the relation $W(k) = k^2 E(k)$. The novel quantities, associated with the vertical velocity are

$$S(k) = \frac{2\pi k}{\gamma} \frac{\alpha + \beta k^2}{\alpha + \beta' k^2}. \tag{4.25}$$

With $\beta' = \beta - \delta^2/\gamma$.

Obviously, since the 2D dynamics are independent on the presence or absence of the passive scalar, β' should have the same value as β when $\gamma = \delta = 0$. However, the relation for β' indicates how the values of γ and δ are interconnected with the value for β for the dynamics of the scalar.[2] The parameter δ is associated with the helicity and in the helicity-free case, this parameter is equal to zero. We obtain then $\beta' = \beta$ and

$$S(k) = \frac{2\pi k}{\gamma} \tag{4.26}$$

for the helicity-free equilibrium distribution of vertical energy. This linear relation reflects an equi-partition of the energy over the modes with $S(\boldsymbol{k}) = \frac{1}{\gamma}$. The helicity spectrum is

$$H(k) = \frac{2\pi k}{\gamma} \frac{\delta k^2}{\alpha + \beta' k^2} \tag{4.27}$$

and it can be noticed that $H(k) = \dfrac{\delta}{\gamma} k^2 E(k) = \dfrac{\delta}{\gamma} W(k)$, and the helicity spectrum is proportional to the enstrophy spectrum. In order to obtain the value of the Lagrange multipliers, we need to solve a system of 4 equations. For that the value of the 4 inviscid invariants can be used:

$$Y = \int_{k_{min}}^{k_{max}} Y(k, \alpha, \beta, \gamma, \delta) \mathrm{d}k.$$

This allows to determine, for a given initial condition, quantitative predictions for the equilibrium spectra.

In figure 4.9 we show final spectra of the four invariant global quantities of the 2D3C inviscid flow. Obviously, numerical simulations confirm the independence of the horizontal velocity field from the helicity, and the spectrum $E(k)$ for the different runs are therefore statistically equivalent realizations of the same flow. Indeed, the spectra are, as in the first part of this chapter, characterized by the expected k^{-1} slope at large wave numbers. It seems that there some deviations at small scales, but these are not as dramatical as in Sec. 4.2.4, since we consider again relatively low resolutions.

The most interesting observation for the following is that the vertical kinetic energy spectra are dependent on helicity. This dependence is most important at large scales, more particularly for $k = 1$. For larger wavenumbers, equipartition of the vertical energy seems verified, as all spectra are proportional to k for larger wavenumbers.

In figure 4.8 we show a visualisation of the u_z field for both a non-helical flow and a fully-helical flow. They are very similar with no obvious difference between them despite the different energy spectra. This is somewhat expected, since, even though the first wavenumber contains more energy in the fully-helical flow than in the non-helical flow, the peak at $k = 1$ contains only 3% of the vertical kinetic energy. However, this does by no means indicate that we can neglect this difference.

Indeed, the fact that vertical kinetic energy modifies the large-scale properties of the spectra is an indication that helicity might be a persistent quantity in 2D3C flows. Indeed, equilibrium spectra give often an indication of cascade directions, as was illustrated by Kraichnan [7], and very recently for the case of 3D turbulence without vortex stretching

[2] Another way to proceed is to consider first independently the case with $\gamma = \delta = 0$ to determine α and β, and then carry out a second analysis, including helicity and variance to determine the four constants appearing in the second system. In the following the exact value of the constants is not used so this will not change the results.

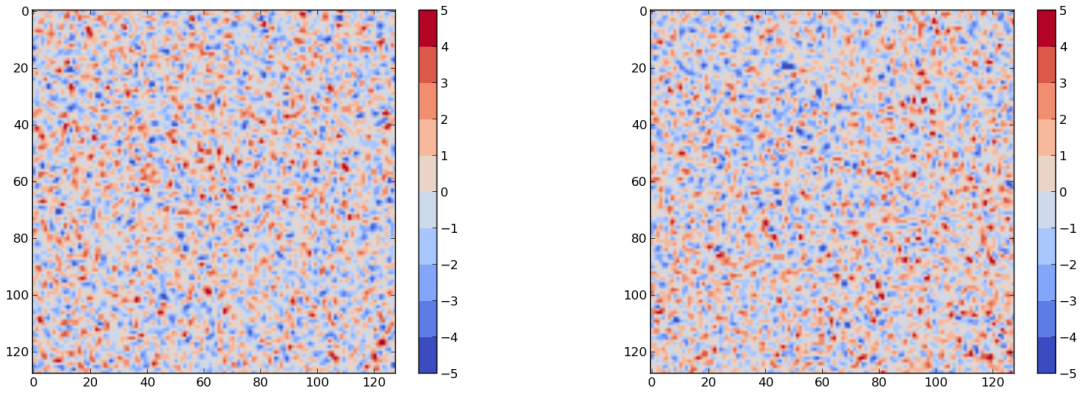

(a) (b)

Figure 4.8: Visualisation of the vertical velocity field.

[82]. The implications of this for 2D3C turbulence will now be investigated for a more realistic system in the presence of viscosity.

4.4 Application: decay of a passive scalar in two-dimensional Navier-Stokes turbulence

In this section we will illustrate the predictive power of statistical mechanics for real, viscous flow. Since Eq. (4.18) has the form of a scalar advection equation, the 2D3C flow, in the absence of forcing, corresponds to the problem of the mixing of a passive scalar at Schmidt number one.

$$\frac{\partial \boldsymbol{u}_\perp}{\partial t} + \boldsymbol{u}_\perp \cdot \nabla \boldsymbol{u}_\perp = -\nabla P + \nu \Delta \boldsymbol{u}_\perp \tag{4.28}$$

$$\frac{\partial \phi}{\partial t} + \boldsymbol{u}_\perp \cdot \nabla \phi = \nu \Delta \phi \tag{4.29}$$

with $\nabla = (\partial_x, \partial_y)$ and $\nabla \cdot \boldsymbol{u}_\perp = 0$. To stress even more the equivalence with mixing, we have introduced the notation $u_z = \phi$. We choose $\nu = 1/Re = 5.10^{-4}$, with again a Gaussian initial distribution for the vertical and horizontal energy spectrum. We choose $k_0 = 4$ and $\sigma = 2$, and a resolution $N = 256^2$. The turbulent flow decays without external forcing.

The main goal is to assess the influence of the initial relative helicity H_{rel} on the evolution of the the scalar variance $S = \int \phi^2 \mathrm{d}\boldsymbol{r}$. For that we set as initial condition

$$\phi = \tilde{\phi} + \lambda \omega \tag{4.30}$$

The part $\tilde{\phi}$ is independent from $\boldsymbol{u}_\perp$ and the relative helicity can be modified by varying λ. Both parts of the vertical velocity field are initialized with the Gaussian spectrum (4.12) and random phases.

Fig. 4.10 shows the influence of the initial relative helicity on inviscid invariants of the 2D3C flow. A common characteristic with the inviscid flow is the independence of energy and enstrophy from the initial relative helicity. On the other hand the evolution of the

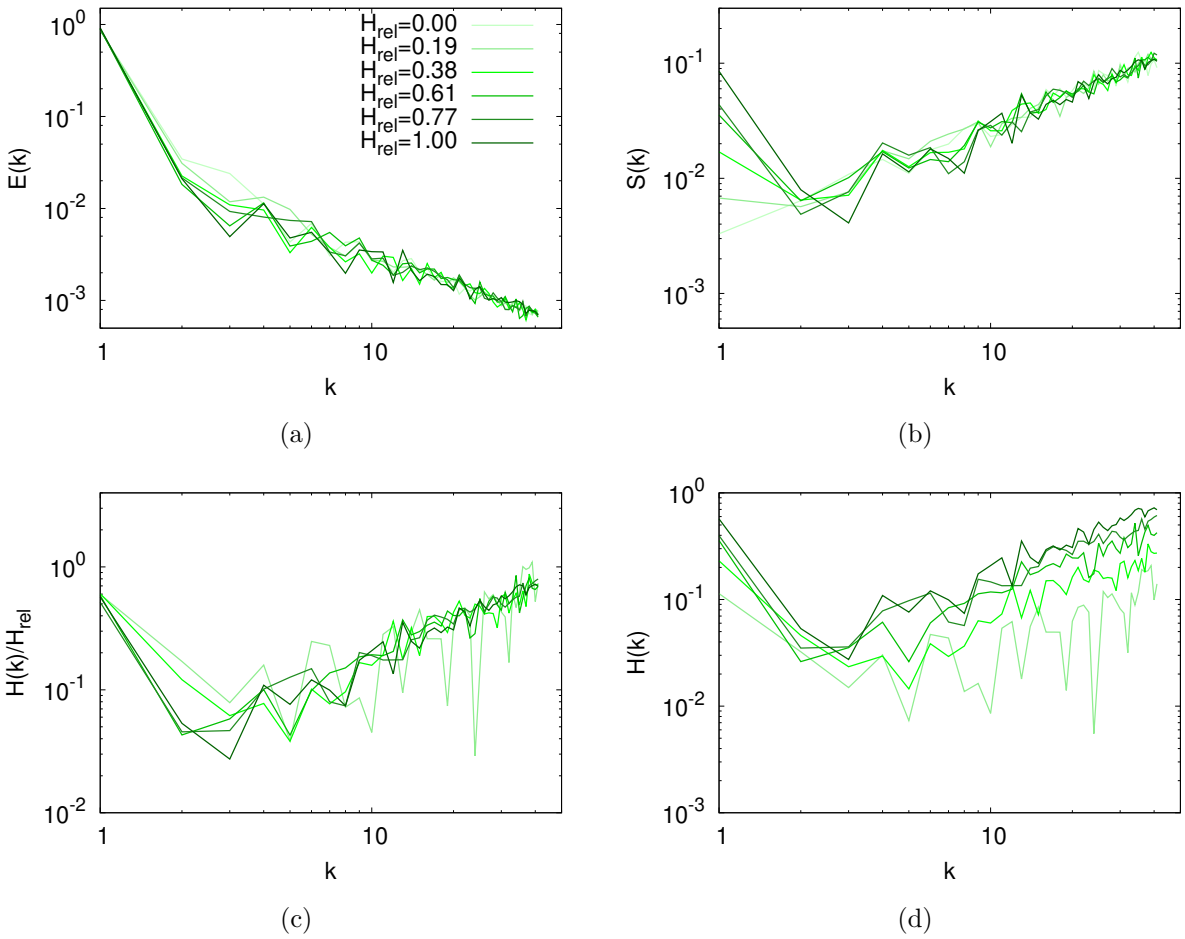

Figure 4.9: Spectra of inviscid 2D3C invariants for different values of H_{rel} for $k_{max} = 42$ and $k_{min} = 1$.

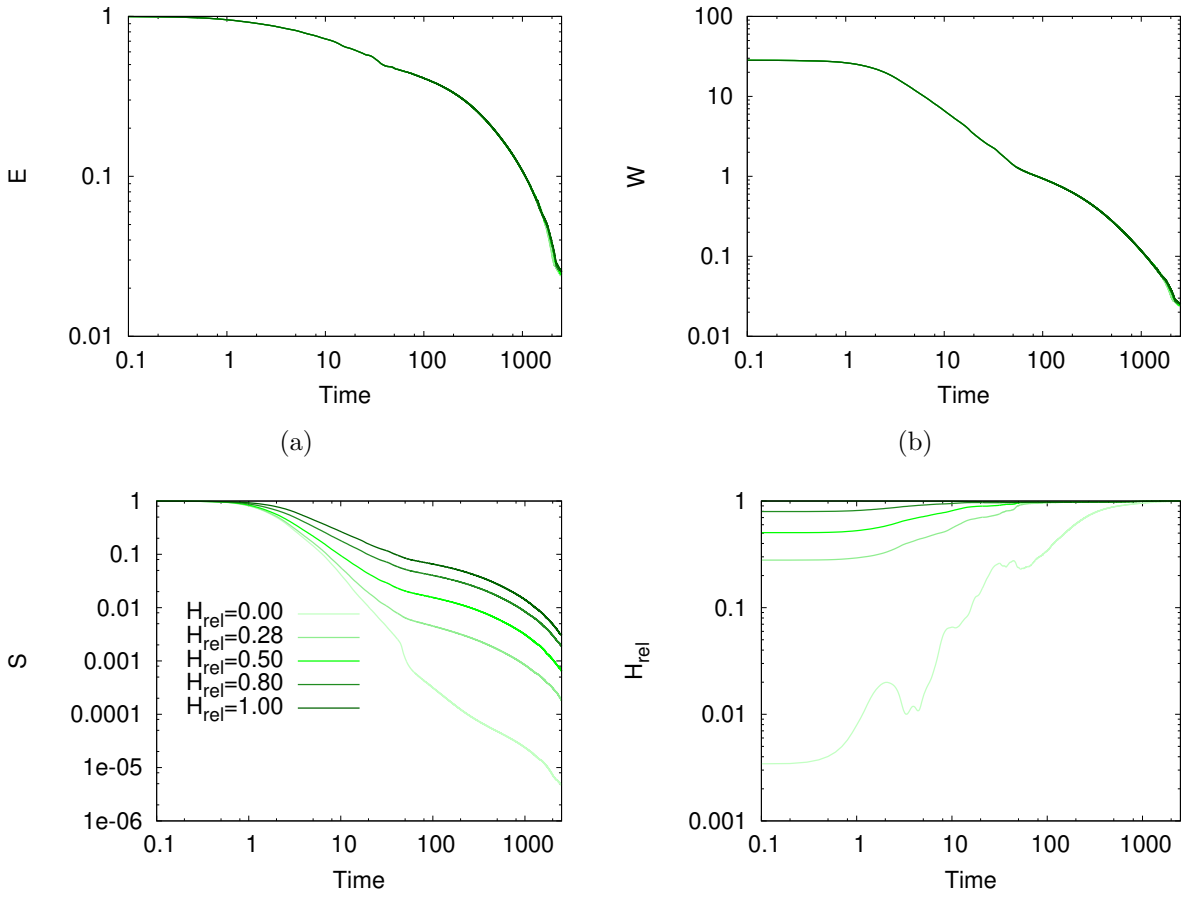

Figure 4.10: Time evolution of inviscid 2D3C invariants for different values of H_{rel}.

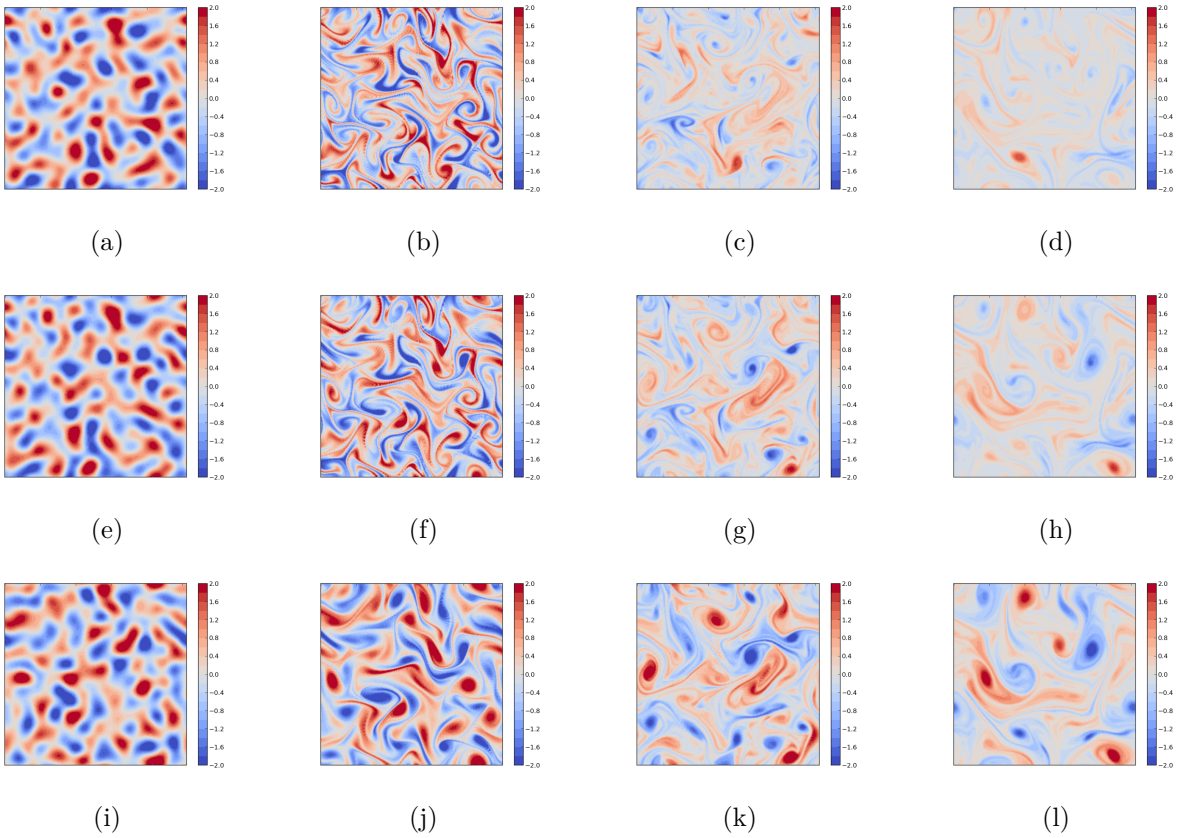

Figure 4.11: Mixing of three scalar fields. The fields have the same initial variance and spectral distribution. Furthermore the advecting velocity field is identical. The only difference is the initial correlation between scalar and vorticity. Top-row $H_{rel} = 0$, middle $H_{rel} = 0.5$, bottom $H_{rel} = 1$. From left to right, value of the scalar ϕ for $t = 0, 1, 5, 10$.

vertical kinetic energy is strongly correlated with the initial relative helicity. The higher the initial relative helicity, the faster the vertical energy decreases.

All flows tend to Beltramize, since the relative helicity tends to 1 for all of them. Even the case indicated by $H_{rel} = 0$ tends eventually to a Beltramized state. Indeed, the helicity of this case is not strictly zero but less than a percent of its maximum value. Eventually even a very small amount of helicity leads to a long-time persistent correlation, dominating the final state.

To give a visual impression of the mixing process and the influence of the helicity we show in Fig. 4.11 the decay of the Mixing of three scalar fields. The fields have the same initial variance and spectral distribution. Furthermore the advecting velocity field is identical. The only difference is the initial correlation between scalar and vorticity. Since the color-scales are the same for the three-sets of visualizations, that already at $t = 10$ the scalar variance is significantly lower in the non-correlated case.

The fact that the scalar is correlated with the vorticity does therefore allow it to persist longer in the flow. This is a rather intuitive result, since scalars which are exactly centered on a rotating blob will not experience straining. However, the fact that we can relate this observation to an invariant of the 2D3C system is an interesting feature, we think.

4.5 Conclusion of the chapter

In this chapter we showed that the statistical mechanics of two-dimensional turbulence are still an intriguing subject. Indeed, it seems that when the energy is large compared to the enstrophy, for a given range of lengthscales, a condensate forms which defies Kraichnan's statistical mechanics. The dynamics can be understood as a coexistence of a force-free condensate and a back-ground noise, the latter being well described by Kraichnan's statistical mechanics.

Furthermore, two-dimensional three-component turbulence is an interesting system, since it contains two additional invariants, compared to two-dimensional turbulence. Whereas the variance of the third component is an "obvious" invariant, the presence of the second invariant, helicity, is more surprising. Its physical interpretation should perhaps not be searched for in terms of knottedness, as for helicity in three-dimensional flows, but more directly as the pre-dominance of the sign of the helical motion of vertical structures. This is also the interpretation which emerges when considering the generation of helicity in unstable stratification in Chap. 7.

In the following we will see how these phenomena change when the third direction, in which the dynamics are invariant is not straight anymore. That system is axisymmetric turbulence.

5 Transition and helicity in 2D turbulence with curvature

5.1 2D3C flow with curvature

In the previous chapter, we investigated (standard) two-dimensional three-component flow. Such flow is described by the velocity field

$$\boldsymbol{u} = (u_x(x,y), u_y(x,y), u_z(x,y)), \tag{5.1}$$

where $u_z(x,y)$ is the out-of-plane velocity component. The dynamics of this system are fully determined by u_x, u_y, whereas u_z is advected as a passive scalar. When the out of plane direction is not straight, but curved, an alternative 2D3C flow can be defined, where the velocity field is then given, in cylindrical coordinates, by

$$\boldsymbol{u} = (u_r(r,z), u_\theta(r,z), u_z(r,z)). \tag{5.2}$$

This velocity field describes axisymmetric flow. An important difference with the flow in the previous chapter is that now the out of plane velocity u_θ can back-react on the planar dynamics. Such a flow will be considered in the present chapter.

5.1.1 Previous results on axisymmetric turbulence

In the presence of strong magnetic fields, plasmas or conducting fluids tend towards 2D3C dynamics. Indeed, the movement along the magnetic field direction is less-constrained than the perpendicular direction, where the Lorentz force acts. The presence of a strong toroidal magnetic field in fusion plasmas such as tokamaks has for a long time motivated plasma physicists to consider 2D3C plasma dynamics with curvature. Nevertheless, in the fluid dynamics community, the study of axisymmetric turbulence is relatively young.

Since the 2000s, in particular since the work of LeProvost, Chavanis and Dubrulle [44], the fluid dynamics of (5.2) was investigated theoretically. The behavior is somewhat similar to that of (5.1), but in the case of axisymmetric flow the planar and out-of-plane dynamics are, as we just mentioned, not completely decoupled.

The statistical mechanics of this system were discussed in detail in [44, 46] and more recently in [83]. The initial motivation was to develop a statistical mechanics theory which could be applied to the von Karman experiment (see e.g. [84] for the experimental set-up). The considered geometry was therefore in the initial studies a bounded cylinder. The somewhat simpler 2D2C case, where $u_\theta = 0$, was theoretically investigated in the framework of vortex-rings [85] and the case of the Taylor-Couette geometry in [47]. This

rather late interest for axisymmetric turbulent fluid flow is probably due to the fact that turbulent flow is in general not axisymmetric.

Indeed, in the turbulence modeling literature, statistically axisymmetric turbulence has been treated, using RANS approaches [86]. In such flows only the time-averaged flow is axisymmetric. However, surprisingly, the results derived for purely (instantaneous) axisymmetric turbulence were verified in fully three-dimensional turbulence with time-averaged axisymmetry only [45], giving thereby an additional motivation to continue this line of research.

In the PhD projects of Bo Qu and Zecong Qin [87, 88], axisymmetric turbulence was investigated using direct numerical simulations, aiming at the assessment of the theoretical predictions. Indeed, experimentally, turbulent fluid flows are sometimes on average axisymmetric, but never instantaneously. Therefore, even though surprising ressemblance was observed between averaged experimental results and theoretical predictions, it seemed important to verify whether the theory correctly predicted the flows for which it was derived. Numerical results of decaying axisymmetric turbulence allowed to yield first numerical evidence that some of the theoretical results were correct [48]. It was further observed that in the 2D3C state of axisymmetric turbulence, helicity seemed to be transferred to small scales [89].

This numerical line of research was pursued by Zecong Qin, [49, 56], who showed that, in the presence of linear forcing terms, a critical transition can be observed between purely poloidal and swirling flow. To understand the underlying dynamics, it is useful to compute energy spectra, fluxes and transfer mechanisms. In Qin et al. [49] preliminary observations were obtained in wall-bounded cylindrical geometry. However, Fourier-spectra are more conveniently determined in periodic domains. Periodicity is however incompatible with cylindrical coordinates in the radial direction.

In the present investigation we tackle this issue and consider a simplification which allows to consider axisymmetric turbulence in a two-dimensional periodic domain. This simplification leads to a set-up where we can verify whether the critical transition observed in the cylinder in Qin et al. is associated with the closed cylinder, or that it survives in the academic test-case of periodic boundary conditions. Furthermore, importantly, the use of periodic boundary conditions allows the use of efficient pseudo-spectral numerical methods.

5.1.2 Objectives and outline

The objectives of the present chapter are the following

- Show that axisymmetric turbulence can be investigated in two-dimensional double-periodic geometry.
- Check that in such geometry the transition between purely poloidal and swirling flow, as reported in [49] survives.
- Document the associated spectra and fluxes to understand the underlying physics

In Sec. 5.2 we will define the geometry and the governing equations of the system. It is discussed how axisymmetric turbulence can be rendered compatible with periodic boundary conditions. In Sec. 5.3 we study absolute equilibrium ensembles as in the

foregoing chapter. Then, in Sec. 5.4 we present the numerical results on the transition between purely-poloidal and swirling flow in a forced-dissipative system.

An interesting additional result, not anticipated from the outset, is that the presence of helicity can importantly modify the dynamics for some cases. This was observed for certain flows only and the details are yet to be understood, but we report these preliminary results in Appendix B.

5.2 Set-up and governing equations

In this section the governing equations are given, boundary conditions are discussed and the forcing and damping terms are introduced.

5.2.1 Axisymmetric turbulence in a periodic domain

We repeat here, for the reader's convenience, that in cylindrical coordinates the Navier-Stokes equations are described by the three velocity coordinates u_r, u_θ, u_z, which vary in the r, θ, z directions,

$$\begin{cases} \dfrac{\partial u_r}{\partial t} + \boldsymbol{u} \cdot \nabla u_r - \dfrac{u_\theta^2}{r} = -\dfrac{\partial P}{\partial r} + \nu \left(\Delta u_r - \dfrac{u_r}{r^2} - \dfrac{2}{r^2}\dfrac{u_\theta}{\partial \theta} \right) + F_r \\ \dfrac{\partial u_\theta}{\partial t} + \boldsymbol{u} \cdot \nabla u_\theta + \dfrac{u_\theta u_r}{r} = -\dfrac{1}{r}\dfrac{\partial P}{\partial \theta} + \nu \left(\Delta u_\theta - \dfrac{u_\theta}{r^2} + \dfrac{2}{r^2}\dfrac{u_r}{\partial \theta} \right) + F_\theta \\ \dfrac{\partial u_z}{\partial t} + \boldsymbol{u} \cdot \nabla u_z = -\dfrac{\partial P}{\partial z} + \nu \Delta u_z + F_z, \end{cases}$$

where the density, again assumed constant and uniform, is conveniently absorbed into the pressure.

In this expression the Laplacian Δ is defined as

$$\Delta = \frac{1}{r}\frac{\partial}{\partial r}\left(r \frac{\partial}{\partial r} \right) + \frac{1}{r^2}\frac{\partial^2}{\partial \theta^2} + \frac{\partial^2}{\partial z^2}, \tag{5.3}$$

and the gradient operator as

$$\nabla = \left(\frac{\partial}{\partial r}, \frac{1}{r}\frac{\partial}{\partial \theta}, \frac{\partial}{\partial z} \right), \tag{5.4}$$

and incompressibility is expressed by

$$\frac{1}{r}\frac{\partial r u_r}{\partial r} + \frac{1}{r}\frac{\partial u_\theta}{\partial \theta} + \frac{\partial u_z}{\partial z} = 0. \tag{5.5}$$

Axisymmetric turbulence consists of the special case where all quantities are invariant in the azimuthal direction. This means that all terms involving an azimuthal derivative $\partial/\partial\theta$ are zero. The resulting dynamics are therefore 2 dimensional, involving three velocity

components. We introduce the notation $\boldsymbol{u}_P = (u_r, u_z)$, so that we can write

$$\begin{cases} \dfrac{\partial u_r}{\partial t} + \boldsymbol{u}_P \cdot \nabla_P \, u_r - \dfrac{u_\theta^2}{r} = -\dfrac{\partial P}{\partial r} + \nu \mathcal{L} u_r + F_r, \\ \dfrac{\partial u_\theta}{\partial t} + \boldsymbol{u}_P \cdot \nabla_P \, u_\theta + \dfrac{u_\theta u_r}{r} = \nu \mathcal{L} u_\theta + F_\theta, \\ \dfrac{\partial u_z}{\partial t} + \boldsymbol{u}_P \cdot \nabla_P \, u_z = -\dfrac{\partial P}{\partial z} + \nu \Delta_P u_z + F_z, \end{cases}$$

with

$$\boldsymbol{u}_P \cdot \nabla_P = u_r \frac{\partial}{\partial r} + u_z \frac{\partial}{\partial z},$$

$$\Delta_P = \frac{\partial^2}{\partial r^2} + \frac{1}{r}\frac{\partial}{\partial r} + \frac{\partial^2}{\partial z^2}, \qquad \mathcal{L} = \Delta_P - \frac{1}{r^2},$$

while solenoidality is expressed by

$$\frac{1}{r}\frac{\partial r u_r}{\partial r} + \frac{\partial u_z}{\partial z} = 0. \tag{5.6}$$

The system is therefore similar to the 2D3C turbulence considered in the previous chapter, with the difference that the invariant direction is now curved. Due to this curvature, the dynamics change. Indeed, it is observed that on the left-hand-side of these equations two additional terms appear, $-u_\theta^2/r$ and $u_\theta u_r/r$. These terms result from the $\boldsymbol{u} \cdot \nabla \boldsymbol{u}$ term expressed in cylindrical coordinates. Similarly, the Laplacian contains additional terms, proportional to either r^{-1} or r^{-2}. An interesting observation is then that in the limit $r \to \infty$ the influence of the curvature vanishes. In that particular limit we therefore obtain the 2D3C system studied in the previous chapter.

5.2.2 Invariants

As was discussed in detail in the previous chapter, the invariants of the horizontal (u_x, u_y) dynamics in 2D3C flow are the enstrophy and the energy. The additional invariants associated with the advection of the passive scalar (or vertical velocity) are the helicity H and the variance of the scalar S. Indeed the decay of this passive third component is importantly affected by the initial condition, depending on its correlation with the vorticity field. This correlation was shown to determine the final state in the absolute equilibrium as was illustrated in Sec. 4.3. In particular the presence of helicity modified the spectral behavior at the largest scales (smallest wavenumbers).

In axisymmetric turbulence, two classes of flow-states are generally distinguished. In one case the toroidal velocity is zero and the resulting two-dimensional two-component flow is actually equivalent to the canonical case of two-dimensional turbulence, as can be shown through a change of variables [44]. The other, 2D3C or swirling flow, is different from the 2D3C flow without curvature, since energy can be exchanged between the poloidal and toroidal components through the curvature terms in the system.

In the purely poloidal 2D2C case, the invariants of the system are the poloidal kinetic energy

$$E_P = \frac{1}{2}\int_\Omega u_r^2 + u_z^2 \, \mathrm{d}\Omega \tag{5.7}$$

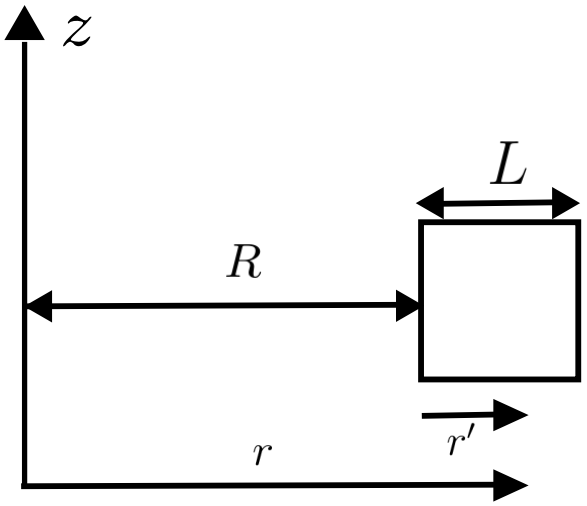

Figure 5.1: Illustration of slab-geometry, to investigate toroidal dynamics in periodic geometry.

and its associated enstrophy

$$Z = \frac{1}{2}\int_\Omega \omega_\theta^2 \, \mathrm{d}\Omega. \tag{5.8}$$

The dynamics start to differ from classical 2D turbulence when the toroidal velocity is not zero anymore. In that case enstrophy is no longer an invariant of the system, but helicity is

$$H = \int_\Omega u_\theta \omega_\theta \, \mathrm{d}\Omega. \tag{5.9}$$

In addition, it is now the sum of the toroidal and poloidal energy which is conserved,

$$E = E_T + E_P = \frac{1}{2}\int_\Omega u_\theta u_\theta \, \mathrm{d}\Omega + E_P. \tag{5.10}$$

Additional invariants are moments of the angular momentum and moments of a generalized helicity. We have not focused on these in the present chapter but these definitely deserve further focus and we will mention this in the perspectives.

5.2.3 Periodic boundary conditions

In the present chapter we want to retain the influence of curvature, but we want to consider (simple) periodic boundary conditions. The trick that we introduce is that we consider a small flow-domain and that we assume that the curvature is constant over the size of the domain. Indeed, we assume that the considered flow domain represents a small slab at a distance R from the major axis. Such an approach is rather usual in the tokamak community and the geometry is shown in Fig. 5.1. We subsequently assume that the numerical domain has a radial size L. In the limit $L/R \ll 1$, the curvature can then be considered approximately constant over the domain.

To illustrate this consider the coriolis term u_θ^2/r. In the particular case we consider, the value of this term varies from u_θ^2/R to $u_\theta^2/(R+L)$. The error made by considering the curvature constant over the domain is then of order

$$\mathrm{Err} = (\frac{u_\theta^2}{R} - \frac{u_\theta^2}{R+L}) \approx \frac{u_\theta^2}{R}(1 - \frac{R}{R+L}) = \frac{u_\theta^2}{R}\frac{L}{R+L} \tag{5.11}$$

so that the relative error, $Err/(u_\theta^2/R)$ is, for $R \gg L$ of order $\mathcal{O}(L/R)$. Once the terms involving explicitly the position $r = R + r'$ are replaced by terms where a constant value R is used, periodic boundary conditions can be introduced. An implication of this assumption is that we can only focus on flow structures of size smaller or equal to L, which is small compared to the lengthscale R.

The set of equations used in the following is then

$$\begin{cases} \dfrac{\partial u_r}{\partial t} + \boldsymbol{u}_P \cdot \nabla_P u_r - \dfrac{u_\theta^2}{R} = -\dfrac{\partial P}{\partial r} + \nu \mathcal{L} u_r + F_r, \\ \dfrac{\partial u_\theta}{\partial t} + \boldsymbol{u}_P \cdot \nabla_P u_\theta + \dfrac{u_\theta u_r}{R} = \nu \mathcal{L} u_\theta + F_\theta, \\ \dfrac{\partial u_z}{\partial t} + \boldsymbol{u}_P \cdot \nabla_P u_z = -\dfrac{\partial P}{\partial z} + \nu \Delta_P u_z + F_z, \end{cases}$$

where

$$\boldsymbol{u}_P \cdot \nabla_P = u_r \frac{\partial}{\partial r} + u_z \frac{\partial}{\partial z},$$

and where

$$\Delta_P = \frac{\partial^2}{\partial r^2} + \frac{1}{R}\frac{\partial}{\partial r} + \frac{\partial^2}{\partial z^2} \qquad \mathcal{L} = \Delta_P - \frac{1}{R^2}.$$

The incompressibility now becomes,

$$\frac{\partial u_r}{\partial r} + \frac{u_r}{R} + \frac{\partial u_z}{\partial z} = 0. \tag{5.12}$$

We have in these equations tacitly replaced the local radial coordinate r' by r.

It is at this point convenient to introduce a stream-function ψ, associated with the poloidal dynamics. For the exact equations, the relation between the stream-function and the velocity reads $u_r = -\partial\psi/\partial z$ and $u_z = r^{-1}\partial(r\psi)/\partial r$. In our slab-approximation this becomes at leading order,

$$u_r = -\frac{\partial \psi}{\partial z} \quad \text{and} \quad u_z = \frac{\psi}{R} + \frac{\partial \psi}{\partial r}. \tag{5.13}$$

The relation between the stream-function and the toroidal vorticity is

$$\omega_\theta = -\mathcal{L}\psi, \tag{5.14}$$

and Poisson brackets for our system write,

$$[a, b] = \left(\frac{\partial a}{\partial r} + \frac{a}{R}\right)\frac{\partial b}{\partial z} - \frac{\partial a}{\partial z}\frac{\partial b}{\partial r}.$$

This notation allows to write the full 2D-3C dynamics as a function of the two scalar fields $u_\theta(r, z)$ and $\psi(r, z)$

$$\begin{cases} \dfrac{\partial u_\theta}{\partial t} + [\psi, u_\theta] = \nu \mathcal{L} u_\theta + \dfrac{u_\theta}{R}\dfrac{\partial \psi}{\partial z} + F_\theta, \\ \dfrac{\partial \psi}{\partial t} = \nu \mathcal{L}\psi + \mathcal{L}^{-1}\left([\psi, -\mathcal{L}\psi] - \dfrac{\mathcal{L}\psi}{R}\left(\dfrac{\partial \psi}{\partial z}\right) - \dfrac{1}{R}\dfrac{\partial u_\theta^2}{\partial z}\right) + F_\psi, \\ \omega_\theta = -\mathcal{L}\psi, \end{cases}$$

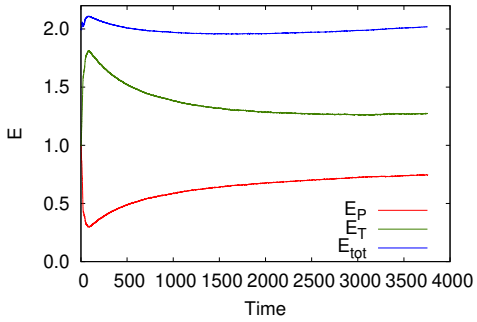

(a)

Figure 5.2: Poloidal and toroidal energy in the truncated axisymmetric system.

with $F_\psi = -\mathcal{L}^{-1}(\nabla \times \boldsymbol{F}_P) \cdot \boldsymbol{e}_\theta$, the poloidal force being defined by

$$\boldsymbol{F}_P = (F_r \boldsymbol{e}_r + F_z \boldsymbol{e}_z). \tag{5.15}$$

We have at this point succeeded to express the full 2D3C dynamics as the evolution of two scalar fields, which are compatible with periodic boundary conditions. Such boundary conditions allow to use pseudo-spectral methods, which simplifies the computation of the derivatives, Laplacians and the inverse operators such as $\mathcal{L}^{-1}$.

5.3 Galerkin truncated Euler dynamics

Given the insights obtained from the last chapter, it seems useful to investigate the equilibrium statistical mechanics of the periodic axisymmetric system.

A theoretical investigation of the Galerkin-truncated axisymmetric system is presented in chapter 3 of Simon Thalabard's thesis [90]. It is shown there that this approach, at least from a theoretical point of view leads to somewhat ambiguous results. For instance, the Galerkin truncation does not conserve kinetic energy. Indeed, the detailed conservation of quantities depends on symmetry-properties of the nonlinearity expressed in a given coordinate system. It seems that for cylindrical coordinates this symmetry is broken and energy is no longer an invariant of the Galerkin-truncated system. This non-conservation is similar to the case of two-dimensional turbulence, where many Casimir-invariants can be defined [44], but where only energy and enstrophy are invariants which survive Galerkin-truncation. This consequence of the truncation should not impact energy-conservation by the nonlinearity in a sufficiently resolved forced-dissipative system.

However, for this reason (energy-non-conservation), we investigate here two specific systems. The first one is the just derived (non-conservative) system, corresponding to double-periodic axisymmetric dynamics. The second system is the simplified system obtained by considering the 2D3C system (as in the previous chapter), while keeping the Coriolis terms which allow to transfer energy between the different components.

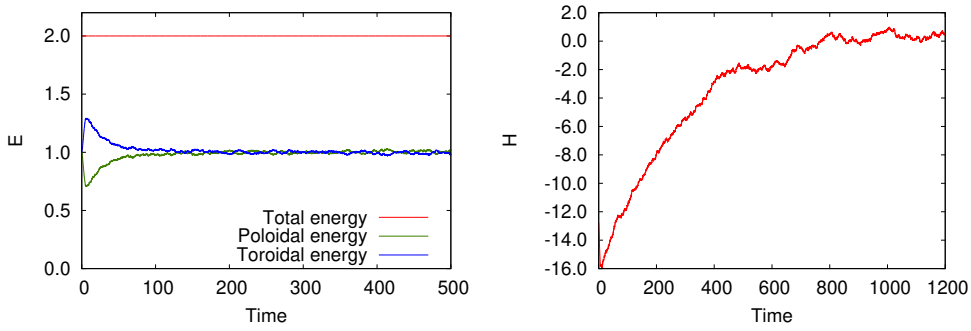

(a) (b)

Figure 5.3: Temporal evolution of (a) energy (b) helicity during the relaxation to equilibrium of the energy conserving truncated Euler system.

5.3.1 "Full" truncated axisymmetric Euler

Removing viscous and forcing terms from Eqs.(5.2.3), we obtain the system of the following two coupled equations.

$$\frac{\partial u_\theta}{\partial t} + [\psi, u_\theta] = \frac{u_\theta}{R}\frac{\partial \psi}{\partial z} \tag{5.16}$$

$$\frac{\partial \mathcal{L}\psi}{\partial t} + [\psi, \mathcal{L}\psi] = -\frac{\mathcal{L}\psi}{R}\left(\frac{\partial \psi}{\partial z}\right) - \frac{1}{R}\frac{\partial u_\theta^2}{\partial z}, \tag{5.17}$$

$$\omega_\theta = -\mathcal{L}\psi. \tag{5.18}$$

The left-hand sides of these equations correspond to the Cartesian 2D3C system, while the right-hand sides couple the poloidal and toroidal components. As shown by Thalabard [90], this system does not conserve energy.

Simulations are again carried out using GHOST, starting from random initial conditions with spectral distribution (4.12). We initialize a spectrum with a finite amount of helicity. We use the value $R = 4\pi$.

We illustrate the energy distribution between the components numerically in Fig. 5.2, where we show a rapid transfer of energy between the velocity components for short time. Then, for longer times, the total energy increases slowly.

We investigated the system and observed that for large values of R the system conserves the energy. This is the desired behavior, since for large R the system degenerates into the 2D3C dynamics discussed in Chap. 4. Nevertheless this variation of the total energy is not a very desirable quantity so we do not further explore this truncated system.

5.3.2 Toy model

Indeed, since we are, in the following, interested in practical applications (such as tokamaks, or geophysics), we do think that energy conservation is an important constraint on the dynamics. We therefore also investigate the dynamics of the modified system,

$$\frac{\partial u_\theta}{\partial t} + (\boldsymbol{u}_P \cdot \nabla_P) u_\theta = -\frac{u_\theta u_r}{R} \tag{5.19}$$

$$\frac{\partial \omega_\theta}{\partial t} + (\boldsymbol{u}_P \cdot \nabla_P) \omega_\theta = \frac{1}{R}\frac{\partial^2 u_\theta^2}{\partial z^2}, \tag{5.20}$$

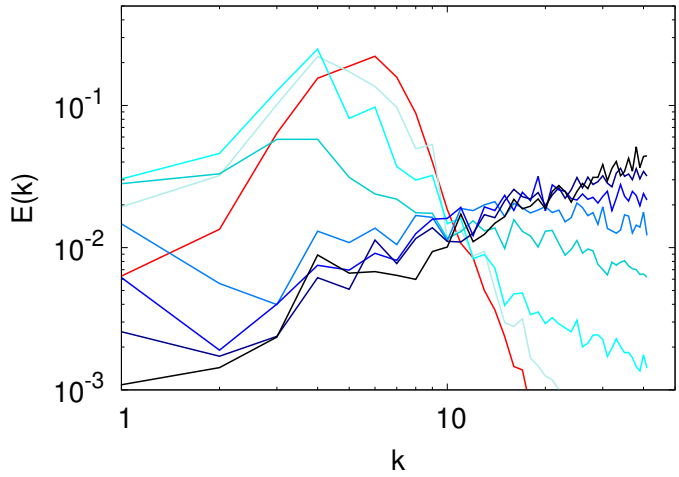

Figure 5.4: Relaxation to absolute equilibrium of the energy conserving truncated Euler system at t=0 in red and t=1,2,5,10,20,50,1000

with $\omega_\theta = \partial_z u_r - \partial_r u_z$. This system is obtained by taking the Cartesian 2D3C system and adding the Coriolis terms resulting from the advection term in cylindrical coordinates. In some sense, this is a hybrid formulation which breaks enstrophy conservation, compared to 2D3C flows, but allows energy transfer between the components. Importantly this formulation restores energy conservation. These features seem desirable if one is to study axisymmetric turbulence.

We use the same numerical set-up and parameters as in the previous paragraph. Results for the toroidal and poloidal energy and their sum are shown in Fig. 5.3(a). From this figure two features are remarkable. Firstly energy is perfectly conserved, as desired. Secondly, energy is at long times evenly distributed between the two components. In Fig. 5.3(b) it is shown that the helicity is not conserved by the system. However, the helicity of the flow decays only slowly, so that, during a long transient, helicity might play a role in the dynamics.

In Fig. 5.4 we show the relaxation to absolute equilibrium of the system, as illustrated by the evolution of the kinetic energy spectrum. The first observation, comparing to the Cartesian 2D3C cases assessed in the foregoing chapter, is that for large k the spectrum is proportional to k, whereas for the 2D3C system this was the case only for the $E_z(k)$ contribution, but not for the horizontal spectrum, which reflected enstrophy equipartition, proportional to k^{-1}. Since enstrophy is now not an invariant, the equilibrium distribution does not need to satisfy this constraint and the equilibrium spectra are reflecting energy equipartition.

A feature that we might overlook if we only consider the long-time equilibrium spectrum, is that at short times energy increases at the lowest wavenumber. Indeed, while the initial condition peaks around $k = 6$, at short times ($t < 10$), some energy seems to accumulate around $k = 1$, before it drops towards equipartition. The underlying physics of this transient are the fact that, even though helicity is not an invariant of the system. The system degenerates towards a 2D3C system for $R \to \infty$. For such systems helicity conservation is manifested by a peak in the energy spectrum at the longest wavelengths (here around $k = 1$). In the transient, a trace of this is thus visible (as is also illustrated in Fig. 5.3(b) for the total value of the helicity). For large values of R, helicity might

therefore play an important role in the physics of axisymmetric turbulence.

5.4 Axisymmetric turbulence with forcing and dissipation

In this section we first define the forcing-terms and justify the choice of the parameters before presenting results on the transition between 2D2C and 2D3C axisymmetric turbulence.

5.4.1 Definition of the forcing terms

In addition to periodic boundary conditions, which allow to consider a flow-dynamics which, from a numerical point of view, is statistically homogeneous, it is convenient to consider statistically stationary flow. For this we introduce forcing terms which introduce energy into the flow. In engineering or geophysical flows, forcing terms are in general associated with mean-velocity gradients, magnetic fields or buoyancy forces. All these types of forcing introduce preferred directions into the flow and the statistics become thereby anisotropic, and often inhomogeneous. To consider the most symmetric, academic type of energy injection, isotropic forcing is used in the majority of theoretical studies which do not focus on anisotropic or inhomogeneous flows. We will here consider a force which does not explicitly introduce anisotropy in the poloidal plane.

A next question is which type of isotropic forcing is considered. A well known type is random forcing, where the force is not correlated with the velocity field. In our study we specifically use another type, which is linear forcing. The reason for this is that an important number of natural phenomena are intimately associated with this type of forcing. Indeed, many real-life turbulent flows, such as turbulent convection, and boundary layer transition are generated by linear instabilities.

The easiest expression to understand such linear forcing is

$$\frac{dX(t)}{dt} = cX(t) + \text{other terms.} \tag{5.21}$$

The linear term $cX(t)$, will lead, in the absence of other mechanisms to an exponential growth of $X(t)$. In many systems, such behavior is observed at small times, until nonlinear terms become dominant. The direct use of a linear forcing term proportional to the velocity in the Navier-Stokes equations was proposed by Lundgren [91]. Such forcing is extremely simply to implement in numerical schemes. We investigated its properties in isotropic turbulence, associated with the transition to sustained turbulence and this study is reported elsewhere [92].

In reality, not all different lengthscales are equally unstable in natural flows, and often a physical effect will trigger a linear instability at a given wavelength or wavenumber. It is in these cases convenient to add a linear force term exclusively at a wavenumber, or a small band of wavenumbers. The forcing terms we apply are defined as follows

$$\begin{cases} F_r(\mathbf{k}) = \left[C_P u_r(\mathbf{k}) - c_3 |u_P|^2(\mathbf{k}) u_r(\mathbf{k})\right] \Pi(k_1, k_2) \\ F_z(\mathbf{k}) = \left[C_P u_z(\mathbf{k}) - c_3 |u_P|^2(\mathbf{k}) u_z(\mathbf{k})\right] \Pi(k_1, k_2) \\ F_T(\mathbf{k}) = \left[C_T u_\theta(\mathbf{k}) - c_3 |u_T|^2(\mathbf{k}) u_\theta(\mathbf{k})\right] \Pi(k_1, k_2) \end{cases} \tag{5.22}$$

where the forced wavenumber intervals are defined by

$$\Pi(k_1, k_2) = \begin{cases} 1 & \text{if } |\mathbf{k}| \in [k_1, k_2] \\ 0 & \text{elsewhere} \end{cases}$$

In these expressions we do not only show the linear forcing terms, but also cubic damping terms which are proportional to $|u_P|^2 \equiv |u_r|^2 + |u_z|^2$ or $|u_T|^2 \equiv |u_\theta|^2$. This combination of linear and cubic damping terms is typical in studies of active turbulence such as in the Toner-Tu model [93, 94, 95] and they were recently used to study two-dimensional turbulence [96]. Indeed, in the absence of such damping, the energy in the forced modes of two-dimensional turbulence too rapidly increases until nonphysical numerical artefacts appear.

This forcing and damping acts thus at intermediate scales and the viscosity, as usual, on the small scales. In the case where the turbulence is close to a 2D2C state, we expect an inverse cascade of energy. The presence of such a transfer of energy towards the smallest k values of the domain will lead to an eventual condensation until the system blows-up due to numerical instabilities. We therefore add a hypofriction to the largest scales of the system. To concentrate its influence to a narrow range of scales, we add to the right hand side of the poloidal dynamics Eq. 5.2.3, to the equation of ψ a term $-c_\psi \Delta^{-2}\psi$, which is easily implemented in Fourier-space, by adding to the equation for the Fourier-coefficient $\tilde{\psi}$ a term $-c_\psi k^{-4}\psi$.

5.4.2 Parameters

Now that we have defined the governing equations, the boundary conditions and the energy input, we can proceed to a numerical integration of the system.

We need to define the size of the domain and the size of the energy injection scales $[k_1, k_2]$. We define the size of the domain conveniently to be a square of size $L = 2\pi$, which corresponds to a minimum wavenumber in the x, y–directions of unity. The resolution is set to 512^2 grid-points, which allows to carry out long simulations, which turns out to be important in our simulations, since rare transitions can be observed between different flow-states. The major axis R is chosen to be $R = 4\pi$. While this does not satisfy the criterion $L/R \ll 1$, we have chosen this value to assess the influence of the curvature. Indeed, in the asymptotic limit where $L/R \ll 1$, the influence of the curvature terms becomes negligible and the system becomes equivalent to the one studied in the previous chapter. The choice $R/L = 2$ must then be seen as a compromise to assess the effect of curvature, while still using periodic boundary conditions. Furthermore, this is also the order of magnitude of the curvature in the tokamak-like geometry in the following chapter.

To allow for an assessment of energy, enstrophy and helicity cascades in both forward and inverse directions in scale space, we choose the forcing scale of intermediate size, at $[k_1 : k_2] = [16 : 18]$. Whereas this is a good choice to assess the presence of an inverse cascade, leaving enough wavenumber space between the injection scale and the box-size, it turns out that this choice will have an incidence on the influence of the curvature on the dynamics.

The viscosity $\nu = 1/Re$ determines the smallest active scales and is adapted as a function of the numerical resolution. Its value is here set at 1/4000. The parameters associated with the forcing, C_T and C_P are the main control parameters of the system.

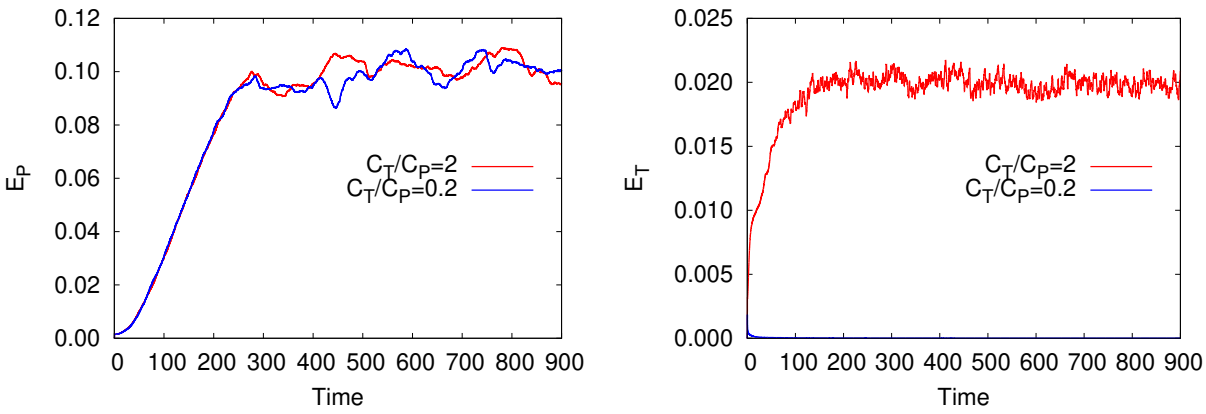

(a) (b)

Figure 5.5: Time evolution of poloidal energy (a) and toroidal energy (b) in two simulations. For the first case $C_T/C_P = 0.2$ the flow is poloidal, as is illustrated by the fact that the toroidal energy decays to a negligible value. For the second $C_T/C_P = 2.0$ and both energies show an evolution around a statistically steady state.

We fix one of these forcing parameters, setting $C_P = 10$ and vary the value of C_T in the range $C_T \in [0 : 20]$. Indeed, it was shown in [49] that the ratio of the constants was the most important parameter to trigger the transition. The cubic damping parameter is set to $c_3 = 2 \cdot 10^{-5}$. The hypo-friction constant is set to $c_\psi = 0.005$.

5.4.3 Results on the critical transition

Two general classes of flows were identified in [49], swirling and non-swirling, the transition being triggered by the forcing-anisotropy C_T/C_P. In the present set-up, we similarly assess this transition. The initial condition from which we start is small amplitude Gaussian noise with a spectral energy distribution Eq. (4.12), identical for both the poloidal and the toroidal energy, but with independent random phases.

A parameter-scan is carried out, varying C_T/C_P and the poloidal and toroidal energies of two characteristic runs are shown in Fig. 5.5. We similarly identified the two regimes. For the case where $C_T/C_P = 0.2$, it is observed that the poloidal energy grows towards a statistically steady state, whereas the toroidal energy decays from the initial condition to negligibly small values. The dynamics of this case should be close to that of two-dimensional turbulence.

For the other case shown in the Figure, $C_T/C_P = 2$, both toroidal and poloidal energies approach a statistically steady state. The level of the poloidal flow, which is driven by the same forcing-strength, is not significantly affected by this appearance of a toroidal component. This shows that the toroidal flow does not exchange much energy with the poloidal component and we will come back to this observation.

These results indicate that the critical transition [49] seems to persist in the present set-up. This is illustrated in Fig. 5.6, where we show the ratio of the time-averaged values of E_T and E_P during the statistically steady states. We can identify a critical value of the ratio which is situated at order unity in between $C_T/C_P|_{\text{crit}} \approx 0.3$. For lower values of the forcing ratio the flow tends to a strictly poloidal dynamics, which should in principle be characterized by an inverse cascade of energy.

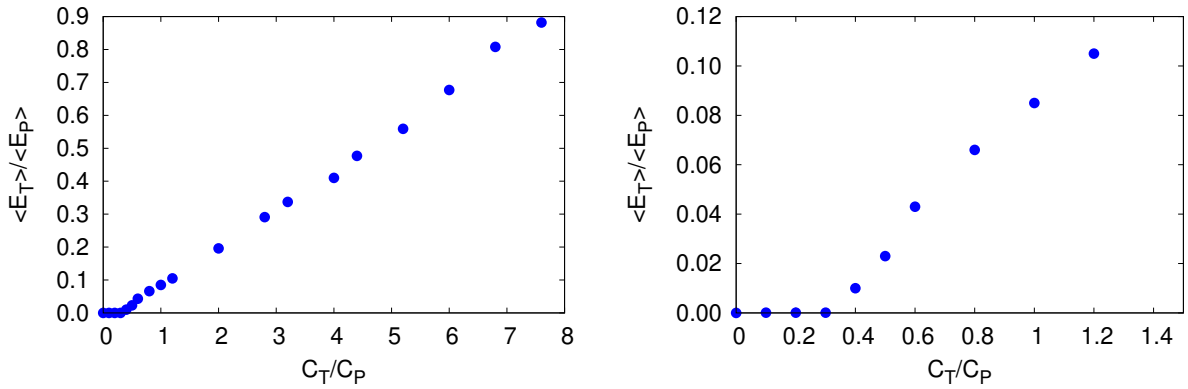

(a) (b)

Figure 5.6: (a) Influence of the forcing anisotropy C_T/C_P on the toroidal to poloidal kinetic energy ratio. The ratio is computed using the time-averaged values of the two kinetic energy components during the statistically steady state. Fig. (b) is a zoom on the small values of the range of C_T/C_P.

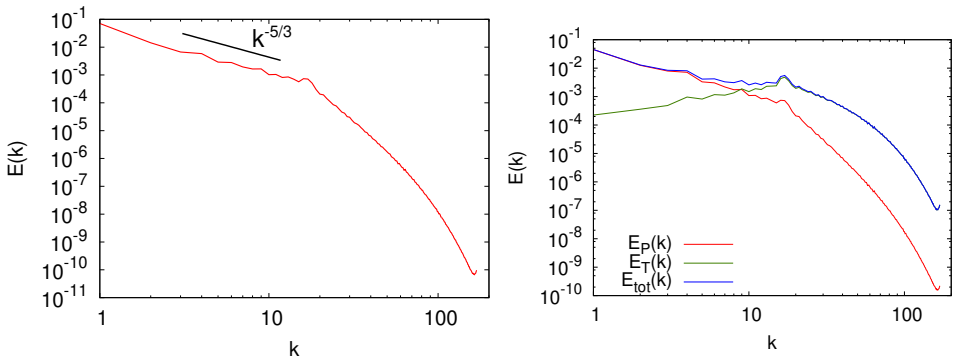

Figure 5.7: Time-average energy spectrum $C_T/C_P = 0.2$ and $C_T/C_P = 6.0$

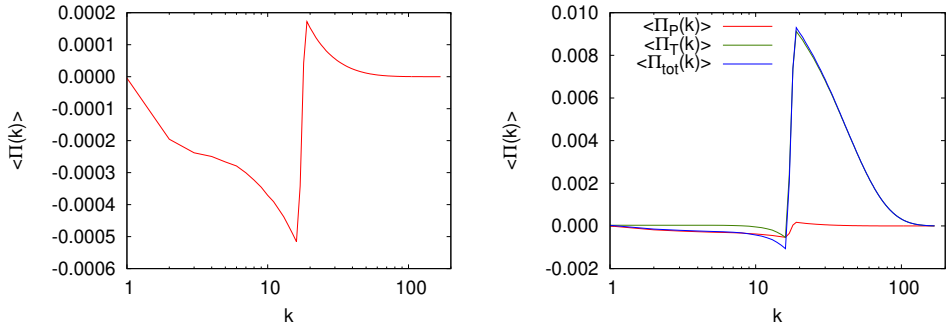

Figure 5.8: Time-averaged flux spectra for $C_T/C_P = 0.2$ and $C_T/C_P = 6.0$

Energy spectra associated with the two flows are shown in Fig. 5.7. It is observed that the scales larger than the forcing scale are not incompatible with a $k^{-5/3}$ wavenumber. This is the case for the poloidal spectra for values on both side of the critical transition. Indeed, it is observed that for the case of $C_T/C_P = 6$ the inverse cascade survives, and is not significantly affected by the presence of the toroidal component.

It is observed that the spectrum of the toroidal kinetic energy is much shallower, reflecting the direct cascade of energy we already encountered in the last chapter for the passively advected third component in 2D3C flow. The results confirm that this toroidal energy is not significantly transported towards the large scales. Indeed, for $k < k_f$ we observe an approximate equi-partition of toroidal kinetic energy with $E_T(k) \sim k$.

In Fig. 5.8 we plot the different fluxes of energy. Fig. 5.8(a) shows the dominant flux towards large scales, corresponding to the negative part of the flux spectrum. For k tending towards unity, the flux vanishes, which shows that the poloidal flux at the large scales is absorbed by the large-scale friction. At large k a (smaller) positive flux of energy is observed, directly dissipated by viscous dissipation.

In Fig. 5.8(b) we show the spectra associated with fluxes of poloidal and toroidal energy, and their sum. It is observed that the toroidal flux is mainly towards large k, reflecting the forward toroidal energy cascade. We also show that for the present choice of parameters, the toroidal flux is an order of magnitude larger than the poloidal flux.

To give an idea of the flow structures, we show visualizations of both poloidal and the toroidal fields for two typical cases in Fig. 5.9.

5.4.4 Influence of the curvature on the dynamics

The transition observed in the foregoing does not seem to affect the poloidal dynamics significantly. As such, it seems that the dynamics are close to the Cartesian 2D3C flows, where the toroidal component is passive.

In the present case, the global poloidal and toroidal kinetic energy balances read

$$\frac{dE_P}{dt} = I_P - \varepsilon_P + T \tag{5.23}$$

$$\frac{dE_T}{dt} = I_T - \varepsilon_T - T \tag{5.24}$$

where I_P and I_T represent the energy injected by the forcing terms Eq. (5.22) and ε_P and ε_T the dissipation mechanisms. Most importantly for our discussion, the coupling terms

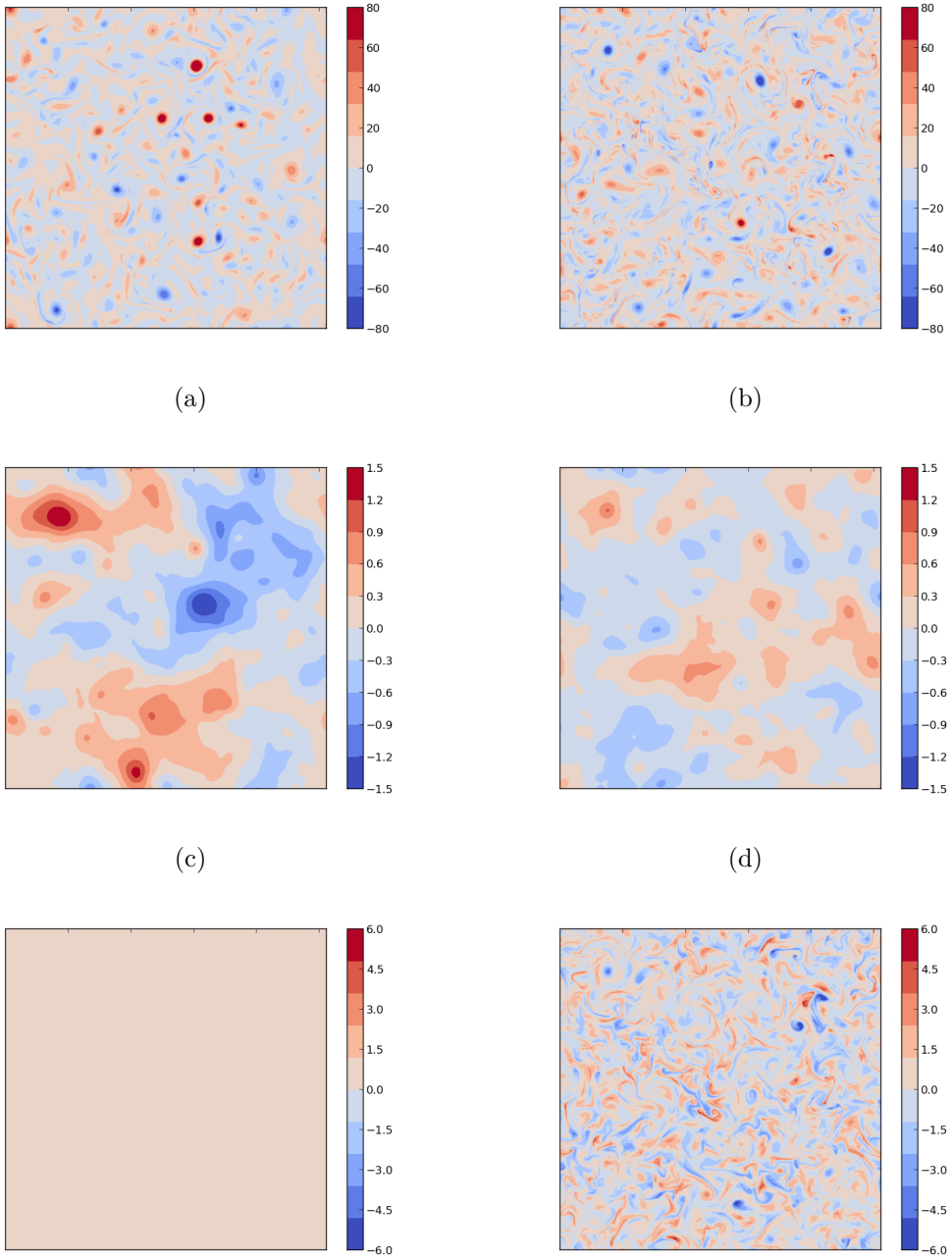

Figure 5.9: Visualizations of the flow-field during the statistically steady state for the flows with $C_T/C_P = 0.2$ (left) and $C_T/C_P = 6$ (right). The displayed quantities are vorticity ω_θ (a,b), streamfunction ψ (c,d) and toroidal velocity u_θ (e,f).

in the energy balance allow for an average energy transfer between the components equal to

$$T = \frac{\langle u_\theta^2 u_r \rangle}{R}. \tag{5.25}$$

The order of magnitude of this flux can be estimated by

$$\mathcal{O}(T) \sim \frac{E_T E_P^{1/2}}{R}. \tag{5.26}$$

The order of magnitude of the toroidal energy flux is set by the parameters used in the forcing protocol, but are in particular determined by the lengthscale k_f^{-1} where the forcing acts. Indeed, for a scalar, an extension of Taylor's estimate for the dissipation rate writes

$$\mathcal{O}(\epsilon_T) \sim \frac{E_T E_P^{1/2}}{k_f^{-1}}, \tag{5.27}$$

where we used the forcing-scale is taken as a typical lengthscale, since it is poloidal velocity structures at these scales which act most vigorously at the injection scale of the scalar.

The fact that

$$\frac{k_f^{-1}}{R} \ll 1, \tag{5.28}$$

determines that for an important part of the parameter space, the transfer T is negligible compared to the fluxes associated with the nonlinear transfer of energy. Indeed, we have $R = 4\pi$ and $k_f \approx 17$, so that $Rk_f \approx 200$ and therefore only for rather extreme cases the influence of the curvature becomes important. We illustrate this by computing the wavenumber spectra associated with the term T in Eqs. (5.23) and (5.24). Even though the terms in both global energy equations are equal, their scale distribution is not necessarily so. These are given by

$$T_{P\to T}(k) = -\int_{\mathbb{R}^3} \frac{\widehat{u_r^* u_\theta^2}}{R} \delta(|\boldsymbol{k}| - k)\, \mathrm{d}\boldsymbol{k} \tag{5.29}$$

$$T_{T\to P}(k) = \int_{\mathbb{R}^3} \frac{\widehat{u_\theta^* u_\theta u_r}}{R} \delta(|\boldsymbol{k}| - k)\, \mathrm{d}\boldsymbol{k}. \tag{5.30}$$

In Fig. 5.10 we show the lengthscale distribution of the transfer between the toroidal and poloidal components. An interesting feature of this transfer is that the transfer between the components is not at all a process involving only one lengthscale. Indeed it is observed that energy is extracted around the forcing scale from the poloidal component and that it is injected into the poloidal component around the scale of the domain-size.

Perhaps an even more important information is that the strength of the transfer is several orders of magnitude smaller than the nonlinear transfer for a given component. Possibly by changing the forcing-scale, injecting toroidal energy in scales comparable to R the curvature terms could become important. This is an important information and will be taken into account in setting up the simulations in the next chapter.

5.4.5 Helicity formation

In the previous results we have not observed any influence of the helicity. In Chap. 4 it was shown that helicity is associated with the $k = 1$ mode in the 2D3C system. Even though

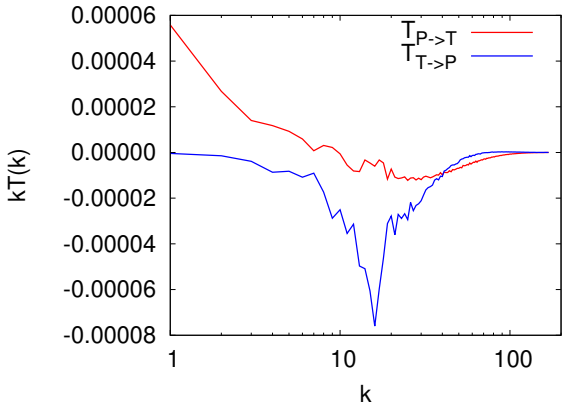

Figure 5.10: Spectral locality of poloidal/toroidal transfer

we have curvature, possibly this feature persists since our dynamics are not far from a Cartesian 2D3C dynamics since the curvature flux is small compared to the nonlinear flux. We have some preliminary results, which we did not manage to explore at the time of this writing, where helicity seems to play a role, and these results are reported in Appendix B.

5.5 Conclusion of the chapter

We have in the current chapter investigated axisymmetric turbulence in periodic "slab" geometry. The results remain exploratory and the number of open questions is large enough to dedicate a complete thesis to the dynamics. We here conclude this chapter but insist on two points that will be of interest in the rest of this thesis.

The first observation is the subsistence of a critical transition between 2D2C and 2D3C dynamics. Indeed, in the following chapter (Chap. 6), we investigate the critical transition from poloidal to three dimensional dynamics in toroidal geometry, mimicking the dynamics of a tokamak.

Another insight is that, if the injection-scale is much smaller than the curvature scale, the influence of the curvature on the 2D2C-2D3C transition is small. This is intuitively understandable, since for very small scales l the influence of advection through turbulent motion, compared to the effects of curvature should scale as l/R. In the next chapter we inject therefore the energy at scales which are comparable to the domain size.

The other observation that we will come back to is the spontaneous generation of helicity, observed near the onset of 2D3C flow (see Appendix B). In the final chapter of this thesis (Chap. 7), we investigate the generation of helicity in a geophysically motivated geometry, where unstable stratification (a linear forcing mechanism) is combined with a strong magnetic field, allowing the field to approach the 2D3C limit.

6 A fluid mechanics explanation for enhanced confinement in tokamaks

Tokamak[1] fusion plasmas can operate in two regimes, L-mode and H-mode. This latter mode, where turbulence is reduced, is beneficial for the reactor performance and will be essential to reach the goal of profitable energy production. Despite the observation of the transition between these regimes in a wide range of fusion experiments, the origin of the transition itself is not understood. What lacks is a generic global explanation of what happens during the LH-transition. We show, using numerical experiments, that on the level of a fluid description of the fusion plasma, observations can be explained as the result of a transition of the turbulent plasma flow from a nearly two-dimensional state, with three velocity components, to a purely two-dimensional flow, involving only two components. This latter flow-state allows the self-organization of the plasma to a quiescent dynamics, characterized by long-living coherent structures. When these large-scale structures orient in the azimuthal direction, the radial transport is reduced. We show thus that these two ingredients, the transition to poloidal dynamics plus symmetry breaking, are essential to attain a flow field beneficial for confinement.

6.1 The LH transition and two-dimensional turbulence

Thermonuclear fusion is a sustainable and carbon-free energy source. It can thereby constitute a game-changer in the context of energy regulation and climate change. Currently the most advanced geometry to achieve the ultimate goal of a sustained large-scale fusion reaction is the tokamak: in a torus-shaped reactor chamber, magnetic fields are used to confine a plasma at a temperature of hundreds of millions degrees, in which energy is produced by fusion of hydrogen isotopes. A schematic of toroidal geometry, indicating the definitions of toroidal and poloidal directions, is shown in Fig. 6.1.

The largest obstacle for fusion is the confinement of a plasma. Indeed, if any reactor is to produce energy by a fusion reaction, the ionized gas of hydrogen isotopes should be kept at a sufficient temperature, with a sufficient density for a long enough period of time. This triple criterion (time, density and temperature) has been known since the 1950s [97] and the goal of almost any magnetically controlled fusion experiment is to enhance this triple product. Currently, tokamaks cannot work without continuous injection of energy in the plasma, and they produce less energy than they need to sustain the reaction. The ITER experiment aims at showing that tokamaks can reach, and go beyond, the break-even point.

[1]This chapter largely follows the preprint of the same title, with authors W. Agoua, B. Favier, J. Morales & W.J.T. Bos

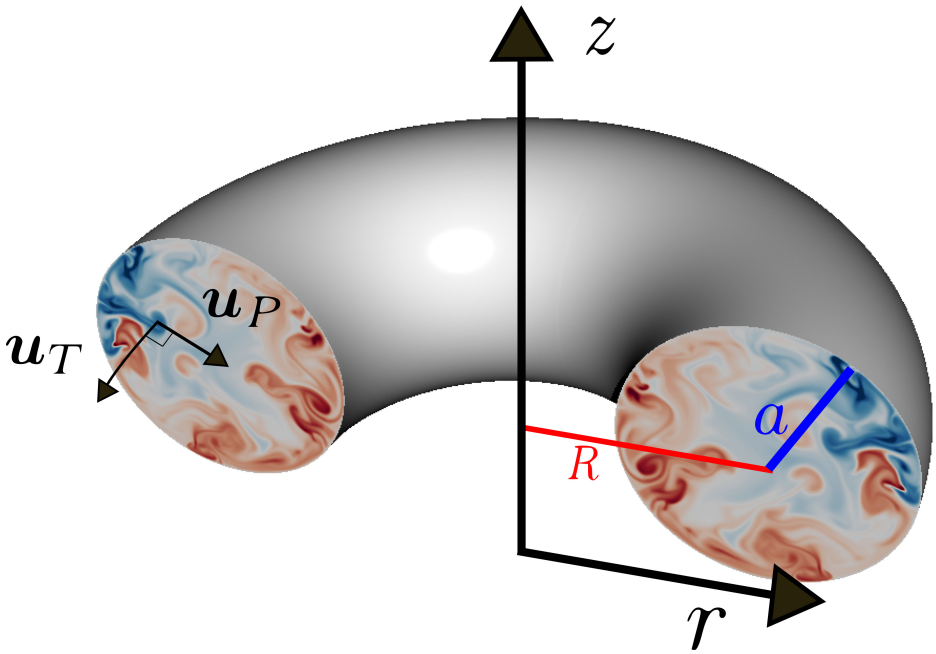

Figure 6.1: Tokamaks are torus-shaped fusion reactors where the plasma is confined by a magnetic field. The toroidal component of the magnetic field is dominant in realistic reactors. In the simplified description considered here, we only consider this toroidal field and assume it strong enough to render the plasma-dynamics invariant along the toroidal direction. This reduces the dynamics to a two-dimensional system, with three velocity components: two components in the poloidal plane, $\boldsymbol{u}_P$ and one toroidal component u_T. In the present schematic we indicate the major and minor axes R and a, respectively. The color plot indicate the (toroidal) vorticity associated with the poloidal velocity field.

The main actor limiting the confinement in tokamaks is turbulence. The transport of heat and matter by turbulent fluctuations degrades the confinement quality in all existing tokamaks [98, 99]. The presence of some turbulence does seem inevitable given the enormous gradients of temperature and magnetic fields in the plasma edge, but limiting the intensity of this turbulence as much as possible in the reaction chamber is paramount. This explains the tremendous importance given to a transition between two turbulent states, observed first experimentally in the ASDEX experiment [100]. The transition from a, highly turbulent, low-confinement mode (or L-mode) to a, more quiescent, high confinement mode (H-mode), is observed to increase the confinement time considerably. Knowing how to trigger such a LH-transition, and keep a plasma in H-mode, can thus be essential for the design of a successful fusion-reactor.

The understanding of the LH-transition is however still incomplete. Different propositions of theoretical frameworks can be found in reviews on the subject [101, 102]. It is now well accepted that in H-mode, confinement is improved by the presence of shearing motion at the edge of the plasma [103, 104, 105] and that interaction with the walls of the plasma vessel might play a role in this dynamics [106]. Such shearing motion allows to decorrelate radially propagating structures by a mechanism called shear-sheltering in the fluid mechanics literature [107, 108]. In the tokamak community this insight has had a major impact [109], in particular since magnetized plasmas show the formation of zonal flows, radially-sheared poloidal flow structures, which contribute importantly to this shear-sheltering [110, 111, 112]. Even though the dominance of these zonal flows seems a well established feature of H-mode behavior, it does not explain why these structures are only present in H-mode.

Our study, on the contrary, attempts to reveal the underlying, fluid-mechanical, origin of the transition. We illustrate that the observations of typical LH-related phenomena such as zonal flows, transport barriers and self-organization can be a consequence of a well-defined, robust transition, from a nearly two-dimensional flow with three dominant flow components, to a purely two-dimensional flow.

Indeed, in addition to zonal flows, another established ingredient of the H-mode is its link with two-dimensional turbulence. It has been known since the works of Kraichnan [7, 26] that a fluid flow in two space dimensions has the tendency to self-organize into large-scale structures. Examples of such self-organization are cyclonic structures in the atmosphere, and controlled numerical and physical experiments have verified this tendency to self-organization [113, 40, 39]. The turbulence in plasmas seems to behave in a similar manner [114], i.e., the turbulence also tends to form large scale structures. The link between the formation of space-filling structures in two-dimensional flows and the H-mode was stressed in experiments [115]. However, this does not explain why these effects are limited to the H-mode. Clearly, the magnetic field is also present in the L-mode, so that the dynamics should not be far from two-dimensional.

To understand the fluid mechanical difference between the two modes, one needs recent insights from theoretical studies on axisymmetric turbulence, which we will now briefly review. We consider purely axisymmetric flows, where not only the average flow quantities, but also every fluctuation is exactly axisymmetric. In the absence of magnetic fields or other body-forces, in neutral fluids such a flow in the turbulent regime is difficult to establish. Therefore, in the fluid mechanics community, this type of flow has received interest only recently, mostly in order to extend ideas from statistical mechanics of two-dimensional flows to a case closer to three dimensions [44, 46, 47]. Since such a

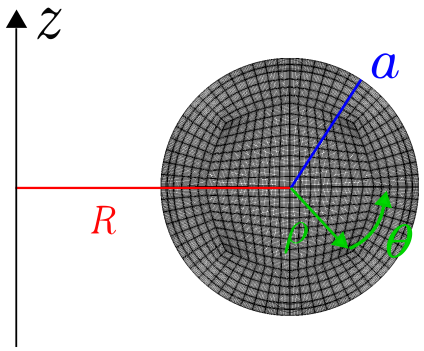

Figure 6.2: Spectral element mesh on the poloidal plane. The mesh consists of a central part and a boundary-adapted circular part. The major radius of the torus is R and the minor radius is denoted a.

turbulence is hard to reproduce experimentally, the assessment of theoretical ideas has been mainly achieved through direct numerical simulations of the axisymmetric Navier-Stokes equations [48, 116]. In a recent investigation [49] it was observed that a critical transition between two types of axisymmetric turbulence can be observed, where one of the flow states is characterized by typical two-dimensional behavior, i.e., self-organization of large velocity structures, whereas the other flow is two-dimensional, but involves three velocity components (see Fig. 6.3(a,b) for an illustration). Even though this latter state is essentially 2D, the large-scale flow structures are inherently unstable and tend to loose their energy to smaller scales, a feature reminiscent of 3D turbulence: this change in cascade direction is a major difference between 2D and axisymmetric 2D3C turbulence

Whereas neutral fluid turbulence is rarely in a close to axisymmetric state, this changes for the case of electrically conducting fluids, or plasmas. Indeed, the presence of a strong azimuthal magnetic field limits the variations in the direction of the field [20, 117, 118]. In a tokamak, a strong toroidal magnetic field is present, which renders the flow close to axisymmetric. In general the strength of this field is an order magnitude larger than the poloidal field (associated with a toroidal current) which we will neglect in our approach. The plasma in a tokamak is thereby close to a strictly axisymmetric state and can be described, at first order, by an axisymmetric fluid flow. We suggest that the transition which was discovered between two different axisymmetric turbulent states [49] should carry over to the dynamics of tokamaks. To illustrate this possibility, we have set-up a numerical experiment in toroidal geometry and we will show the confinement properties of the two axisymmetric flow states from a pure fluid mechanics perspective.

In the next section, we describe in detail the model we use to describe a turbulent plasma in toroidal geometry. In Sec. 6.3 we discuss the numerical details. In Sec. 6.4 we present the results of our numerical experiments. Finally in Sec. 6.5 we conclude.

6.2 Modeling and governing equations

The system we consider is a plasma in toroidal geometry. Since we assume axisymmetry, the dynamics can be described by a three-component dynamics in the poloidal plane. This simplifies the numerical experiments considerably. The poloidal domain on which

we focus is shown in Fig. 6.2, where we indicate the coordinate system. The major radius is R and the minor radius a. The cylindrical coordinate system is centered around the major (z-)axis of the torus. In this coordinate system the radial and vertical direction in the poloidal plane are defined r, z. We also define a local coordinate system, centered in the circular cross-section, with polar coordinates ρ, θ.

In the present section we will first introduce the fluid-description. Then we will focus on the forcing protocol, representing the plasma instabilities, and we will explain how we measure the confinement quality of the plasma.

6.2.1 A fluid mechanics modeling of tokamak plasmas

Plasmas can be described by a hierarchy of physical models [119]. The most precise, but thereby also least tractable, description is a kinetic approach involving all charged particles of the plasma and their nonlocal interactions [120]. The coarsest approach is probably a fluid approach, where the plasma is described using continuum mechanics [121]. In the present investigation it is this latter description which is adopted. We will omit all kinetic effects from our system. Furthermore we will assume the dynamics isothermal, solenoidal and we do not model the detailed interaction of the plasma with electrical currents and magnetic fields. The only influence of magnetic fields which is retained in the present system is the influence of a toroidal magnetic field, assumed to be strong enough to render the dynamics perfectly axisymmetric. Physically this corresponds to the fact that charged particles can freely move along magnetic field lines, whereas perpendicular motion is constrained by Coulomb-forces. This quasi-bidimensionalisation of the flow is well documented in magnetohydrodynamical turbulence [21, 122] and can even be exact when the magnetic Reynolds number is low enough [123].

In such an axisymmetric set-up, the dynamics are entirely described by the two velocity components in the poloidal plane $\boldsymbol{u}_P = (u_r, u_z)$, and one component u_T perpendicular to it (see Fig. 6.1). Such a system does not represent the instabilities associated with temperature, density and magnetic field gradients. It is in tokamaks these gradients which are at the origin of the turbulent fluctuations and these sources of instabilities are here modeled explicitly by appropriate external force terms.

We start by writing the axisymmetric Navier-Stokes equations.

$$\frac{\partial \boldsymbol{u}_P}{\partial t} + \boldsymbol{u}_P \cdot \nabla \boldsymbol{u}_P + \nabla P - \nu \Delta \boldsymbol{u}_P = \boldsymbol{\mathcal{N}}_P + \boldsymbol{F}_P \tag{6.1}$$

$$\frac{\partial u_T}{\partial t} + \boldsymbol{u}_P \cdot \nabla u_T - \nu \Delta u_T = \mathcal{N}_T + F_T. \tag{6.2}$$

The pressure P, in which we absorbed the constant density, ensures incompressibility through the condition

$$\frac{1}{r}\frac{\partial r u_r}{\partial r} + \frac{\partial u_z}{\partial z} = 0. \tag{6.3}$$

The last terms on the left hand side represent the viscous stresses, with ν the kinematic viscosity. In these terms the Δ indicates the axisymmetric vector-Laplacian in polar coordinates.

The left-hand-sides (LHSs) of Eq. (6.1) and Eq. (6.2), respectively, describe purely two-dimensional fluid motion, represented by the velocity vector-field $\boldsymbol{u}_P(\boldsymbol{x}, t)$ advecting the toroidal (out of plane) component of the velocity $u_T(\boldsymbol{x}, t)$. In a toroidal geometry the

curvature introduces the $\mathcal{N}$ terms, which couple the two fields. The curvature terms are

$$\boldsymbol{\mathcal{N}}_P = u_T^2/r\boldsymbol{e}_r \tag{6.4}$$

$$\mathcal{N}_T = -u_T u_r/r. \tag{6.5}$$

These terms are reminiscent of the vortex-stretching terms, essential in three-dimensional energy transfer, but absent in purely two-dimensional systems. All toroidal derivatives, $\partial/\partial\phi$ are zero since we consider the axisymmetric case. Physically this assumption is justified by the presence of a strong toroidal magnetic field.

The terms $\boldsymbol{F}_P$ and F_T are forcing terms which we will discuss now.

6.2.2 Forcing protocol

An important feature associated with a heated magnetized plasma is the presence of a number of instabilities leading to the generation of turbulent fluctuations. The forcing terms $\boldsymbol{F}_P$ and F_T are added to our system to reproduce the main features of sources of turbulent fluctuations in realistic plasmas (such as the interchange instability [119]), which are located at the tokamak edge, where the pressure, density and temperature gradients are large. The ensemble of these instabilities leading to turbulent fluctuations are in our approach modeled together by artificial force terms.

To generate the poloidal velocity fluctuations, we add a Rayleigh-Bénard type instability as follows. We compute the advection of a scalar-field by the poloidal velocity field,

$$\frac{\partial b}{\partial t} + \boldsymbol{u}_P \cdot \nabla b = \kappa \Delta b + S'. \tag{6.6}$$

The term S' represents a source of scalar in the edge region of the plasma. More precisely, the value S' is constant and is non-zero only in a shell near the boundary. The boundary condition at $r = a$ is the Dirichlet condition $b = 0$. Thereby, on average a negative radial gradient builds up between the radial location of the source term and the boundary. The poloidal forcing term is

$$\boldsymbol{F_P} = C_P b \boldsymbol{e}_\rho + \boldsymbol{F}_\beta. \tag{6.7}$$

The first term in this expression leads then to the Rayleigh-Bénard-type (linear) instability, through the coupling of the poloidal velocity (Eq. (6.1)) and the scalar (Eq. (6.6)).

The second term, $\boldsymbol{F}_\beta$ is a symmetry-breaking term, reminiscent of the anisotropic nature of a magnetized plasma. Indeed, in magnetized plasmas, a natural tendency to organize into concentric, toroidally invariant structures is observed related to the radial density gradients. The resulting zonal-flows are equivalent to the zonal-flows in rapidly rotating flows, such as the bands on Jupiter or the earth. To mimic this effect in the present set-up a body-force is added to the poloidal forcing in the spirit of the Hasegawa-Mima equation [124, 112],

$$\boldsymbol{F}_\beta = \beta' \rho \boldsymbol{e}_T \times \boldsymbol{u}_P. \tag{6.8}$$

This contribution to the poloidal force does therefore not inject energy in the system. As we will see below, the term $\boldsymbol{F}_\beta$ term is not essential to trigger the transition from 2D3C to 2D2C, but it leads to enhanced confinement if the transition to a 2D2C state is obtained. Simulations with and without this force will presented.

The toroidal fluctuations are also assumed to originate from a linear mechanism and are simulated by a linear forcing term. More precisely, for the toroidal forcing we use

$$F_T = C_T \left[u_T - \tau_\sigma^{-1} \frac{\langle u_T r \rangle}{R} \right] \tag{6.9}$$

and is applied on the same shell as the source term S'. The notation $\langle \cdot \rangle$ indicates a spatial average over the poloidal domain. The second term allows to avoid the build-up of toroidal angular momentum. Indeed, the spontaneous generation of angular momentum $\langle u_T r \rangle$ (or spin-up) in the system is of major interest [125], but we want to disentangle this effect from the investigation of the transition between 2D2C and 2C3C flows. The present form of the toroidal forcing term does therefore dominantly excite the toroidal velocity fluctuations avoiding the build-up of mean angular momentum.

6.2.3 Passive tracer to measure confinement

Eventually, we are interested in the confinement quality of the plasma. In practice, a good confinement in our system is associated with a small value of the radial turbulent diffusion. To measure turbulent diffusion, a passive tracer is injected continuously in the center of the domain, while homogeneous Dirichlet conditions are imposed on the wall. The quantity ξ, which follows the flow as a small amount of ink in a water-flow, does not affect the flow, but allows to measure the diffusion associated with the turbulent fluctuations. The governing equation is, as Eq. (6.13) an advection-diffusion equation,

$$\frac{\partial \xi}{\partial t} + \boldsymbol{u}_P \cdot \nabla \xi = \kappa \Delta \xi + f_\xi \tag{6.10}$$

where $f_\xi = C_\xi X(\rho_\xi - \rho)$, where X is the heaviside function, ρ_ξ the radius of the source and C_ξ a constant. When the turbulent fluctuations are strong, the diffusion allows efficient transport of the scalar, thus bad confinement, and the temperature in the center of the domain drops. Thereby the center-temperature ($\xi(\rho = 0)$) directly measures the confinement quality of the flow.

6.3 Normalization and Numerical set-up

Before performing the numerical simulations, it is convenient to introduce an appropriate normalization of the governing equations. This allows to identify the key parameters that will be varied. In this section we discuss the non-dimensionalization, the parameters used in our simulations and the numerical method,.

6.3.1 Dimensionless equations

In order to non-dimensionalize the equations, we choose as a typical timescale the inverse of the poloidal forcing rate $T^* = C_P^{-1}$. As lengthscale we use the minor radius $L^* = a$. This allows to normalize the equations using $\tilde{u} = uT^*/L^*$, $\tilde{\nabla} = L^*\nabla$, and analogous for $\Delta, P, b, \rho, \partial_t$. Removing after normalization all tildes, for notational ease, we obtain the

non-dimensional set of equations,

$$\frac{\partial \boldsymbol{u}_P}{\partial t} + \boldsymbol{u}_P \cdot \nabla \boldsymbol{u}_P + \nabla P - \frac{1}{Re}\Delta \boldsymbol{u}_P = \tag{6.11}$$

$$u_T^2/r\boldsymbol{e}_r + b\boldsymbol{e}_r + \beta\rho \boldsymbol{e}_T \times \boldsymbol{u}_P. \tag{6.12}$$

and

$$\frac{\partial b}{\partial t} + \boldsymbol{u}_P \cdot \nabla b = \frac{1}{Pe}\Delta b + S. \tag{6.13}$$

These two equations define the poloidal dynamics. For the toroidal velocity component we have in normalized form,

$$\frac{\partial u_T}{\partial t} + \boldsymbol{u}_P \cdot \nabla u_T - \frac{1}{Re}\Delta u_T = \\ -u_T u_r/r + \gamma \left[u_T - \tau_\sigma^{-1} \frac{\langle u_T r \rangle}{R} \right] \tag{6.14}$$

and for the passive scalar

$$\frac{\partial \xi}{\partial t} + \boldsymbol{u}_P \cdot \nabla \xi = \frac{1}{Pe}\Delta \xi + f_\xi. \tag{6.15}$$

In these equations we define,

$$Re = \frac{C_P a^2}{\nu}, \quad Pe = \frac{C_P a^2}{\kappa} \tag{6.16}$$

$$\gamma = \frac{C_T}{C_P}, \quad \beta = \frac{\beta' a}{C_P}, \quad S = \frac{S'}{a C_P^2}. \tag{6.17}$$

The parameter $\gamma = C_T/C_P$ measures the toroidal forcing strength compared to the poloidal forcing. This means that if γ is small, the instability mechanisms mainly drive the fluid flow in the poloidal plane. This ratio γ is the main control-parameter of our system.

6.3.2 Parameters

The major radius of the torus is $R = 2$ and the minor radius $a = 1$. The ratio $R/a = 2$ is of the order of magnitude of typical tokamaks. For instance the JET tokamak is characterized by an aspect ratio $R/a = 2.4$, ITER by a value close to three, while spheromaks have $R/a \approx 1$.

The Reynolds number is $Re = 5000$, which is a high enough value to ensure turbulent motion in our system. A change in its value does not qualitatively change the main results of the present investigation, as long as the flow remains turbulent. The Péclet number is chosen equal to the Reynolds number $Pe = Re$. The value of $C_P = 10$ is fixed and the forcing ratio γ is varied in the range $\gamma \in [0, 1.8]$. The value of $\beta = 0; 2; 8$. The relaxation time for the suppression of angular momentum is $\tau_\sigma = 0.25$.

For the active scalar b the injection shell near the boundary is defined by inner and outer radii $[\rho_1 : \rho_2] = [0.87a : 0.90a]$ and the value of the source term is $S = 0.8$. For the passive scalar ξ the source term is confined to a circular surface of radius $\rho_\xi = 0.1$ in the center of the poloidal plane with injection rate $C_\xi = 0.1$.

6.3.3 Numerical set-up

Direct numerical simulations are performed using the Nek5000 code [126], a robust and well-tested open source code, based on the spectral element method [61]. We solve the discretized Navier-Stokes equations and two scalar advection-diffusion equations. We impose simple non-slip boundary-conditions on the circular walls of the numerical domain for the velocity, and trivial Neumann-conditions for the scalars.

All simulations of the axisymmetric system are performed on a 2D grid which allows fast computations compared to a full three-dimensional description. The computational domain is a disk representing a poloidal cross section of the tokamak (see Fig. 6.2). The numerical grid consists of 640 spectral elements, with $n = 12$ the order of Lagrangian interpolant polynomials. The time-step is adaptative with a Courant–Friedrichs–Lewy condition CFL= 0.3. All results are reported during statistically steady states.

6.4 Numerical experiments of the fluid-mechanics of the LH transition

Now that the system is modeled and the numerical set-up is specified, we will here discuss the results of our simulations.

6.4.1 Characterization of the 2D3C-2D2C transition

The LH transition needs, from the fluid mechanics view-point, two ingredients. We will first focus on the first part, the transition from a 2D3C to a 2D2C flow. We illustrate this by changing the anisotropy of the forcing, $\gamma = C_T/C_P$. In Fig. 6.3(a) we show a time-series of the toroidal and poloidal kinetic energy for a representative case ($Re = 5000$, $\beta = 0$, $C_P = 10$).

For $t < 2850$ the flow is in the 2D3C regime, with a value $\gamma = 1.7$. During this time interval the order of magnitude of the two components of the kinetic energy is comparable with a somewhat more bursty behavior of the toroidal kinetic energy. At $t = 2850$ the strength of the toroidal forcing is instantaneously lowered resulting in $\gamma = 1.35$. This value of γ is apparently below the critical value for the transition and the flow becomes purely poloidal as is illustrated by the purely poloidal dynamics in Fig. 6.3(d). Indeed, the value of the toroidal energy drops to zero. The poloidal energy is not significantly affected. Decreasing the value of the toroidal force-coefficient can therefore trigger the 2D2C state.

In Fig. 6.3(b) we report the results of a parameter-sweep for the parameter $\gamma = C_T/C_P$ for a fixed value of C_P. All the data for the energy corresponds to temporal averages in a statistically steady state. We observe, when increasing γ, a critical transition from the 2D2C state (characterized by $E_T/E_P = 0$) to a 2D3C state, where the toroidal energy is non-zero. The influence of the parameter β will be discussed below.

Visualizations of the flow-field in the two regimes are shown in Fig. 6.3(c,d). The main feature is the non-zero value of the toroidal velocity fluctuations in Fig. 6.3(c). However, another outstanding feature is the tendency to self-organization. Indeed, as observed by inspecting the stream-function associated with the velocity pattern in the poloidal plane, in the 2D2C regime [Fig. 6.3(d)] a large scale self-organization is observed consisting of two counter-rotating toroidal vortex rings.

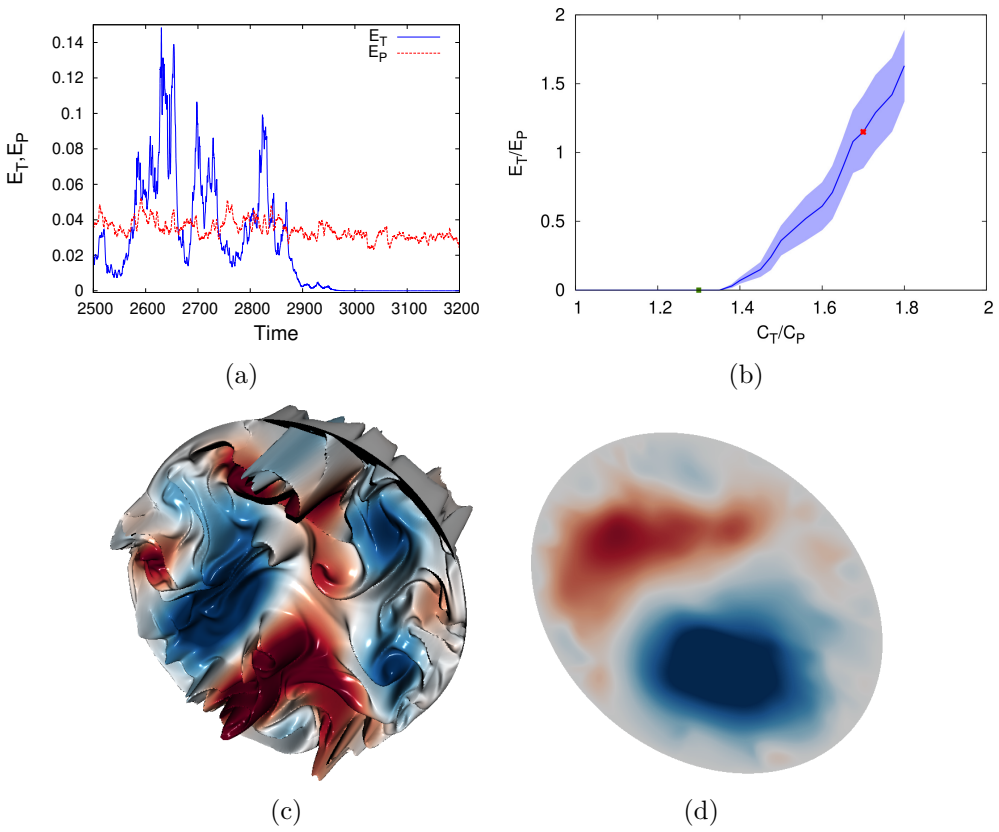

Figure 6.3: (a) Time-evolution of the volume-averaged poloidal energy E_P and toroidal energy E_T. For time $t < 2850$ the value $\gamma = 1.7$. For time $t \geq 2850$ the value the ratio of the forcing strength is lowered to $\gamma = 1.35$. The volume averaged energies illustrate a transition from a 2D3C (c) to a 2D2C state (d), respectively. The movement is in these visualizations plotted in the poloidal plane by colors indicating the strength of the stream-function. The toroidal velocity is illustrated by the out-of-plane morphology. (b)Influence of the forcing anisotropy on the ratio E_T/E_P for $\beta = 0$. The two values of the forcing anisotropy $\gamma = 1.35; 1.7$ associated with the timeseries in Fig. 6.3 are indicated by red and green symbols, respectively.

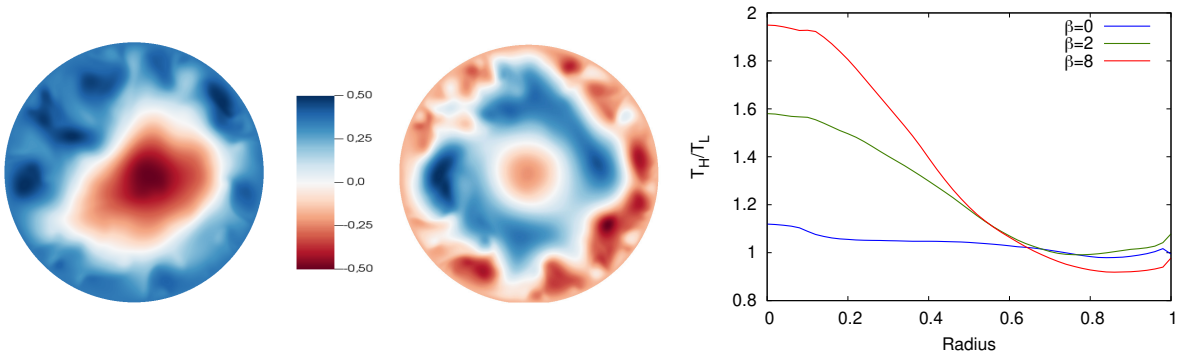

(a) (b)

Figure 6.4: (a) Stream-function patterns for 2D2C flows with two different values of the symmetry-breaking force ($\beta = 2$ and $\beta = 8$). (b) Ratio of the scalar profiles associated with a passive scalar injected in the center of the domain. In addition to values associated with (a) and (b) we also show the profile for $\beta = 0$. In this representation $T_H(\rho)$ is the scalar profile in the 2D2C regime and $T_L(\rho)$ the profile in the 2D3C regime. These profiles are obtained by averaging over time and over the poloidal angle θ.

6.4.2 Assesment of the confinement quality of the flow

Indeed, the double toroidal vortex rings observed in Fig. 6.3(d) are a generic feature of fluid simulations in toroidal geometry [127, 128]. Such a self-organization of the flow into two toroidal vortex rings does not seem beneficial for confinement in the center of the fusion-device, since the fluid or plasma between the large-scale structures will be rapidly expelled. We have tested this by measuring the turbulent diffusion of a passive scalar, injected in the center of the poloidal cross-section.

We solve the additional advection-diffusion equation (6.15), with a constant source term in the center of the poloidal cross-section. By measuring the average profile of the scalar, the confinement is quantified: a large value of the temperature in the center corresponds to good confinement and, conversely, a low core-temperature indicates bad confinement. Indeed, as illustrated in Fig. 6.4, for $\beta = 0$. the confinement is changed at most 10% between the two regimes.

Switching from a 2D3C state to a 2D2C flow is thus not enough to enhance the confinement properties of an axisymmetric toroidal fluid flow. The case of non-zero β, corresponding to the presence of an anisotropic force in the poloidal dynamics, will be discussed now.

6.4.3 The importance of symmetry breaking

Indeed, one additional effect is needed to enhance the confinement. This is the symmetry breaking, allowing to modify the double vortex-pattern, observed in Fig. 6.3(d) to a concentric pattern in the poloidal plane. In tokamak plasmas, this symmetry breaking is associated with the strong radial gradients of density, pressure and temperature. We show the effect of an anisotropic force-term in Fig. 6.4. The presence of this force allows to re-organize the large-scale structuring in a more concentric pattern, beneficial for confinement. In Fig. 6.5(b) we show the results of a parameter-scan for C_T/C_P for the values of $\beta = 0,\ 2,\ 8$. For all three values, a critical transition is observed as in

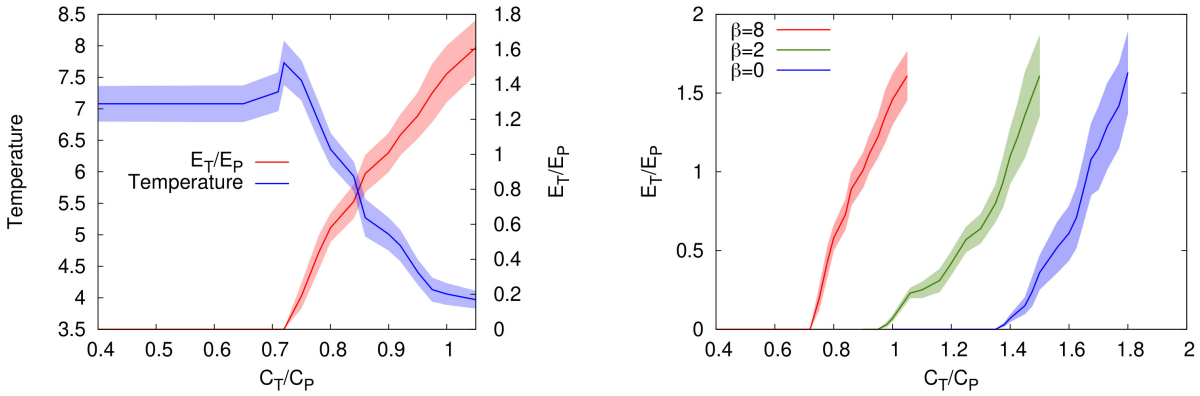

Figure 6.5: (a) Overview of the dependence of the system on the parameter C_T/C_P for fixed C_P and $\beta = 8$, where we also show how the confinement is enhanced by this transition, as measured by the temperature in the center of the toroidal domain. (b) Influence of the forcing anisotropy on the nature of the flow for three different values β, associated with the symmetry-breaking term.

Fig. 6.3(b) around a given ratio γ. The transition is therefore present for simulations with and without the symmetry breaking force, but the value of this critical ratio γ decreases as a function of β.

Most importantly, the resulting $2D2C$ flow, for the non-zero values of β considered here, confines the scalar significantly better. Indeed, in Fig. 6.5, it is observed that for a same constant scalar injection rate, the temperature in the center of the domain increases by a factor around two.

The transition of the flow is therefore triggered by the anisotropy of the forcing. This transition allows to enter a fully poloidal flow regime for small values of C_T/C_P. Such a purely poloidal flow has a tendency to self-organize. Indeed, in the absence of toroidal flow, the system can be described by purely two-dimensional hydrodynamics. The shape of the self-organized structures does depend on other factors, such as here the poloidal β-effect.

6.5 Towards enhanced confinement

From the results presented in the previous paragraphs, it can be concluded that a recently discovered critical transition in axisymmetric turbulence [49] survives in toroidal geometry, forced by instabilities near the toroidal boundaries. Indeed, this mimics in a crude way the dynamics of a tokamak, where a toroidally confined plasma develops instabilities at the boundaries where the pressure, density and temperature gradients are most important.

The present results illustrate that the LH-transition, in the present simplified fluid system, needs two ingredients. First, a dominance of the poloidal forcing over the toroidal forcing is required to be under a threshold for the critical $2D3C$ instability. Secondly, the self-organization resulting from the purely two-dimensional two-component-dynamics needs a symmetry-breaking mechanism, alllowing the system to organize into a concentric pattern in the poloidal plane (zonal flows). The main observations can then be summarized by Fig. 6.5(a), showing simultaneously the dependence of the energy ratio

and the confinement quality as a function of γ.

It is our newly obtained understanding that it is not the zonal flows which trigger the LH-transition: they are the consequence of the 2D2C nature of the H-mode. In the 2D3C L-mode we observe, a forward energy cascade will destroy the coherence of large-scale structures, preventing thereby the emergence of zonal flows. Once these zonal flows appear, they enhance the confinement.

The observations reported here are simple and robust. We have not added any more physics to the system than an axisymmetric fluid-description with linear force terms. We think that this identification of the essential ingredients of the transition is the most important insight that we have gained. The fact that the observations do not contain any precise plasma-instability, magnetic-field structure or kinetic effects perhaps explains why the LH-transition is so widely observed in the last four decades.

Note finally that while magnetohydrodynamical and kinetic effects are obviously fundamental in understanding the details of the LH transition [102], the objective here is to show that a minimal fluid dynamics model can reproduce its most important characteristics. Indeed now that we have pinpointed the essential physics, further understanding can be gained by transposing these ideas to a more realistic setting. For instance, in future experimental campaigns it can be tried to, either enhance poloidal energy injection, or to reduce toroidal fluctuations, leading to possibly unexplored magnetic fusion confinement protocols.

6.6 Conclusion of this chapter

The dynamics observed in the present chapter have possibly an important relevance for magnetically confined fusion research. In particular, in the context of the present thesis, we show that the flow in the torus changes its nature from 2D2C to 2D3C. This change should modify the invariants of the system and thereby the cascade properties.

Things that have not been observed are the generation of helical motion or mean angular motion. Indeed the latter effect is artificially removed through our damping on the toroidal velocity in Eq. (6.9). The influence of helicity on the dynamics seems however an important issue for further research. Indeed, this will be subject of the next chapter, where we investigate the transition from 3D3C turbulence to Cartesian 2D3C flows and where we will illustrate that this allows the spontaneous generation of helicity.

7 Spontaneous generation and reversal of helicity in anisotropic turbulence

Helicity[1] plays an important role in spectacular geophysical phenomena such as hurricanes or the generation of the terrestrial magnetic field. The present chapter shows how helicity can be created in a statistically homogeneous but anisotropic flow, driven by buoyancy. If the flow is close enough to a two-dimensional limit, spontaneous symmetry-breaking leads to the generation of mean helicity. In particular we explain these observations by identifying a simple linear mechanism, the relevance of which is illustrated by simulations of unstably stratified turbulence in a conducting fluid on which a magnetic field is imposed. Finally it is shown that the self-organized state displays dynamical reversals of the sign of the mean helicity.

7.1 On the origin and importance of helicity.

Helicity is associated with the cork-screw motion of fluid particles. As was discussed in Sec. 2.3.4, the mean helicity [9] is a topological invariant of the Euler equations and is defined as

$$H = \langle \boldsymbol{u} \cdot \boldsymbol{\omega} \rangle \tag{7.1}$$

where $\boldsymbol{u}$ is the velocity, $\boldsymbol{\omega} = \nabla \times \boldsymbol{u}$ the vorticity, and the brackets denote an ensemble average. Its value measures the knottedness of the vortex-lines in a fluid [10] and is zero in a mirror-symmetric flow.

The presence of helicity is presumably important for the generation of the Earth's magnetic field [129, 130, 131]. Furthermore, helicity is strong in hurricanes [132, 133, 134] and helical modes can be considered the building-blocks of the turbulent energy cascade of turbulent flows [135, 136, 137, 138, 139]. It has been known that the presence of helicity in isotropic turbulence does somewhat weaken the energy cascade [140, 141, 142]. These effects become more drastic and alter completely the energy cascade when strong helical forcing is used [73], a possibility anticipated some decades ago [143]. Also, in the presence of body-forces such as the buoyancy force or rotation, the influence of helicity can affect flow properties in a significant way [144, 145, 11]. Yet another interesting feature is that an inhomogeneous distribution of mean-helicity can induce a mean flow [146, 147].

Helicity can thus play an important role in turbulent flows. Both in laboratory experiments and numerical simulations aiming at the investigation of its effects, it is

[1]This chapter contains the results published in the publication, W. Agoua, B. Favier, A. Delache, A. Briard & W.J.T. Bos, Physical Review E 103.6 (2021): L061101. The text is slightly remodeled to integrate the results in the rest of this PhD manuscript.

usual to inject helicity in a flow either by boundary conditions or by adding a helical volume-force to the system. In the dynamo experiments of Riga and Karlsruhe [148, 149] for example, a helical mean flow was imposed through the shape of the container. In the Von Karman Sodium experiment [150], mean helicity is injected by counter-rotating impellers. In numerical simulations, helicity is often injected by adding an ABC flow containing mean-helicity [151, 152], or by starting from helical initial conditions [153, 154]. Using artificial forcing combined with strong rotation, helicity can be generated in a more spontaneous manner [155]. Apart from this last reference, in most of the above cited investigations, helicity is thus artificially imposed and its influence on the system is subsequently assessed. In natural flows, a known source of helicity is Ekman pumping [156, 157], or the interplay of inertial wave-packets with buoyancy [158, 159].

However, in the absence of statistical inhomogeneity or artificial forcing, is it possible to generate helicity? In the present investigation, we will show how helicity can be generated spontaneously by symmetry breaking of an initially non-helical system. It seems that the mechanism presented in this paper is thereby fairly generic and a good candidate to explain the genesis of helical motion in a number of geo- and astrophysical flows.

In the following we will derive a simple model, involving the linear interaction of skew-diffusion (a quantity defined below in Eq.(7.5)) and helicity. Analyzing this model, we will show that two ingredients are important for the current mechanism to operate: the presence of an unstable density stratification, and strong anisotropy.

7.2 Unstably stratified turbulence, skew-diffusion and helicity.

The governing equations of unstably stratified turbulence in the presence of a uniform density gradient in the z-direction are, in the Boussinesq approximation,

$$\partial_t \boldsymbol{u} + \boldsymbol{u}\cdot\nabla\boldsymbol{u} = -\nabla P + \nu\Delta\boldsymbol{u} + \theta\boldsymbol{e}_z + \boldsymbol{F}/\rho_0 \tag{7.2}$$

$$\partial_t \theta + \boldsymbol{u}\cdot\nabla\theta = \kappa\Delta\theta - N^2\boldsymbol{u}\cdot\boldsymbol{e}_z \tag{7.3}$$

$$\nabla\cdot\boldsymbol{u} = 0 \tag{7.4}$$

where P is pressure divided by the mean density ρ_0, ν the kinematic viscosity, $\theta = \rho g/\rho_0$ the buoyancy perturbation, with ρ the density fluctuation, g the acceleration due to gravity, κ the diffusivity, N the Brunt-Väisälä frequency and $\boldsymbol{F}$ an additional body force or damping term. Later on in this investigation we will apply a magnetic field to the system, in which case the term $\boldsymbol{F}$ is associated with the Lorentz force.

In statistically homogeneous, mirror-symmetric flow, in the presence of a constant mean density gradient, the large-scale dynamics of the system are characterized by the kinetic energy $\langle\boldsymbol{u}\cdot\boldsymbol{u}\rangle/2$, buoyancy variance $\langle\theta^2\rangle$ and buoyancy flux $\langle u_z\theta\rangle$. These three quantities measure the evolution of the flow and the interaction of the density and velocity fields. When mirror-symmetry is broken, which corresponds to the presence of mean helicity H, a new statistical correlation appears (zero in mirror-symmetric flow), the skew-diffusion

$$Q \equiv Q_z = \langle\theta\omega_z\rangle\,, \tag{7.5}$$

a quantity introduced by Moffatt [12], and somewhat forgotten since. However, in recent work this quantity was evaluated in isotropic helical turbulence on which a uniform passive scalar gradient is imposed [160].

An important insight, which motivates the present investigation, is that skew diffusion can be generated by a linear mechanism in the presence of helicity. From the evolution equations for $\boldsymbol{u}$ and θ [Eqs. (7.2)–(7.4)] we derive (in the absence of $\boldsymbol{F}$),

$$\frac{dQ}{dt} = N^2 H_z - D_Q - \epsilon_Q, \tag{7.6}$$

where the nonlinear damping and viscous terms are respectively defined by

$$D_Q = -\left\langle \theta \boldsymbol{\omega} \cdot \nabla u_z \right\rangle, \qquad \epsilon_Q = (\nu + \kappa) \left\langle \nabla\theta \cdot \nabla\omega_z \right\rangle. \tag{7.7}$$

We thus see that the production term (first term in the rhs of Eq. (7.6)) is directly proportional to the vertical component of the helicity $H_z = \langle u_z \omega_z \rangle$.

Analogously, when writing the equation for the helicity, it is observed that the skew-diffusion appears as a production term,

$$\frac{dH_z}{dt} = Q - D_H - \epsilon_H, \tag{7.8}$$

with

$$D_H = \left\langle \omega_z \boldsymbol{e}_z \cdot \nabla P \right\rangle, \qquad \epsilon_H = \nu \left\langle \nabla\boldsymbol{\omega} : \nabla\boldsymbol{u} \right\rangle. \tag{7.9}$$

The production term is not present if the scalar is passive. However, when back-reaction through buoyancy is present, the system is thus piloted by a linear production mechanism (first terms on the rhs of Eqs. (7.6) and (7.8)). The other terms in the system are nonlinear damping D_Q, D_H and visco-diffusive terms ϵ_Q, ϵ_H.

In the absence of the nonlinear damping, we can expect growth of H_z and Q if diffusive effects are small enough. The whole question is thus whether the nonlinear damping terms are strong enough to annihilate the combined linear production of helicity and skew-diffusion. There is an asymptotic limit where this should happen: from equations (7.6)-(7.8) it can be deduced that a system invariant along $\boldsymbol{e}_z$ (hereafter called 2D3C for two-dimensional three-components) will not be damped by the nonlinear terms.

Indeed, in the 2D3C limit, the gradient of the velocity and pressure field reduces to $\nabla = (\partial_x, \partial_y, 0)^T$ and consequently $\boldsymbol{\omega} = \omega_z \boldsymbol{e}_z$. Therefore both D_H and D_Q are zero since $\boldsymbol{e}_z \cdot \nabla$ vanishes. It seems therefore plausible that helicity (and skew-diffusion) will be generated in systems close to the 2D3C limit [1]. While the buoyancy force is anisotropic, it is known to sustain fully 3D turbulent states [153, 161, 162] and is therefore probably not sufficient on its own to reach the 2D3C limit. In the present investigation we will consider both the case $\boldsymbol{F} = 0$ and the case where this term is associated with an externally-imposed magnetic field, allowing the flow to approach the 2D3C regime.

7.3 Numerical set-up and parameters

Details on the 12 simulations documented in this investigation are given now. The three-dimensional Navier-Stokes equations and the buoyancy equation [Eqs. (7.2)–(7.4)] are integrated using pseudo-spectral Direct Numerical Simulations (DNS) in a 2π-periodic cube. The equations are integrated using a 3rd order Adams-Bashfort scheme and

[1] In this 2D3C limit, we note that the non-trivial relation between the contributions to the helicity $H_z = H_x + H_y$ can be derived using incompressibility.

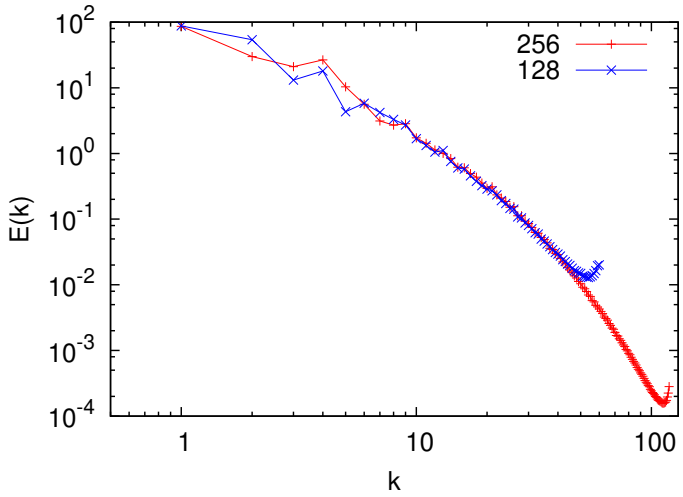

Figure 7.1: Kinetic energy spectrum $E(k)$ for a typical run ($G = 150$) at 128^3 and 256^3 resolution.

dealiasing is performed by phase-shifting. Initial conditions are statistically homogeneous, isotropic, with a peaked-initial spectrum around wavenumber $k = 1.5$. We start from initial conditions with a small amount of helicity (the normalized amount of initial helicity is of the order of a few percents). Any infinitesimal non-zero helicity is amplified by the present linear instability mechanism, and the nonlinearly saturated state is independent of the initial conditions. Simulation parameters are summarized in table 7.1. The integral-scale Reynolds number is defined as $R_L = u'L/\nu$, with $u' = \sqrt{2E/3}$, E being the kinetic energy and L the integral lengthscale, $L = \frac{3\pi}{4}\int k^{-1}E(k)dk/E$. The Taylor-scale Reynolds is given by, $R_\lambda = \sqrt{20E^2/(3\nu\epsilon)}$. Since the presence of the magnetic field renders the dynamics close to two-dimensional with three-components, the required resolution for a given Taylor-scale Reynolds number is much smaller than for an isotropic three-dimensional flow. Indeed, for a three-dimensional isotropic turbulent flow, a well-resolved simulation reaching a value $R_\lambda \approx 2300$ would require a spatial resolution of 12288^3 grid-points [163].

The typical Reynolds number based on the RMS velocity fluctuation and integral lengthscale is varying in the range $R_L \in [10^3, 10^4]$ for all runs with non-zero magnetic field. The initial value of the normalized helicity is small in all runs. All results are presented during a statistically steady state.

The simulations were performed at a resolution of 128^3 grid-points. This modest resolution allows to carry out long simulations which is useful to evaluate the long-time behavior of the system in order to compute converged statistics during the statistically steady state and to investigate reversals. However, consistency checks at a resolution of 256^3 grid-points confirm the results. We illustrate this in Fig. 7.1, where we plot energy spectra for the same physical parameters using both a resolution of 128^3 and 256^3 grid-points. The spectra roughly superpose all the way to the cut-off wavenumber of the 128^3 simulation. In particular, since we show that the helicity is piloted by the largest wavelengths (smallest wavenumbers), this relatively modest resolution seems sufficient to capture the physics of the system.

B_0	G	H_z	$\tilde{H}_z$	$\tilde{\Xi}_z$	R_L	R_λ	γ
0.0	0	0.0	0.0	0.0	265	81.53	0.64
0.170	48.1	4.8	0.017	0.31	1063	285	0.85
0.200	66.7	12.5	0.033	0.48	1242	339	0.89
0.300	150	57.4	0.043	0.64	2328	601	0.93
0.400	267	155	0.056	0.67	3404	852	0.94
0.500	417	302	0.066	0.71	4952	1235	0.95
0.555	513	354	0.068	0.72	5752	1451	0.95
0.600	600	453	0.071	0.74	6882	1696	0.96
0.650	704	517	0.073	0.75	7483	1832	0.96
0.700	817	662	0.076	0.75	8238	2038	0.96
0.760	963	710	0.077	0.78	9024	2270	0.97
0.800	1067	826	0.078	0.80	9647	2337	0.97

Table 7.1: Parameters and steady state values of several integral quantities. All simulations use $\nu = 0.0067$, $N = 0.6$, $\eta_0 = 0.001$, $\rho_0 = 1$, $\mu_0 = 1$.

7.4 Results.

We first consider a reference case of buoyancy-driven turbulence without imposed magnetic field [$\boldsymbol{F} = \boldsymbol{0}$ in Eq.(7.2)]. Iso-enstrophy surfaces are shown in Fig. 7.2(a) for the case $N = 0.6$ illustrating the presence of small-scale flow structures. Even though the mechanism which generates the flow is inherently anisotropic, no generation of mean helicity was observed, irrespective of the value of N, which was varied in the range $N \in [0.3, 4.5]$. These initial tests show that in statistically homogeneous buoyancy-driven turbulence without the presence of other effects, the strength of the nonlinear damping is too large to allow for a spontaneous generation of mean helicity.

In order to reduce the importance of the nonlinear damping terms we add an additional source of anisotropy to the simulations, in the form of an imposed vertical magnetic field ($\boldsymbol{F}$ in Eq. (7.2)). Indeed the Joule-damping associated with the Lorentz-force, rapidly tends to render the system invariant in the direction of the magnetic field if this latter is strong enough [20, 117]. Equivalently, we could have added rotation to the system, as in [145], which also allows to approach the 2D3C limit. We consider the quasi-static approximation where the Lorentz-force appears in closed form [117] in the Navier-Stokes equations, and the induction equation does not need to be solved. The Lorentz force acts then as a damping on the velocity fluctuations and its influence writes in this approximation, in Fourier representation,

$$\hat{\boldsymbol{F}} = -\frac{B_0^2}{\eta\mu_0}(\cos^2\phi)\hat{\boldsymbol{u}}, \tag{7.10}$$

with μ_0 the permeability, η the magnetic diffusivity and ϕ the angle between the wave-vector associated with $\hat{\boldsymbol{u}}$ and the direction of the magnetic field. This linear anisotropic damping term is of interest to gradually reach a 2D3C state. We fix the value $N = 0.6$ and vary the value of B_0. The control parameter is now the dimensionless number

$$G = \frac{B_0^2}{N\eta\rho_0\mu_0}, \tag{7.11}$$

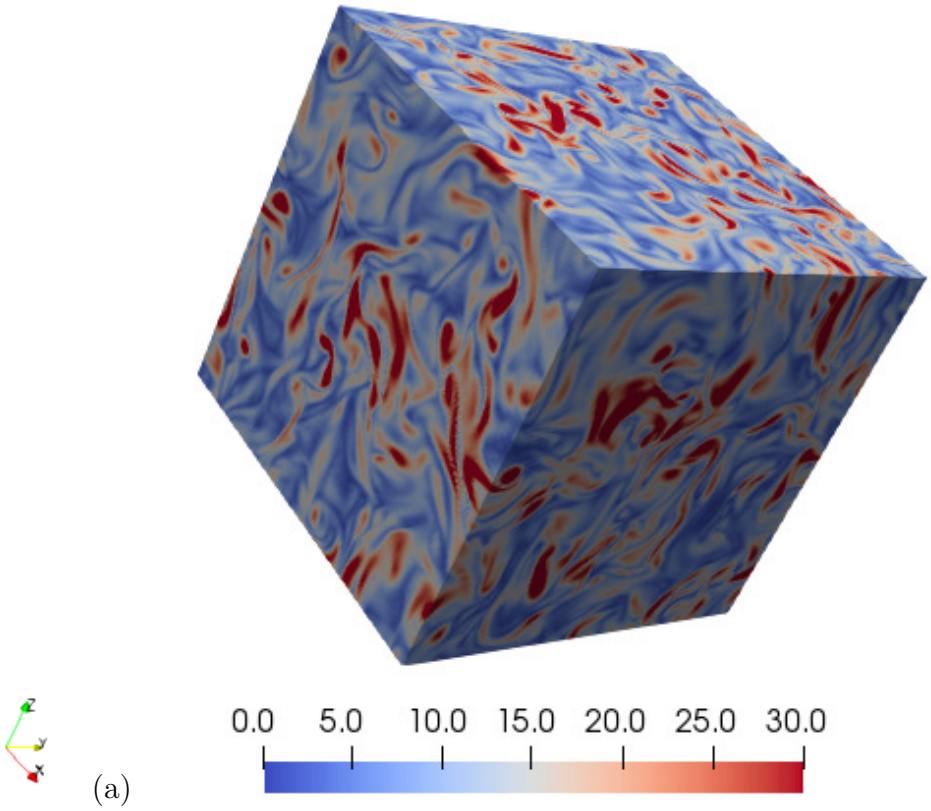

(a)

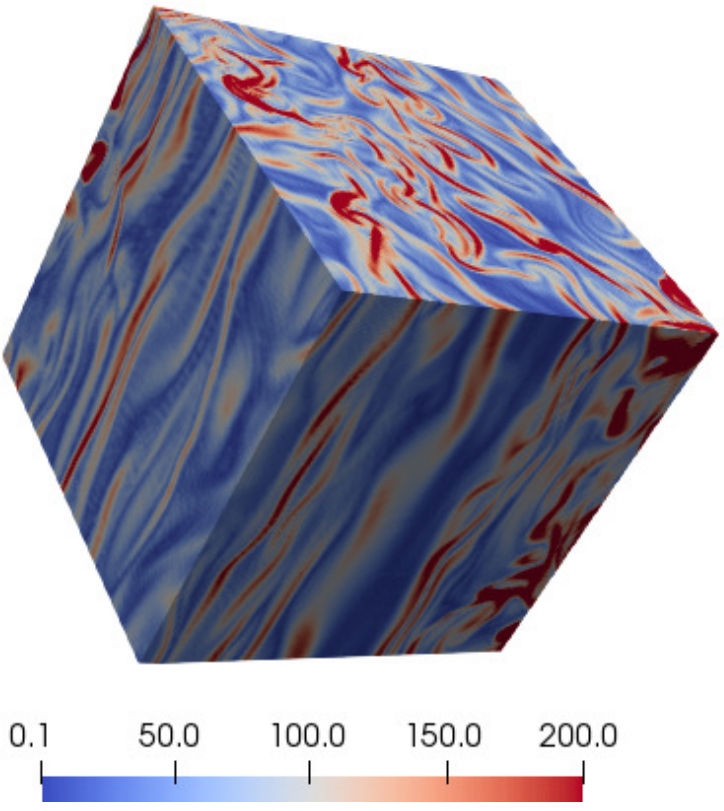

(b)

Figure 7.2: Enstrophy in unstably stratified turbulence ($N = 0.6$, $\nu = 0.0067$). (a) Without magnetic field [$G = 0$, see Eq. (7.11)]; (b) with magnetic field, $G = 300$.

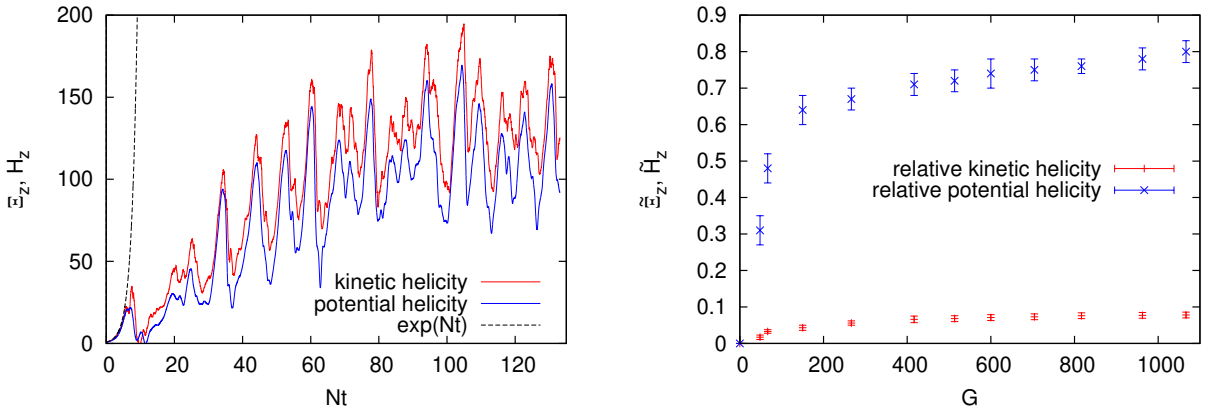

(a) (b)

Figure 7.3: (a) Time evolution of vertical kinetic helicity H_z and potential helicity Ξ_z for $N = 0.6$; $G = 300$. (b) Normalized helicities $\tilde{H}_z, \tilde{\Xi}_z$ as a function of G (for fixed $N = 0.6$).

which is varied in the range $G \in [0, 1100]$. For large values of G, the flow becomes almost invariant in the vertical direction (see Fig. 7.2(b)). We quantify this by measuring the vertically averaged kinetic energy compared to the total kinetic energy as in [164]:

$$\gamma = \frac{\langle E \rangle_z}{\langle E \rangle} \equiv \frac{\langle \| \frac{1}{L} \int_0^L \boldsymbol{u} dz \|^2 \rangle}{\langle \| \boldsymbol{u} \|^2 \rangle}, \tag{7.12}$$

which varies from $\gamma = 0.6$ for $G = 0$ to $\gamma = 0.95$ for $G = 1100$. This illustrates that the flow is close to the 2D3C limit for the largest values of G we considered.

We show in Figure 7.3(a), the results of a run where $G = 300$, illustrating that there is helicity generation when the magnetic field is strong enough. Below $G \approx 40$ the value of the mean-helicity could not easily be disentangled from random fluctuations.

The typical behavior for large values of G, as in Figure 7.3(a), is a linear phase ($Nt < 5$) for which the growth rate is exponential as predicted by the linearized Eqs. (7.6)-(7.8), followed by a saturation when damping terms can no longer be neglected. Eventually helicity fluctuates around a steady state ($Nt > 100$).

In the following we average helicity over the statistically steady state. Fig. 7.3(b) shows the relative vertical helicity

$$\tilde{H}_z = \langle u_z \omega_z \rangle \, / \left(\sqrt{\langle u_z^2 \rangle} \sqrt{\langle \omega_z^2 \rangle} \right). \tag{7.13}$$

This quantity does not exceed 0.1, even for the largest values of the magnetic field strength. We will now give an explanation for this observation.

An intuitive, structure-based interpretation of helicity generation in the present flow is that the helicity corresponds to segregated patches of vertical vorticity with a definite sign of vorticity while they rise, and the opposite sign when they descend. The anisotropic damping by the magnetic field leads to an invariance in the vertical direction of these patches. This would correspond, in a horizontal cut through the domain, to a dominant value of the vertical helicity of one sign. This is assessed in Fig. 7.4(a). In this visualization, both positive and negative small-scale helicity patches are observed. Furthermore, comparing the vertical velocity component Fig. 7.4(b) and vorticity Fig. 7.4(c), no clear spatial correlation is observed. It is thus not clear from these

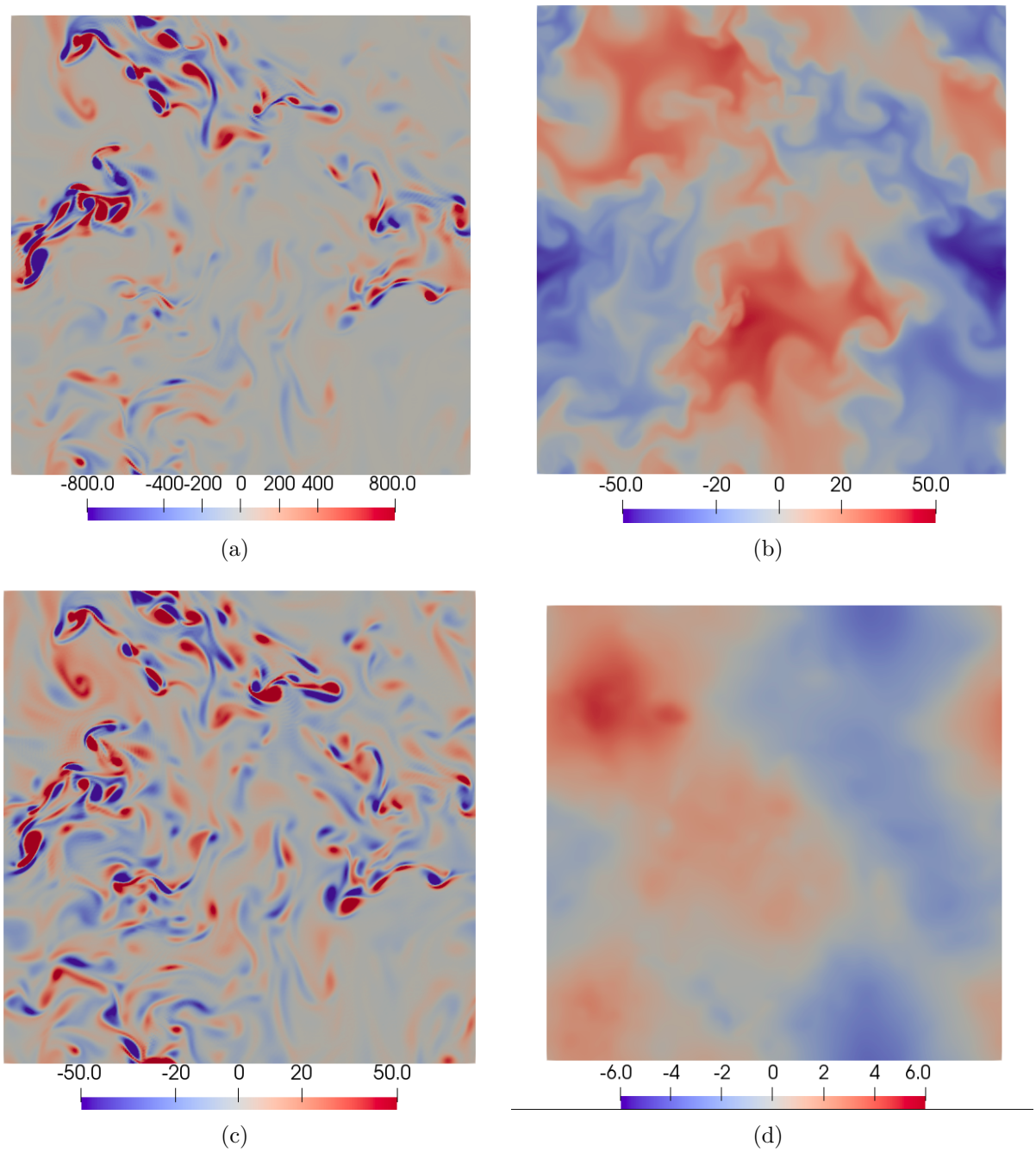

Figure 7.4: Horizontal cuts through the simulation domain for $G = 500$. The quantities are (a) vertical component of local helicity h_z, (b) vertical velocity u_z, (c) vertical vorticity ω_z, (d) Stream-function ψ_z associated with the velocity in the horizontal plane.

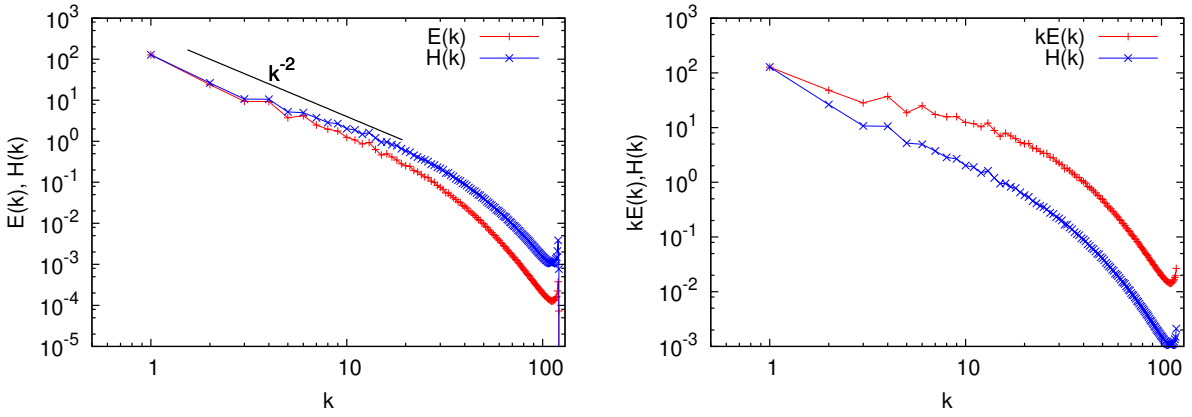

Figure 7.5: (a) Kinetic energy spectrum $E(k)$ and helicity spectrum $H(k)$ for $G = 0.3$. (b) Spectra $kE(k)$ and $H(k)$. This representation shows that the largest scales of the flow, where $|H(k)| = kE(k)$, are fully helical.

pictures which structures are responsible for the mean helicity. This visually confirms the small value of the relative helicity $\tilde{H}_z$.

It will be shown that the helicity is not contained in the small vortical structures visualized in Fig. 7.2(b) (or Fig. 7.4(c)), but in larger structures that are directly forced by the buoyancy instability driving the turbulence and which are associated with a two-dimensional condensate. With condensate we mean energy in the largest scales of a close to two-dimensional flow. Such a condensate results from blockage of the forward energy cascade for close-to-two-dimensional flow at large values of the magnetic field strength [165].

Insights into the multi-scale nature of turbulent phenomena are obtained by considering Fourier-spectra. We highlight in this section the spectral characterization of the statistically stationary flow for $G = 0.3$. In Fig. 7.5(a) we show the three dimensional kinetic energy spectrum $E(k)$ computed as an average over a duration of $t \approx 60/N$ during the statistically steady state of the run. It is observed that the spectrum displays an approximate k^{-2} scaling for intermediate wavenumbers. It is interesting to note here that this is quite similar to observations in high-resolution rotating stably stratified turbulence [145].

In Fig. 7.5(a) the helicity spectrum is also shown. This spectrum coincides at large scales and falls of somewhat less fast at larger wavenumbers. An interesting insight is obtained by considering the Cauchy-Schwarz inequality which relates the two spectra,

$$|H(k)| \leq kE(k). \tag{7.14}$$

In the limiting case where $|H(k)| = kE(k)$ the flow is *Beltramized*, which means that the vorticity is aligned with the velocity. In Fig. 7.5(b) we show again the two spectra, but with $E(k)$ mulitplied by k. We show that the two spectra do coincide for $k = 1$, which shows that the largest scales are corresponding to this Beltramized state where the normalized helicity is equal to unity. This spectral consideration thereby confirms that the largest scales of the flow are helical, as also suggested by the physical space investigation of the flow structures.

In order to highlight these large scale structures in physical space, we introduce the stream-function associated with the 2D motion, ψ_z such that $\omega_z = -\Delta_{x,y}\psi_z$, with $\Delta_{x,y}$

the horizontal Laplacian.

Indeed, both ω_z and ψ_z are associated with rotating velocity patterns, but the vorticity is in general associated with small scale structures whereas the stream-function characterizes larger-scale fluid motion. Visualizing ψ_z, in Fig. 7.4(d), it is observed that the large-scale rotating motion is fairly well correlated with the vertical velocity Fig. 7.4(b), which suggests that the mean-helicity is contained in the large-scale, two-dimensional condensate-like structure of the flow. Indeed, considering the vorticity, it is almost impossible to discern the helicity containing structures of the flow.

To substantiate these observations, we introduce a new quantity named potential helicity, (whereas the former helicity is designated by kinetic helicity) defined by

$$\Xi_z = \langle u_z \psi_z \rangle. \tag{7.15}$$

This quantity is shown to evolve in time very similar to the kinetic helicity, as shown in Fig. 7.3(a).

The relative potential helicity

$$\tilde{\Xi}_z = \langle u_z \psi_z \rangle \,/\, \left(\sqrt{u_z^2} \sqrt{\psi_z^2} \right) \tag{7.16}$$

is however observed to be significantly larger than the kinetic helicity (Fig. 7.3(b)). The fact that this quantity, is close to unity and that the non-normalized value almost coincides with the kinetic helicity shows that the helicity is contained in the largest structures, associated with wavenumber $k \approx 1$, which is confirmed by the spectra shown in Fig. 7.5.

Note that in a different limit, namely weak MHD turbulence, for the imbalanced case with strong correlation between the magnetic field and the velocity field, condensates of the residual energy were observed, associated with the breakdown of mirror symmetry at the largest scales [166].

7.5 Reversals of the helicity.

The presence of strong fluctuations could possibly allow for the reversal of the sign of the helicity. Indeed, both signs of the helicity are equally probable and it is natural to wonder whether the system can spontaneously reverse the sign of the helicity. We have investigated this possibility for small values of G, where the flow is not too close to its 2D3C limit. We show the results in Fig. 7.6 for $G = 80$. We indeed observe reversals. We have shown in the visualizations and the spectra that the helicity is governed by the largest scales of the flow. The reversals seem therefore related to the stability of the flow structures associated with these scales. A complete statistical analysis of the reversals and the underlying dynamics is beyond the scope of this chapter.

7.6 Conclusions of this chapter.

We presented a generic mechanism to generate helicity without the need for walls, viscous effects or statistical inhomogeneity. The generation of helicity is piloted by the interaction between skew-diffusion and helicity, represented by Eqs. (7.6) and (7.8). For the mechanism to be effective, the flow needs the presence of an unstable density gradient and a body-force which allows the system to attain a close-to-two-dimensional flow-state.

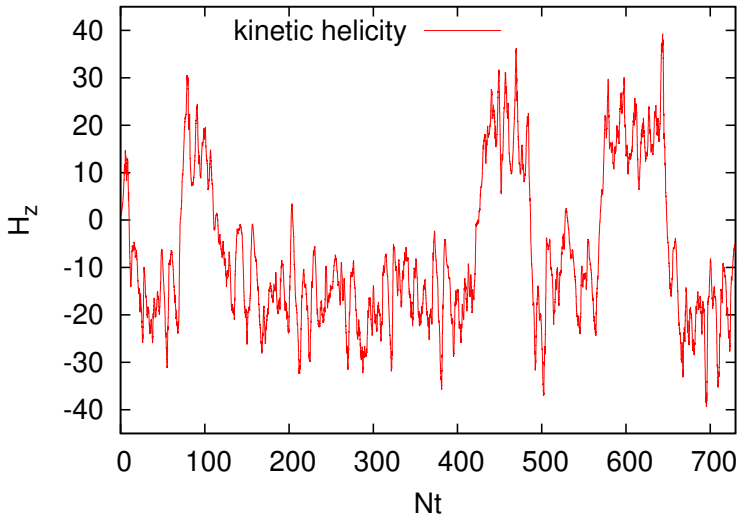

Figure 7.6: Reversals of the value of the mean helicity can be observed for certain values of the magnetic field (here $G = 80$).

The helicity is contained in condensate-like large-scale structures, associated with wavenumber $k = 1$, which are better assessed using the stream-function associated with the horizontal motion than using the vorticity.

The spontaneous nature of the helicity-generation and the random reversals invite to speculate on the relevance of the present observations for planetary dynamos and hurricane-genesis. Considering the combination of unstable stratification with other effects such as system rotation seems a logical direction to further explore the present class of symmetry breaking and its possible geophysical relevance.

Retrospective. This last chapter of the PhD manuscript reports on the first investigation carried out during this PhD project. After the results we obtained after publication of these results [167], such as the those reported in Chap. 4, it seems that the observed results in the present chapter can be understood by the fact that in the 2D3C limit, to which this flow transcends for strong magnetic field strength contains an invariant which has tendency to accumulate at the largest scales of the system. This effect was illustrated in the truncated 2D3C Euler system, illustrated in Fig. 4.9 where the $k = 1$ mode was shown to represent the effect of mean-helicity. The fact that the helicity is here also contained in a 'Beltramized' $k = 1$ mode does not seem a coincidence and illustrates how simple arguments using statistical mechanics can give insights into complex dynamics.

Conclusions and Perspectives of this Thesis

Conclusions

This thesis treated the subject of two-dimensional three-component turbulent flows. The most interesting observations are perhaps found when a realistic flow approaches this limit, either from the strictly 2D2C side, or starting from fully three-dimensional turbulence.

We will not repeat here all the observations of the ensemble of investigations of this thesis, since partial conclusions can be found at the end of each results chapter. What we think is interesting, is that combining theoretical ideas and simplified systems, specific physical phenomena could be identified which do not only exist in truncated inviscid systems, but which also have their application in realistic flows.

The three applications to more applied systems are

1. The influence of the vorticity-scalar correlation on mixing. In particular by singling out that it is an inviscid invariant which determines the decay of scalar variance, we can understand why mixing is so drastically affected by the initial vorticity-scalar correlation.

2. The influence of the 2D2C to 2D3C transition on the self-organization properties of turbulence, an effect which survives in the presence of toroidal solid boundaries, and which thereby has its possible application to research on magnetically confined nuclear fusion.

3. The generation of helicity in unstably stratified turbulence. Indeed, when linear energy input (here by buoyancy) is combined with a body force which renders the dynamics strongly anisotropic, the large-scale helicity, also observed in truncated equilibrium states, can emerge spontaneously.

Perspectives

We have in this thesis obtained these results combining ideas from equilibrium statistical mechanics and numerical simulations. The thereby obtained insights have also raised an important amount of questions, which we will discuss now.

Skew diffusion in 2D3C turbulence. The correlation between vorticity and scalar seems to play a very important role in the initial conditions of scalar mixing problems. We observed that this quantity persisted, for the Euler system, in the $k = 1$ mode. What we

do not know is whether this quantity, if it is injected at large wavenumbers, is transferred to smaller wavenumbers. In other words: is there an inverse cascade of skew diffusion?

Turbulence with curvature. In Chapter 5 we left several open ends. Indeed, there are theoretical and physical questions. What we mean by theoretical is that it would be interesting to show in the Galerkin-truncated axisymmetric system, how energy conservation is violated.

Furthermore, we would like to know how this can be fixed. Secondly, it would be of interest to investigate whether the influence of curvature can become more important if the toroidal injection scale is of the order of magnitude of the major radius R. Indeed, in the present set-up we needed cubic damping to prevent the toroidal energy from growing without bound. In previous studies [49] this extra damping was not needed and the curvature allowed to damp the system sufficiently by coupling the toroidal and poloidal dynamics.

The other invariants of the axisymmetric turbulence, angular momentum and generalized helicity have not been investigated in the present investigation. This is an interesting direction for further study.

Transition and confinement in toroidal geometry. Specifically this chapter opens an important number of perspectives. Since tokamaks and other fusion devices such as the RFP and stellarator have been studied extensively, it is more than interesting to put the present results in the context of fusion-plasma research. For instance: what are the underlying instabilities in a tokamak plasma. Are they of linear nature, is the anisotropy of existing instabilities somehow characterizable by a quantity like C_T/C_P, possibly by identifying the linear growth rate and the direction of instabilities in the tokamak edge. Is it possible to inject more poloidal movement to calm the tokamak turbulence, pushing it towards a 2D2C state? Also, the preliminary results in appendix B show that helicity might play an important role in the axisymmetric system. Is this also the case in more complex, toroidal geometry?

Reversals of helicity. In the end of Chap. 7 we showed that helicity can spontaneously flip from one sign to another.We don't think that there is a direct correlation with the inversion of the Earth's magnetic field. Firstly, because the characteristic times are different, and secondly, because the alpha effect is not the only phenomenon responsible for generating the magnetic field. However, this helicity inversion, coupled with other mechanisms, could contribute to the weakening of the Earth's magnetic field that precedes its reversal.

Altogether, it seems that this thesis is not the final contribution in the investigation of two-dimensional three-component turbulent flows.

A Appendix: A kitchen recipe to compute equilibrium energy spectra

This section shows how to compute equilibrium energy spectra once the invariants of a system are known. We specify the results for two-dimensional incompressible flow. Details and justifications can be found in [168, 90]. In particular, the second reference, Simon Thalabard's PhD manuscript gives a detailed procedure, which is definitely more rigorous than the present "kitchen recipe".

A.1 The general case

The derivation of Kraichnan's equilibrium distribution is as follows. We determine the invariants of the system, and we decompose them on the number of coordinates n, $G_{n1}, G_{n2}, ...$ Their sum will allow to define a constant of motion,

$$S_n = \alpha_1 G_{n1} + \alpha_2 G_{n2} + ... \tag{A.1}$$

The single mode partition function is then given by

$$Z_n = \int_{V_n} \exp[-S_n] dy_{1n} dy_{2n} ..., \tag{A.2}$$

where V_n is the phase-space containing all possible states y_{in}. In general this integral can be computed exactly. The average equilibrium modal distribution of quantity G_{np} is then directly obtained from this integrand using the relation

$$\langle G_{np} \rangle = -\frac{1}{Z_n} \frac{dZ_n}{d\alpha_p}, \tag{A.3}$$

which is the same as

$$\langle G_{np} \rangle = -\frac{d \ln [Z_n]}{d\alpha_p}. \tag{A.4}$$

This method, simplifies the calculation once the Gaussian integrals are worked out. These integrals are rather tedious to calculate analytically, but symbolic math software such as maple allows to compute the Gaussian integrals rather rapidly.

A.2 Energy and enstrophy in 2D turbulence

We consider a two-dimensional incompressible turbulent flow. We will first define the modal decomposition of the velocity field.

In two-dimensions, since incompressibility constrains the velocity to be perpendicular to the wavevector, only one free velocity-direction exists in the k_x, k_y plane, $\boldsymbol{e}_w = \boldsymbol{e}_k \times \boldsymbol{e}_z$. With $\boldsymbol{e}_z, \boldsymbol{e}_k$ unit-vectors in the vertical direction and parallel to the wave-vector, respectively. The velocity $\boldsymbol{u}(\boldsymbol{k}) = \tilde{u}(\boldsymbol{k})\boldsymbol{e}_w$ is a complex quantity, so that two independent real coefficients describe the velocity vector.

$$\boldsymbol{u}(\boldsymbol{k}) = \tilde{u}(\boldsymbol{k})\boldsymbol{e}_w = y_1(\boldsymbol{k})\boldsymbol{e}_w + iy_2(\boldsymbol{k})\boldsymbol{e}_w. \tag{A.5}$$

The energy is given by

$$E(\boldsymbol{k}) = \frac{1}{2}\langle \boldsymbol{u}(\boldsymbol{k}) \cdot \boldsymbol{u}(\boldsymbol{k})^* \rangle = \frac{1}{2}\langle y_1^2(\boldsymbol{k}) + y_2^2(\boldsymbol{k}) \rangle. \tag{A.6}$$

The vorticity is the curl of the velocity,

$$\boldsymbol{\omega}(\boldsymbol{k}) = i\boldsymbol{k} \times \boldsymbol{e}_w \tilde{u}(\boldsymbol{k}). \tag{A.7}$$

We have

$$\begin{aligned} \boldsymbol{k} \times \boldsymbol{e}_w &= \epsilon_{ijm} k_j \epsilon_{mab} k^{-1} k_a \delta_{b3} && \text{(A.8)} \\ &= (\delta_{ia}\delta_{jb} - \delta_{ib}\delta_{ja}) k^{-1} k_j k_a \delta_{b3} && \text{(A.9)} \\ &= k^{-1} k_3 k_i - k\delta_{i3} && \text{(A.10)} \end{aligned}$$

So that

$$\boldsymbol{\omega}(\boldsymbol{k}) = i(k^{-1}k_3 k_i - k\delta_{i3})\tilde{u}(\boldsymbol{k}). \tag{A.11}$$

Since $k_3 = 0$ (no variations in the vertical direction),

$$\boldsymbol{\omega}(\boldsymbol{k}) = -ik\tilde{u}(\boldsymbol{k})\boldsymbol{e}_z = \omega(\boldsymbol{k})\boldsymbol{e}_z. \tag{A.12}$$

The enstrophy is then

$$\begin{aligned} W(\boldsymbol{k}) &= \frac{1}{2}\langle \omega(\boldsymbol{k})\omega(\boldsymbol{k})^* \rangle && \text{(A.13)} \\ &= \frac{1}{2}k^2 \langle \tilde{u}(\boldsymbol{k})\tilde{u}(-\boldsymbol{k}). \rangle && \text{(A.14)} \\ &= k^2 E(\boldsymbol{k}). && \text{(A.15)} \\ & && \text{(A.16)} \end{aligned}$$

A.3 Advection of the two-dimensional passive scalar

We consider that the flow advects a scalar θ. The scalar is also described by its real and imaginary parts,

$$\theta(\boldsymbol{k}) = y_3(\boldsymbol{k}) + iy_4(\boldsymbol{k}). \tag{A.17}$$

The scalar "energy" is given by

$$\begin{aligned} C(\boldsymbol{k}) &= \frac{1}{2}\langle \theta(\boldsymbol{k})\theta(-\boldsymbol{k}) \rangle && \text{(A.18)} \\ &= \frac{1}{2}\langle y_3^2(\boldsymbol{k}) + y_4^2(\boldsymbol{k}) \rangle. && \text{(A.19)} \end{aligned}$$

The vorticity-scalar correlation, $\langle\theta\omega\rangle$ is an additional invariant of the system. Since this is not a quadratic quantity, one should be careful with the Fourier-correlation $\langle\omega(\boldsymbol{k})\theta(\boldsymbol{k})^*\rangle$, since it contains real and imaginary parts. The real part corresponds to the physical space correlation.

$$\begin{aligned} Q(\boldsymbol{k}) &= \Re\left[\langle\omega(\boldsymbol{k})\theta(\boldsymbol{k})^*\rangle\right] && \text{(A.20)}\\ &= \Re\left[\langle -ik\tilde{u}(\boldsymbol{k})\theta(\boldsymbol{k})^*\rangle\right] && \text{(A.21)}\\ &= \Re\left[\langle -ik(y_1(\boldsymbol{k})+iy_2(\boldsymbol{k}))(y_3(\boldsymbol{k})-iy_4(\boldsymbol{k}))\rangle\right] && \text{(A.22)}\\ &= k\langle y_2(\boldsymbol{k})y_3(\boldsymbol{k})-y_1(\boldsymbol{k})y_4(\boldsymbol{k})\rangle. && \text{(A.23)} \end{aligned}$$

We have expressed our 4 invariants as a function of the $y_i(\boldsymbol{k})$. We can now follow the kitchen recipe.

A.4 Statistical mechanics predictions of the spectra

The generalized phase-space coordinates are thus $y_i(\boldsymbol{k})$ with $i = 1..4$. For every $\boldsymbol{k}$, we have four corresponding coordinates. We will call $y_i(\boldsymbol{k}) \equiv y_{in}$. The conserved quantities are

$$\begin{aligned} E &= \sum_n \langle E_n\rangle, && \text{(A.24)}\\ W &= \sum_n \langle W_n\rangle, && \text{(A.25)}\\ C &= \sum_n \langle C_n\rangle, && \text{(A.26)}\\ Q &= \sum_n \langle Q_n\rangle. && \text{(A.27)} \end{aligned}$$

We can therefore write for S_n,

$$S_n = \alpha E_n + \beta W_n + \gamma C_n + \delta Q_n \tag{A.28}$$

which can be written,

$$S_n = \frac{1}{2}(\alpha+\beta k^2)(y_{1n}^2+y_{2n}^2) + \frac{1}{2}\gamma(y_{3n}^2+y_{4n}^2) + k\delta(y_{2n}y_{3n}-y_{1n}y_{4n}) \tag{A.29}$$

The single-mode partition function is then

$$Z_n = \iiiint_{-\infty}^{\infty} \exp[-S_n]\mathrm{d}y_{1n}\mathrm{d}y_{2n}\mathrm{d}y_{3n}\mathrm{d}y_{4n}. \tag{A.30}$$

This Gaussian integral can be computed (tedious, but Maple is a great help ...) and its value is

$$Z_n = \frac{4\pi^2}{\beta\gamma k^2 - \delta^2 k^2 + \alpha\gamma}. \tag{A.31}$$

From this expression, one can derive the energy distribution,

$$\langle E_n\rangle = -\frac{d\ln[Z_n]}{d\alpha}, \tag{A.32}$$

yielding,

$$U(k) \equiv \langle E_n \rangle = \frac{1}{\alpha + \beta k^2 - \frac{\delta^2}{\gamma} k^2}. \tag{A.33}$$

This can be reformulated as

$$U(k) = \frac{1}{\alpha + \beta' k^2}. \tag{A.34}$$

where $\beta' = \beta - \delta^2/(\gamma)$. So we find the same distribution as for classic 2D turbulence, which should be so since the scalar is passive. For the scalar, we find,

$$C(k) \equiv \langle C_n \rangle = \frac{1}{\gamma} \frac{\alpha + \beta k^2}{\alpha + \beta k^2 - \frac{\delta^2}{\gamma} k^2} \tag{A.35}$$

$$= \frac{1}{\gamma} \frac{\alpha + \beta k^2}{\alpha + \beta' k^2}, \tag{A.36}$$

which shows that the scalar spectrum is modified compared to the spectrum in the absence of $\langle \omega\theta \rangle$, which is given by

$$C(k) = \frac{1}{\gamma}. \tag{A.37}$$

How strong this modification is, depends on the initial correlation. The maximum correlation is $\langle \omega\theta \rangle = \langle |\omega| \rangle \langle |\theta| \rangle$.

B Appendix B: helicity generation in axisymmetric turbulence

We present here results, which we have not completely explored. We therefore present them like observations, with some speculation about the underlying physics. We think it is interesting to report the observations in order to avoid the possibility to miss an important physical feature.

In these simulations, the general set-up is identical to those in Sec. 5.4. We have removed large-scale friction. For this case $L = 2\pi$ which is not large. We use $C_P = 20$, $c_\psi = 0$ and $c_3 = 10^{-6}$, we keep the other parameters identical to those in Sec. 5.4. For this set-up we found a critical forcing ratio for $C_T/C_P \approx 0.15$.

In general, in forced two-dimensional turbulence in the absence of large-scale damping, the kinetic energy accumulates until a condensate is formed. However, recent results on approximately the same set-up as the one in our investigation, show that linear-forcing combined with cubic damping leads to a (partial) suppression of the inverse kinetic energy cascade [96]. We suspect that the same effect is present here. This arrest of the inverse cascade is a topic of current research and might be related by the formation of coherent structures of the size of the forcing, which do not actively interact with the larger flow scales, which can be considered, for such flow, as uncorrelated noise. This explanation is purely speculative, however.

In Fig. B.1 we show results for $C_T/C_P = 0.2$. For short times, the value of the toroidal kinetic energy remains small, but does not decay as in Fig. 5.5(b). At longer times, around $t = 600$ the toroidal energy suddenly rises to a larger value and remains in this state for the rest of the simulated time. A hint of the origin of this sudden transition is the appearance of mean-helicity in this case. Defining the relative helicity by

$$H_{rel} = \frac{H}{2W^{1/2}E_T^{1/2}}, \tag{B.1}$$

it is observed in Fig. B.1(d) that after the transition around $t = 600$, the normalized helicity rises from small random fluctuations around zero to a plateau value, where the relative helicity exceeds 80% of its maximum value.

For another flow, where $C_T/C_P = 2.0$, a bursty behavior is observed where at sudden time-instants helicity takes non-neglible values. However, this seems to be a transient effect.

In Fig. B.2, we show visualizations of the flows, corresponding to two cases where helicity is strong. It is observed that the dynamics of vorticity, stream-function and toroidal velocity are for these cases all dominated by highly energetic, helical vortices of the size of the forcing-scale.

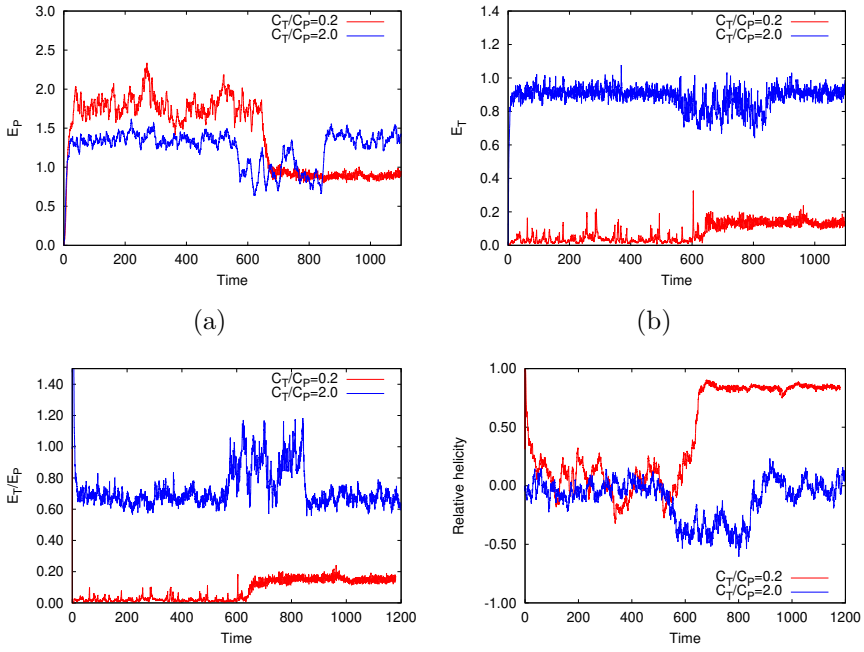

Figure B.1: Temporal behavior of two specific cases with a forcing anisotropy close to ($C_T/C_P = 0.2$), and not too far ($C_T/C_P = 2.0$) from the critical value separating 2D2C and 2D3C dynamics. (a) Poloidal energy (b) toroidal energy (c) ratio of the energies (d) normalized helicity.

Further research is needed to fully explore how strongly helical structures influence axisymmetric turbulence in general. In particular, are these structures only artefacts of the particular numerical set-up, or do they have a more general importance for research on 2D3D turbulence.

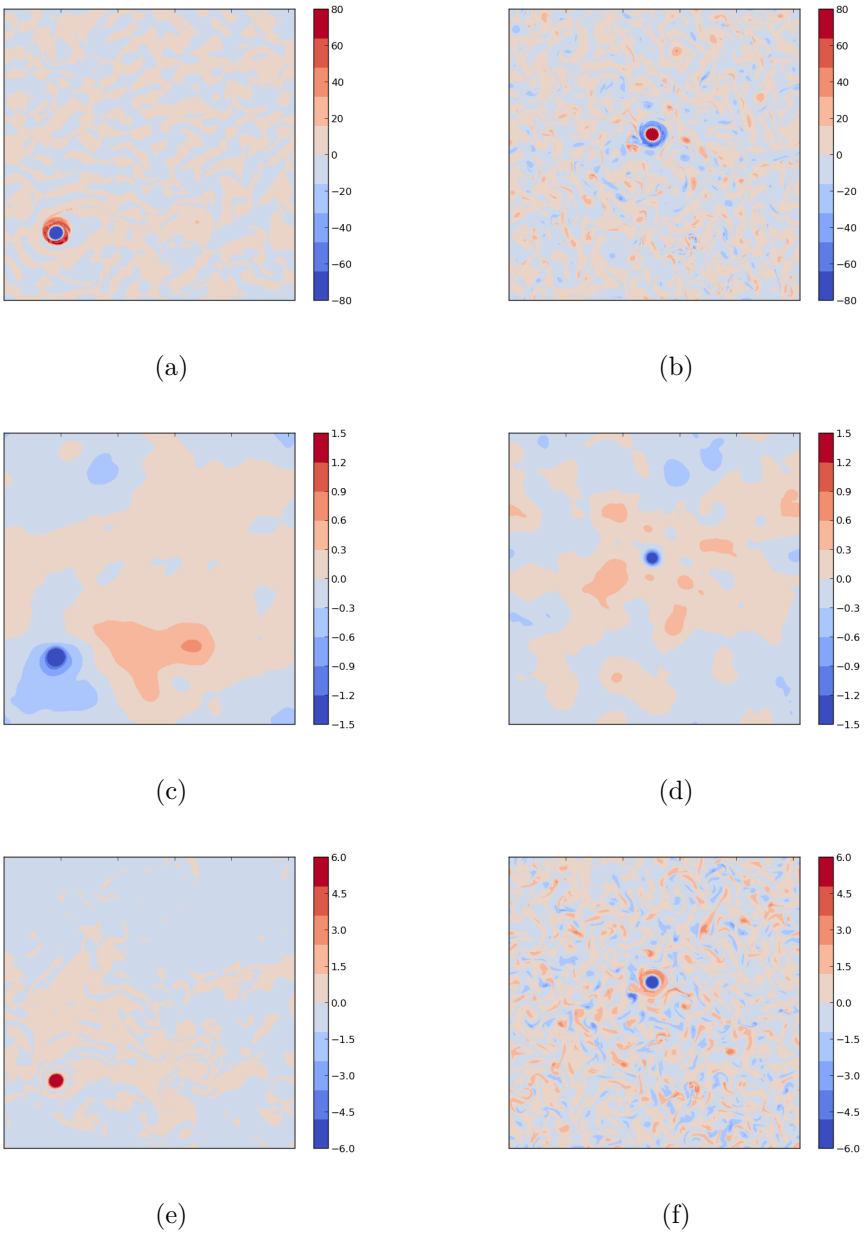

Figure B.2: Visualizations of the flow-field during the statistically steady state for the flows with $C_T/C_P = 0.2$ (left) and $C_T/C_P = 2$ (right). The displayed quantities are vorticity ω_θ (a,b), and toroidal velocity u_θ (c,d)

Bibliography

[1] Uriel Frisch. *Turbulence: the legacy of AN Kolmogorov*. Cambridge university press, 1995.

[2] Osborne Reynolds. An experimental investigation of the circumstances which determine whether the motion of water shall be direct or sinuous, and of the law of resistance in parallel channels. *Philosophical Transactions of the Royal society of London*, (174):935–982, 1883.

[3] LF. Richardson. *Weather prediction by numerical process*. University Press, 1922.

[4] Geoffrey Ingram Taylor. Statistical theory of turbulenc. *Proceedings of the Royal Society of London. Series A-Mathematical and Physical Sciences*, 151(873):421–444, 1935.

[5] D.C. Leslie. *Developments in the theory of turbulence*. Oxford University Press, 1973.

[6] P. Sagaut and C. Cambon. *Homogeneous Turbulence Dynamics*. Cambridge University Press, 2008.

[7] Robert H Kraichnan. Inertial ranges in two-dimensional turbulence. *The Physics of Fluids*, 10(7):1417–1423, 1967.

[8] Robert J Teed and Emmanuel Dormy. Solenoidal force balances in numerical dynamos. *Journal of Fluid Mechanics*, 964:A26, 2023.

[9] Jean Jacques Moreau. Constantes d'un îlot tourbillonnaire en fluide parfait barotrope. *Comptes rendus hebdomadaires des séances de l'Académie des sciences*, 252:2810–2812, 1961.

[10] Henry Keith Moffatt. The degree of knottedness of tangled vortex lines. *Journal of Fluid Mechanics*, 35(1):117–129, 1969.

[11] Keith Moffatt and Emmanuel Dormy. *Self-exciting fluid dynamos*, volume 59. Cambridge University Press, 2019.

[12] HK Moffatt. Transport effects associated with turbulence with particular attention to the influence of helicity. *Reports on Progress in Physics*, 46(5):621, 1983.

[13] AN. Kolmogorov. The Local Structure of Turbulence in Incompressible Viscous Fluid for Very Large Reynolds' Numbers. *Akademiia Nauk SSSR Doklady*, 30:301–305, January 1941.

[14] AN. Kolmogorov. A refinement of previous hypotheses concerning the local structure of turbulence in a viscous incompressible fluid at high reynolds number. *Journal of Fluid Mechanics*, 13(1):82–85, 1962.

[15] Peter Alan Davidson. *Turbulence in rotating, stratified and electrically conducting fluids*. Cambridge University Press, 2013.

[16] B Lehnert. The decay of magneto-turbulence in the presence of a magnetic field and coriolis force. *Quarterly of Applied Mathematics*, 12(4):321–341, 1955.

[17] CE Leith. Atmospheric predictability and two-dimensional turbulence. *Journal of the Atmospheric Sciences*, 28(2):145–161, 1971.

[18] G. J. Boer and T. G. Shepherd. Large-scale two-dimensional turbulence in the atmosphere. *Journal of Atmospheric Sciences*, 40(1):164 – 184, 1983.

[19] Erik Lindborg. Can the atmospheric kinetic energy spectrum be explained by two-dimensional turbulence? *Journal of Fluid Mechanics*, 388:259–288, 1999.

[20] HK Moffatt. On the suppression of turbulence by a uniform magnetic field. *Journal of fluid Mechanics*, 28(3):571–592, 1967.

[21] Alexandros Alexakis. Two-dimensional behavior of three-dimensional magnetohydrodynamic flow with a strong guiding field. *Physical Review E*, 84(5):056330, 2011.

[22] U Schumann. Numerical simulation of the transition from three-to two-dimensional turbulence under a uniform magnetic field. *Journal of fluid mechanics*, 74(1):31–58, 1976.

[23] David Montgomery and Leaf Turner. Anisotropic magnetohydrodynamic turbulence in a strong external magnetic field. *The Physics of Fluids*, 24(5):825–831, 05 1981.

[24] Barbara Bigot and Sébastien Galtier. Two-dimensional state in driven magnetohydrodynamic turbulence. *Phys. Rev. E*, 83:026405, Feb 2011.

[25] A Alemany, R Moreau, PL Sulem, and U Frisch. Influence of an external magnetic field on homogeneous mhd turbulence. *Journal de Mecanique*, 18(2):277–313, 1979.

[26] Robert H Kraichnan and David Montgomery. Two-dimensional turbulence. *Reports on Progress in Physics*, 43(5):547, 1980.

[27] Guido Boffetta and Robert E. Ecke. Two-dimensional turbulence. *Annual Review of Fluid Mechanics*, 44(1):427–451, 2012.

[28] Patrick Tabeling. Two-dimensional turbulence: a physicist approach. *Physics reports*, 362(1):1–62, 2002.

[29] Hamid Kellay and Walter I Goldburg. Two-dimensional turbulence: a review of some recent experiments. *Reports on Progress in Physics*, 65(5):845, apr 2002.

[30] Yoshimitsu Ogura. Energy transfer in a normally distributed and isotropic turbulent velocity field in two dimensions. *The Physics of Fluids*, 5(4):395–401, 1962.

[31] Ragnar Fjørtoft. On the changes in the spectral distribution of kinetic energy for twodimensional, nondivergent flow. *Tellus*, 5(3):225–230, 1953.

[32] Cecil E Leith. Diffusion approximation for two-dimensional turbulence. *The Physics of Fluids*, 11(3):671–672, 1968.

[33] George K Batchelor. Computation of the energy spectrum in homogeneous two-dimensional turbulence. *The Physics of Fluids*, 12(12):II–233, 1969.

[34] Douglas K Lilly. Numerical simulation of two-dimensional turbulence. *The Physics of Fluids*, 12(12):II–240, 1969.

[35] Douglas K Lilly. Numerical simulation of developing and decaying two-dimensional turbulence. *Journal of Fluid Mechanics*, 45(2):395–415, 1971.

[36] JR Herring, SA Orszag, RH Kraichnan, and DG Fox. Decay of two-dimensional homogeneous turbulence. *Journal of Fluid Mechanics*, 66(3):417–444, 1974.

[37] A. Pouquet, M. Lesieur, J. C. André, and C. Basdevant. Evolution of high reynolds number two-dimensional turbulence. *Journal of Fluid Mechanics*, 72(2):305–319, 1975.

[38] U Frisch and P-L Sulem. Numerical simulation of the inverse cascade in two-dimensional turbulence. *The Physics of fluids*, 27(8):1921–1923, 1984.

[39] Jérôme Paret and Patrick Tabeling. Experimental observation of the two-dimensional inverse energy cascade. *Physical review letters*, 79(21):4162, 1997.

[40] Joel Sommeria. Experimental study of the two-dimensional inverse energy cascade in a square box. *Journal of fluid mechanics*, 170:139–168, 1986.

[41] Robert H Kraichnan. Inertial-range transfer in two-and three-dimensional turbulence. *Journal of Fluid Mechanics*, 47(3):525–535, 1971.

[42] Sivaramakrishna Chandrasekhar. The theory of axisymmetric turbulence. *Philosophical Transactions of the Royal Society of London. Series A, Mathematical and Physical Sciences*, 242(855):557–577, 1950.

[43] GK Batchelor. The theory of axisymmetric turbulence. *Proceedings of the Royal Society of London. Series A. Mathematical and Physical Sciences*, 186(1007):480–502, 1946.

[44] Nicolas Leprovost, Bérengère Dubrulle, and P-H Chavanis. Dynamics and thermodynamics of axisymmetric flows: Theory. *Physical Review E*, 73(4):046308, 2006.

[45] Romain Monchaux, Florent Ravelet, Bérengère Dubrulle, Arnaud Chiffaudel, and François Daviaud. Properties of steady states in turbulent axisymmetric flows. *Physical review letters*, 96(12):124502, 2006.

[46] Aurore Naso, Romain Monchaux, Pierre-Henri Chavanis, and Bérengère Dubrulle. Statistical mechanics of beltrami flows in axisymmetric geometry: Theory reexamined. *Physical Review E*, 81(6):066318, 2010.

[47] Simon Thalabard, Bérengère Dubrulle, and Freddy Bouchet. Statistical mechanics of the 3d axisymmetric euler equations in a taylor–couette geometry. *Journal of Statistical Mechanics: Theory and Experiment*, 2014(1):P01005, 2014.

[48] Bo Qu, Wouter JT Bos, and Aurore Naso. Direct numerical simulation of axisymmetric turbulence. *Physical Review Fluids*, 2(9):094608, 2017.

[49] Zecong Qin, Hugues Faller, Bérengère Dubrulle, Aurore Naso, and Wouter JT Bos. Transition from non-swirling to swirling axisymmetric turbulence. *Physical Review Fluids*, 5(6):064602, 2020.

[50] U Frisch, M Lesieur, and PL Sulem. Crossover dimensions for fully developed turbulence. *Physical Review Letters*, 37(19):1312, 1976.

[51] A. Celani, S. Musacchio, and D. Vincenzi. Turbulence in more than two and less than three dimensions. *Phys. Rev. Lett.*, 104:184506, 2010.

[52] Adrian van Kan and Alexandros Alexakis. Condensates in thin-layer turbulence. *Journal of Fluid Mechanics*, 864:490–518, 2019.

[53] Stefano Musacchio and Guido Boffetta. Split energy cascade in turbulent thin fluid layers. *Physics of Fluids*, 29(11), 2017.

[54] Hua Xia, David Byrne, Gregory Falkovich, and Michael Shats. Upscale energy transfer in thick turbulent fluid layers. *Nature Physics*, 7(4):321–324, 2011.

[55] Alexandros Alexakis and Luca Biferale. Cascades and transitions in turbulent flows. *Physics Reports*, 2018.

[56] Zecong Qin, Aurore Naso, and Wouter JT Bos. Transition from axisymmetric to three-dimensional turbulence. *Journal of Turbulence*, 22(8):481–496, 2021.

[57] W Peter Jones and Brian Edward Launder. The prediction of laminarization with a two-equation model of turbulence. *International journal of heat and mass transfer*, 15(2):301–314, 1972.

[58] S. A. Orszag. Analytical theories of turbulence. *J. Fluid Mech.*, 41:363, 1970.

[59] Pablo D Mininni, Duane Rosenberg, Raghu Reddy, and Annick Pouquet. A hybrid mpi–openmp scheme for scalable parallel pseudospectral computations for fluid turbulence. *Parallel computing*, 37(6-7):316–326, 2011.

[60] A. Delache, C. Cambon, and F. Godeferd. Scale by scale anisotropy in freely decaying rotating turbulence. *Phys. Fluids*, 26(2):025104, 2014.

[61] Anthony T Patera. A spectral element method for fluid dynamics: laminar flow in a channel expansion. *Journal of computational Physics*, 54(3):468–488, 1984.

[62] Paul Fischer, James Lottes, and Henry Tufo. Nek5000. Technical report, Argonne National Lab.(ANL), Argonne, IL (United States), 2007.

[63] Hank Childs, Eric Brugger, Brad Whitlock, Jeremy Meredith, Sean Ahern, David Pugmire, Kathleen Biagas, Mark Miller, Cyrus Harrison, Gunther H. Weber, Hari Krishnan, Thomas Fogal, Allen Sanderson, Christoph Garth, E. Wes Bethel, David Camp, Oliver Rübel, Marc Durant, Jean M. Favre, and Paul Navrátil. Visit: An end-user tool for visualizing and analyzing very large data. In *High Performance Visualization–Enabling Extreme-Scale Scientific Insight*, pages 357–372. October 2012.

[64] Lars Onsager. Statistical hydrodynamics. *Il Nuovo Cimento (1943-1954)*, 6(Suppl 2):279–287, 1949.

[65] G. Joyce and D. Montgomery. Negative temperature states for the two-dimensional guiding center plasma. *J. Plasma Phys.*, 10:107, 1973.

[66] D.C. Montgomery and G. Joyce. Statistical mechanics of "negative temperature" states. *Phys. Fluids*, 17:1139, 1974.

[67] J. Miller. Statistical mechanics of Euler equations in two dimensions. *Phys. Rev. Lett.*, 65:2137–2140, 1990.

[68] R. Robert and J. Sommeria. Statistical equilibrium states for two-dimensional flows. *J. Fluid Mech.*, 229:291, 1991.

[69] G. L. Eyink and K. R Sreenivasan. Onsager and the theory of hydrodynamic turbulence. *Rev. Mod. Phys.*, 78(1):87, 2006.

[70] Robert H Kraichnan and David Montgomery. Two-dimensional turbulence. *Reports on Progress in Physics*, 43(5):547, 1980.

[71] F. Bouchet and A. Venaille. Statistical mechanics of two-dimensional and geophysical flows. *Physics Reports*, 515:227, 2012.

[72] T.D. Lee. On some statistical properties of hydrodynamical and magnetohydrodynamical fields. *Q. Appl. Math*, 10:69, 1952.

[73] Franck Plunian, Andrei Teimurazov, Rodion Stepanov, and Mahendra Kumar Verma. Inverse cascade of energy in helical turbulence. *Journal of Fluid Mechanics*, 895, 2020.

[74] Tong Wu and Wouter J.T. Bos. Statistical mechanics of the euler equations without vortex stretching. *Journal of Fluid Mechanics*, 929:A11, 2021.

[75] Douglas G Fox and Steven A Orszag. Inviscid dynamics of two-dimensional turbulence. *The Physics of Fluids*, 16(2):169–171, 1973.

[76] CE Seyler Jr, Yehuda Salu, David Montgomery, and Georg Knorr. Two-dimensional turbulence in inviscid fluids or guiding center plasmas. *The Physics of Fluids*, 18(7):803–813, 1975.

[77] Mahendra K Verma and Soumyadeep Chatterjee. Hydrodynamic entropy and emergence of order in two-dimensional euler turbulence. *Physical Review Fluids*, 7(11):114608, 2022.

[78] S Fox and PA Davidson. Integral invariants of two-dimensional and quasigeostrophic shallow-water turbulence. *Physics of Fluids*, 20(7), 2008.

[79] Greg Holloway and Stefan S Kristmannsson. Stirring and transport of tracer fields by geostrophic turbulence. *Journal of Fluid Mechanics*, 141:27–50, 1984.

[80] Marcel Lesieur and Jackson Herring. Diffusion of a passive scalar in two-dimensional turbulence. *Journal of Fluid Mechanics*, 161:77–95, 1985.

[81] Peter Bartello and Greg Holloway. Passive scalar transport in β-plane turbulence. *Journal of Fluid Mechanics*, 223:521–536, 1991.

[82] Tong Wu and Wouter J.T. Bos. Cascades and scaling in turbulence without vortex-stretching. *Submitted*, —, 2021.

[83] Peter B Weichman. Strong vorticity fluctuations and antiferromagnetic correlations in axisymmetric fluid equilibria. *Physical Review Fluids*, 4(5):054703, 2019.

[84] S Douady, Y Couder, and ME Brachet. Direct observation of the intermittency of intense vorticity filaments in turbulence. *Physical review letters*, 67(8):983, 1991.

[85] Kamran Mohseni. Statistical equilibrium theory for axisymmetric flows: Kelvin's variational principle and an explanation for the vortex ring pinch-off process. *Physics of Fluids*, 13(7):1924–1931, 2001.

[86] BE Launder and A Morse. Numerical prediction of axisymmetric free shear flows with a reynolds stress closure. In *Turbulent shear flows I*, pages 279–294. Springer, 1979.

[87] Bo Qu. *Numerical simulation of axisymmetric turbulence*. PhD thesis, Lyon, 2017.

[88] Zecong Qin. *Transitions in axisymmetric turbulence*. PhD thesis, Université de Lyon, 2019.

[89] Bo Qu, Aurore Naso, and Wouter JT Bos. Cascades of energy and helicity in axisymmetric turbulence. *Physical Review Fluids*, 3(1):014607, 2018.

[90] Simon Thalabard. *Contributions to the statistical mechanics of ideal two and a half dimensional flows*. PhD thesis, Université Paris Sud-Paris XI, 2013.

[91] Thomas S Lundgren. Linearly forced isotropic turbulence. *Center for Turbulence Research Annual Research Briefs 2003*, 2003.

[92] Wouter JT Bos, Faouzi Laadhari, and Wesley Agoua. Linearly forced isotropic turbulence at low reynolds numbers. *Physical Review E*, 102(3):033105, 2020.

[93] John Toner, Yuhai Tu, and Sriram Ramaswamy. Hydrodynamics and phases of flocks. *Annals of Physics*, 318(1):170–244, 2005.

[94] Henricus H Wensink, Jörn Dunkel, Sebastian Heidenreich, Knut Drescher, Raymond E Goldstein, Hartmut Löwen, and Julia M Yeomans. Meso-scale turbulence in living fluids. *Proceedings of the national academy of sciences*, 109(36):14308–14313, 2012.

[95] Martin James, Wouter JT Bos, and Michael Wilczek. Turbulence and turbulent pattern formation in a minimal model for active fluids. *Physical Review Fluids*, 3(6):061101, 2018.

[96] Adrian van Kan, Benjamin Favier, Keith Julien, and Edgar Knobloch. Spontaneous suppression of inverse energy cascade in instability-driven 2-d turbulence. *Journal of Fluid Mechanics*, 952:R4, 2022.

[97] J D Lawson. Some criteria for a power producing thermonuclear reactor. *Proceedings of the Physical Society. Section B*, 70(1):6–10, jan 1957.

[98] Paulett C Liewer. Measurements of microturbulence in tokamaks and comparisons with theories of turbulence and anomalous transport. *Nuclear Fusion*, 25(5):543, 1985.

[99] X Garbet, P Mantica, C Angioni, E Asp, Y Baranov, C Bourdelle, R Budny, F Crisanti, G Cordey, L Garzotti, et al. Physics of transport in tokamaks. *Plasma Physics and Controlled Fusion*, 46(12B):B557, 2004.

[100] F. Wagner, G. Becker, K. Behringer, D. Campbell, A. Eberhagen, W. Engelhardt, G. Fussmann, O. Gehre, J. Gernhardt, G. v. Gierke, G. Haas, M. Huang, F. Karger, M. Keilhacker, O. Klüber, M. Kornherr, K. Lackner, G. Lisitano, G. G. Lister, H. M. Mayer, D. Meisel, E. R. Müller, H. Murmann, H. Niedermeyer, W. Poschenrieder, H. Rapp, H. Röhr, F. Schneider, G. Siller, E. Speth, A. Stäbler, K. H. Steuer, G. Venus, O. Vollmer, and Z. Yü. Regime of improved confinement and high beta in neutral-beam-heated divertor discharges of the asdex tokamak. *Phys. Rev. Lett.*, 49:1408–1412, Nov 1982.

[101] Fritz Wagner. A quarter-century of h-mode studies. *Plasma Physics and Controlled Fusion*, 49(12B):B1, 2007.

[102] JW Connor and HR Wilson. A review of theories of the lh transition. *Plasma Physics and Controlled Fusion*, 42(1):R1, 2000.

[103] RJ Groebner, KH Burrell, and RP Seraydarian. Role of edge electric field and poloidal rotation in the l-h transition. *Physical review letters*, 64(25):3015, 1990.

[104] K. C. Shaing and E. C. Crume. Bifurcation theory of poloidal rotation in tokamaks: A model for l-h transition. *Phys. Rev. Lett.*, 63:2369–2372, Nov 1989.

[105] MG Shats, Hua Xia, Horst Punzmann, and Gregory Falkovich. Suppression of turbulence by self-generated and imposed mean flows. *Physical review letters*, 99(16):164502, 2007.

[106] Guilhem Dif-Pradalier, Philippe Ghendrih, Yanick Sarazin, Elisabetta Caschera, Frédéric Clairet, Yann Camenen, Peter Donnel, Xavier Garbet, Virginie Grandgirard, Yann Munschy, et al. Transport barrier onset and edge turbulence shortfall in fusion plasmas. *Communications Physics*, 5(1):1–12, 2022.

[107] Julian CR Hunt and David J Carruthers. Rapid distortion theory and the 'problems' of turbulence. *Journal of Fluid Mechanics*, 212:497–532, 1990.

[108] JCR Hunt and PA Durbin. Perturbed vortical layers and shear sheltering. *Fluid dynamics research*, 24(6):375, 1999.

[109] P. W. Terry. Suppression of turbulence and transport by sheared flow. *Rev. Mod. Phys.*, 72:109–165, Jan 2000.

[110] H. Biglari, P. H. Diamond, and P. W. Terry. Influence of sheared poloidal rotation on edge turbulence. *Physics of Fluids B: Plasma Physics*, 2(1):1–4, 1990.

[111] P. H. Diamond, S. I. Itoh, K. Itoh, and T. S. Hahm. TOPICAL REVIEW: Zonal flows in plasma—a review. *Plasma Physics and Controlled Fusion*, 47(5):R35–R161, May 2005.

[112] Ö D Gürcan and PH Diamond. Zonal flows and pattern formation. *Journal of Physics A: Mathematical and Theoretical*, 48(29):293001, 2015.

[113] James C McWilliams. The emergence of isolated coherent vortices in turbulent flow. *Journal of Fluid Mechanics*, 146:21–43, 1984.

[114] David Fyfe and David Montgomery. Possible inverse cascade behavior for drift-wave turbulence. *The Physics of Fluids*, 22(2):246–248, 1979.

[115] MG Shats, Hua Xia, and Horst Punzmann. Spectral condensation of turbulence in plasmas and fluids and its role in low-to-high phase transitions in toroidal plasma. *Physical Review E*, 71(4):046409, 2005.

[116] Bo Qu, Aurore Naso, and Wouter JT Bos. Cascades of energy and helicity in axisymmetric turbulence. *Phys. Rev. Fluids*, 3(1):014607, 2018.

[117] Benjamin Favier, Fabien S Godeferd, Claude Cambon, and Alexandre Delache. On the two-dimensionalization of quasistatic magnetohydrodynamic turbulence. *Physics of Fluids*, 22(7):075104, 2010.

[118] Basile Gallet. Exact two-dimensionalization of rapidly rotating large-reynolds-number flows. *Journal of Fluid Mechanics*, 783:412–447, 2015.

[119] TJ Boyd, TJM Boyd, and JJ Sanderson. *The physics of plasmas*. Cambridge University Press, 2003.

[120] Patrick H Diamond, Sanae-I Itoh, and Kimitaka Itoh. *Modern Plasma Physics: Volume 1, Physical Kinetics of Turbulent Plasmas*. Cambridge University Press, 2010.

[121] Dieter Biskamp. *Nonlinear magnetohydrodynamics*. Number 1. Cambridge University Press, 1997.

[122] Barbara Bigot and Sébastien Galtier. Two-dimensional state in driven magnetohydrodynamic turbulence. *Physical Review E*, 83(2):026405, 2011.

[123] B. Gallet and C. R. Doering. Exact two-dimensionalization of low-magnetic-reynolds-number flows subject to a strong magnetic field. *Journal of Fluid Mechanics*, 773:154–177, 2015.

[124] Akira Hasegawa and Kunioki Mima. Pseudo-three-dimensional turbulence in magnetized nonuniform plasma. *The Physics of Fluids*, 21(1):87–92, 1978.

[125] JE Rice, A Ince-Cushman, JS Degrassie, L-G Eriksson, Y Sakamoto, A Scarabosio, A Bortolon, KH Burrell, BP Duval, C Fenzi-Bonizec, et al. Inter-machine comparison of intrinsic toroidal rotation in tokamaks. *Nuclear Fusion*, 47(11):1618, 2007.

[126] Paul F Fischer, James W Lottes, and Stefan G Kerkemeier. nek5000 web page, 2008.

[127] Jason W Bates and David C Montgomery. Toroidal visco-resistive magnetohydrodynamic steady states contain vortices. *Physics of Plasmas*, 5(7):2649–2653, 1998.

[128] Jorge A Morales, Wouter JT Bos, Kai Schneider, and David C Montgomery. Intrinsic rotation of toroidally confined magnetohydrodynamics. *Physical review letters*, 109(17):175002, 2012.

[129] H. K. Moffatt. Dynamo action associated with random inertial waves in a rotating conducting fluid. *Journal of Fluid Mechanics*, 44:705–719, 1970.

[130] E. N. Parker. *Cosmical magnetic fields: Their origin and their activity*. 1979.

[131] B. Sreenivasan and C.A. Jones. Helicity generation and subcritical behaviour in rapidly rotating dynamos. *Journal of Fluid Mechanics*, 688:5–30, 2011.

[132] Douglas K Lilly. The structure, energetics and propagation of rotating convective storms. part ii: Helicity and storm stabilization. *Journal of the atmospheric sciences*, 43(2):126–140, 1986.

[133] John Molinari and David Vollaro. Rapid intensification of a sheared tropical storm. *Monthly Weather Review*, 138(10):3869–3885, 2010.

[134] GV Levina and Michael T Montgomery. Numerical diagnosis of tropical cyclogenesis based on a hypothesis of helical self-organization of moist convective atmospheric turbulence. In *Doklady Earth Sciences*, volume 458, pages 1143–1148. Springer, 2014.

[135] Antoine Craya. *Contribution à l'analyse de la turbulence associée à des vitesses moyennes*. PhD thesis, 1957.

[136] JR Herring. Approach of axisymmetric turbulence to isotropy. *The Physics of Fluids*, 17(5):859–872, 1974.

[137] C Cambon and L Jacquin. Spectral approach to non-isotropic turbulence subjected to rotation. *Journal of Fluid Mechanics*, 202:295–317, 1989.

[138] Fabian Waleffe. The nature of triad interactions in homogeneous turbulence. *Physics of Fluids A: Fluid Dynamics*, 4(2):350–363, 1992.

[139] Alexandros Alexakis. Helically decomposed turbulence. *Journal of Fluid Mechanics*, 812:752, 2017.

[140] Robert H Kraichnan. Helical turbulence and absolute equilibrium. *Journal of Fluid Mechanics*, 59(4):745–752, 1973.

[141] JC André and M Lesieur. Influence of helicity on high reynolds number isotropic turbulence. *J. Fluid Mech*, 81:187–207, 1977.

[142] Qiaoning Chen, Shiyi Chen, and Gregory L Eyink. The joint cascade of energy and helicity in three-dimensional turbulence. *Physics of Fluids*, 15(2):361–374, 2003.

[143] A Brissaud, Uriel Frisch, Jacques Léorat, Marcel Lesieur, and Alain Mazure. Helicity cascades in fully developed isotropic turbulence. *Physics of Fluids*, 16(8):1366–1367, 1973.

[144] Pablo Daniel Mininni and A Pouquet. Helicity cascades in rotating turbulence. *Physical Review E*, 79(2):026304, 2009.

[145] Raffaele Marino, Pablo D Mininni, Duane Rosenberg, and Annick Pouquet. Emergence of helicity in rotating stratified turbulence. *Physical Review E*, 87(3):033016, 2013.

[146] Kazuhiro Inagaki, Nobumitsu Yokoi, and Fujihiro Hamba. Mechanism of mean flow generation in rotating turbulence through inhomogeneous helicity. *Physical Review Fluids*, 2(11):114605, 2017.

[147] Nobumitsu Yokoi and Axel Brandenburg. Large-scale flow generation by inhomogeneous helicity. *Physical Review E*, 93(3):033125, 2016.

[148] Agris Gailitis, Olgerts Lielausis, Ernests Platacis, Sergej Dement'ev, Arnis Cifersons, Gunter Gerbeth, Thomas Gundrum, Frank Stefani, Michael Christen, and Gotthard Will. Magnetic field saturation in the riga dynamo experiment. *Physical Review Letters*, 86(14):3024, 2001.

[149] Robert Stieglitz and Ulrich Müller. Experimental demonstration of a homogeneous two-scale dynamo. *Physics of Fluids*, 13(3):561–564, 2001.

[150] Romain Monchaux, Michaël Berhanu, Mickaël Bourgoin, Marc Moulin, Ph Odier, J-F Pinton, Romain Volk, Stéphan Fauve, Nicolas Mordant, François Pétrélis, et al. Generation of a magnetic field by dynamo action in a turbulent flow of liquid sodium. *Physical review letters*, 98(4):044502, 2007.

[151] Annick Pouquet and Pablo Daniel Mininni. The interplay between helicity and rotation in turbulence: implications for scaling laws and small-scale dynamics. *Philosophical Transactions of the Royal Society A: Mathematical, Physical and Engineering Sciences*, 368(1916):1635–1662, 2010.

[152] C Rorai, Duane Rosenberg, Annick Pouquet, and Pablo Daniel Mininni. Helicity dynamics in stratified turbulence in the absence of forcing. *Physical Review E*, 87(6):063007, 2013.

[153] Vadim Borue and Steven A Orszag. Spectra in helical three-dimensional homogeneous isotropic turbulence. *Physical Review E*, 55(6):7005, 1997.

[154] Frank G Jacobitz, Kai Schneider, Wouter JT Bos, and Marie Farge. Influence of initial mean helicity on homogeneous turbulent shear flow. *Physical Review E*, 84(5):056319, 2011.

[155] Vassilios Dallas and Steven M Tobias. Forcing-dependent dynamics and emergence of helicity in rotating turbulence. *Journal of Fluid Mechanics*, 798:682–695, 2016.

[156] Paul H Roberts and Eric M King. On the genesis of the earth's magnetism. *Reports on Progress in Physics*, 76(9):096801, 2013.

[157] N. Schaeffer, D. Jault, H.-C. Nataf, and A. Fournier. Turbulent geodynamo simulations: a leap towards Earth's core. *Geophysical Journal International*, 211(1):1–29, 06 2017.

[158] PA Davidson and A Ranjan. Are planetary dynamos driven by helical waves? *Journal of Plasma Physics*, 84, 2018.

[159] PA Davidson and A Ranjan. Planetary dynamos driven by helical waves–ii. *Geophysical Journal International*, 202(3):1646–1662, 2015.

[160] Antoine Briard and Thomas Gomez. Dynamics of helicity in homogeneous skew-isotropic turbulence. *Journal of Fluid Mechanics*, 821:539–581, 2017.

[161] D. Lohse and F. Toschi. Ultimate state of thermal convection. *Physical review letters*, 90(3):034502, 2003.

[162] Alan Burlot, Benoît-Joseph Gréa, Fabien S Godeferd, Claude Cambon, and Jérôme Griffond. Spectral modelling of high reynolds number unstably stratified homogeneous turbulence. *Journal of Fluid Mechanics*, 765:17, 2015.

[163] Takashi Ishihara, Koji Morishita, Mitsuo Yokokawa, Atsuya Uno, and Yukio Kaneda. Energy spectrum in high-resolution direct numerical simulations of turbulence. *Physical Review Fluids*, 1(8):082403, 2016.

[164] B. Favier, L. J. Silvers, and M. R. E. Proctor. Inverse cascade and symmetry breaking in rapidly rotating boussinesq convection. *Physics of Fluids*, 26(9):096605, 2014.

[165] Sita Sundar, Mahendra K Verma, Alexandros Alexakis, and Anando G Chatterjee. Dynamic anisotropy in mhd turbulence induced by mean magnetic field. *Physics of Plasmas*, 24(2):022304, 2017.

[166] Stanislav Boldyrev and Jean Carlos Perez. Spectrum of weak magnetohydrodynamic turbulence. *Physical review letters*, 103(22):225001, 2009.

[167] Wesley Agoua, Benjamin Favier, Alexandre Delache, Antoine Briard, and Wouter JT Bos. Spontaneous generation and reversal of helicity in anisotropic turbulence. *Physical Review E*, 103(6):L061101, 2021.

[168] David Fyfe and David Montgomery. High-beta turbulence in two-dimensional magnetohydrodynamics. *Journal of Plasma Physics*, 16(2):181–191, 1976.